Sustainable ironmaking through solid-state reduction of iron ores with hydrogen: Influence of H_2 gas pressure on reduction kinetics and microstructure evolution

Von der Fakultät für Georessourcen und Materialtechnik der

Rheinisch-Westfälischen Technischen Hochschule Aachen

zur Erlangung des akademischen Grades einer

Doktorin der Ingenieurwissenschaften

genehmigte Dissertation

vorgelegt von

Özge Özgün, M.Sc.

Berichter: Prof. Dr.-Ing. habil. Dierk Raabe

Dr.-Ing. Yan Ma

Prof. Dr. -Ing. Hauke Springer

Tag der mündlichen Prüfung: 25.04.2025

Hayatta en hakiki mürşit ilimdir.

Mustafa Kemal Atatürk

Acknowledgment

As I am coming to the end of one of the most important chapters of my life, my PhD journey, I am filled with an immense appreciation for people, who have supported, guided, and inspired me throughout this challenging, yet rewarding path.

First and foremost, I am deeply grateful to Prof. Dr. Dierk Raabe for his unwavering support throughout my PhD journey, regardless of the circumstances. Working with you has been an absolute pleasure. Every single discussion I had with you made me more inspired and deeply connected to my work. Your insightful perspectives have been a constant source of learning and growth for me. Beyond your professional excellence, your genuine enthusiasm and kindness have made this journey both rewarding and memorable. You have set a remarkable example of what it means to be a great scientist, and I have constantly aspired to follow in your footsteps.

I extend my gratitude to Dr. -Ing Yan Ma for supervising me during my PhD. Your dedication and passion for science have been truly inspiring. Throughout this journey, I have admired your ability to approach challenges with creativity and determination. Your constructive feedback has sharpened my skills, and your visionary perspectives have expanded my understanding of the field. Thank you for your guidance, and encouragement, and for teaching me how to be an independent scientist.

I would like to express my sincere appreciation to Prof. Dr. Mehmet Acet and Assoc. Dr. Aslı Çakır for their invaluable guidance and support during this journey. Their encouragement, endless support, and mentorship have played an important role in shaping my academic career.

I would also like to express my heartfelt gratitude to all my friends who have been an incredible source of support and joy throughout this journey. Tugce Beyazay, Ezgi Hatipoğlu, Beste Payam, Bilgehan Murat Şesen, Ömer Büyükuslu, Taner Özdal, Tim Schwarz, Sharan Roongta, Francisco José Gallardo Basile, Leonardo Aota, Varatharaja Nallathambi, Aparna Saxena, Martí López Freixes, Mari, Aparna, Saxena, Renelle Dubosq, Kartik Umate, Ubaid Manzoor, Xizhen Dong, Navyanth Kusampudi, Chengguang Wu, Mathias Krämer, Isnaldi Souza, Charu Negi, Shiv Shankar, and many more—thank you for your friendship and encouragement. Qing Tan, special thanks to you for always being your wonderful self. The memories we created together will always hold a special place in my heart, and I miss you dearly. Tim Schwarz, your invaluable support,

humor, and endless Twix bars made my writing journey not only bearable but also fun. Thank you 😊.

A special and heartfelt thanks to my life partner, Berke Can Gulten. Thank you for your incredible patience, understanding, and support during this journey. I know that postponing our honeymoon and many unforgettable moments in the early years of our marriage was not easy. Your love and encouragement have meant the world to me, and now, with this chapter behind us, I am so excited to create those beautiful memories together and be fully present for the life we've always dreamed of sharing. Seni çok seviyorum.

Sevgili aileme,

Kilometrelerce uzakta olsanız bile, varlığınızı, sevginizi, desteğinizi ve en önemlisi bana olan güveninizi her zaman hissettirdiniz. Sizin yanımda olmanız, bu sürecin her aşamasında bana güç verdi. Bu zorlu yolculuğun sonunda benim için en büyük ödül, sizin benimle gurur duymanız olacak. Hiçbir diploma, yüzünüzde oluşacak o gurur dolu ifadeden daha fazla mutluluk veremez bana. Umarım ömrüm boyunca size layık bir evlat olmayı sürdürebilirim. İyi ki varsınız. Hepinizi çok seviyorum.

Abstract

Steel production plays an important role in the world's global transition toward sustainable practices, since it is one of the largest contributor to CO_2 emissions in the manufacturing sector, accounting for 8~10% of global CO_2 emissions. Hydrogen-based direct reduction (HyDR) of iron ores has attracted immense attention as a pioneering solution for sustainable ironmaking owing to its high technology readiness level (TRL: 6-8). HyDR is a multistep solid-gas reaction that involves the reduction of hematite to magnetite, followed by wüstite, and finally metallic iron. Adjusting the reduction parameters, such as temperature, reducing gas composition, hydrogen gas pressure, as well as the pellet's chemical composition and microstructural characteristics (*e.g.,* porosity fraction and pore connectivity), are crucial in determining reduction kinetics and have been the focus of extensive research for decades. While prior studies have investigated the impact of hydrogen gas pressure on the reaction kinetics, the underlying reaction mechanisms governing individual reaction steps and microstructural evolution remain poorly understood. In addition, the chemistry of the final product is of great importance since even a small amount of diffusible hydrogen (*e.g.,* in ppm level) retention in the final product (*e.g.,* high-strength steel) can result in catastrophic failure, known as hydrogen embrittlement. Therefore, the influence of the reduction parameters (*e.g.,* hydrogen pressure) on the reaction mechanisms and quality of the final product needs to be better understood to optimize the process efficiency and downstream processes following HyDR of iron ore.

The question of "How hydrogen gas pressure affects the reduction kinetics and microstructural evolution of hematite pellets" was addressed. We investigated the reduction kinetics of hematite pellets with pure hydrogen at 700 °C at various pressures, *i.e.,* 1, 10, and 100 bar under static gas exposure, and 1.3 and 50 bar under dynamic gas exposure. The microstructure of the reduced pellets was characterized by combining X-ray diffraction and scanning electron microscopy equipped with electron backscatter diffraction. The findings revealed that higher hydrogen gas pressure significantly enhances reduction kinetics. The microstructure of the metallic iron transformed from a dense metallic iron layer formed over the oxide surface at 1 bar to porous metallic iron at 100 bar under static conditions. Simultaneously, the pore morphology transitioned from large, elongated shapes at 1 bar to fine, random shapes at 100 bar under dynamic conditions. In addition, questions of "How does hydrogen gas pressure affect the individual reactions of HyDR

iron ore?" and "Does the solid-gas reaction mechanism change with hydrogen gas pressure?" were explored using *in-situ* synchrotron high-energy X-ray diffraction during HyDR to monitor real-time phase transformations of iron ore under hydrogen gas pressures of 1, 10, 50, and 100 bar.

Last but not least, deploying hydrogen in ironmaking raises critical questions about its impact on material properties: How much hydrogen remains in green steel, and will it cause hydrogen embrittlement? To address this, hydrogen content was quantified in iron produced via hydrogen-HyDR and hydrogen plasma smelting reduction (HPSR) using thermal desorption spectroscopy (TDS) and hot extraction. HyDR iron contained 39.90±9.00 wppm hydrogen, which dropped to 1.46±0.50 wppm after melting in an arc furnace, while HPSR iron contained 0.98±0.50 wppm. Hydrogen trapping sites and energies in direct reduced iron were identified using TDS and microstructure analysis. Comparing hydrogen levels in green steel with conventional processes suggests that hydrogen-based methods do not promote hydrogen embrittlement.

The results of this dissertation demonstrate that using hydrogen as a reducing agent to reduce iron ore does not lead to hydrogen embrittlement in the final product. Furthermore, these findings offer valuable insights into the critical influence of hydrogen pressure on the reduction kinetics and microstructural evolution of iron ore during the HyDR process. An increasing H_2 pressure increases the partial pressure of H_2, which promotes faster reduction kinetics. This fact should be considered for the design of industrial reactors. These insights shed light on advancements in furnace design, e.g., hydrogen gas pressure, and process optimization.

Zusammenfassung

Die Stahlproduktion ist verantwortlich für eine weltweiten CO_2-Emissionen von 8-10%. Die wasserstoffbasierte Direktreduktion (HyDR) von Eisenerzen erregt eine große Aufmerksamkeit als alternative Lösung für eine nachhaltige Eisenproduktion. HyDR ist eine mehrstufige Feststoff-Gas-Reaktion, bei der Eisenerz in Form von Hämatit (Fe_2O_3) in Magnetit (Fe_3O_4) umgewandelt und schließlich über Wüstit (FeO) zu metallischem Eisen (Fe) reduziert wird. Dabei spielen die Reduktionsparameter wie Temperatur, Zusammensetzung des Reduktionsgases, Wasserstoffgasdruck, chemische Zusammensetzung der Pellets und die mikrostrukturellen Eigenschaften eine entscheidende Rolle für die Bestimmung der Reduktionskinetik und stehen seit Jahrzehnten im Mittelpunkt umfangreicher Forschungsarbeiten. Die zugrunde liegenden Reaktionsmechanismen, die die einzelnen Reaktionsschritte und die Entwicklung der Mikrostruktur steuern, sind jedoch noch unzureichend verstanden. Einer der entscheidenden Faktoren ist die Zusammensetzung des Endproduktes, da bereits geringe Verunreinigungen durch z.B. Wasserstoff im ppm-Bereich zu katastrophalem Versagen von hochfesten Stählen führen können, bekannt als Wasserstoffversprödung. Daher ist es notwendig den Einfluss der verschiedenen Reduktionsparameter wie *z. B.* Wasserstoffgasdruck, Temperatur etc. auf die Reaktionsmechanismen und schlussendlich auf die Qualität des Endprodukts besser zu verstehen, um die Effizienz des HyDR Prozesses und nachfolgenden Prozessen nach der Direktreduktion besser optimieren zu können.

In dieser Dissertation wurde zunächst untersucht, wie sich der Wasserstoffgasdruck auf die Reduktionskinetik und die damit verbundene mikrostrukturelle Entwicklung von Hämatitpellets auswirkt. Dazu wurde die Reduktionskinetik von Hämatitpellets mit reinem Wasserstoff bei 700 °C bei 1, 10 und 100 bar unter statischen Bedingungen und 1, 3 und 50 bar unter dynamischen Bedingungen untersucht. Die Mikrostruktur der reduzierten Pellets wurde durch eine Kombination von Röntgendiffraktometrie, Rasterelektronenmikroskopie und Elektronenrückstreubeugung charakterisiert. Die Ergebnisse zeigen, dass ein höherer Wasserstoffgasdruck die Reduktionskinetik unter beiden Bedingungen signifikant beschleunigt. Die Mikrostruktur änderte sich von einer dichten metallischen Eisenschicht, die sich bei 1 bar über der Oxidoberfläche bildete, zu einem porösen metallischen Eisen bei 100 bar. Gleichzeitig änderte sich die

Porenmorphologie von großen, länglichen Porenform zu feinen, zufälligen Porenform von 1 zu 100 bar. Zusätzlich, wie sich der Wasserstoffgasdruck auf die verschiedenen Reaktionen der Eisenerzumwandlung durch HyDR auswirkt und ob sich die Fest-Gas-Reaktionsmechanismen bei höherem Wasserstoffgasdruck verändern. Dazu wurden *in-situ* HyDR-Experimente mit Hochenergie-Röntgendiffraktometrie durchgeführt, um die Phasenumwandlungen des Eisenerzes bei verschiedenen Wasserstoffgasdrücken von 1, 10, 50 und 100 bar in Echtzeit zu untersuchen.

Nicht zuletzt wirft der Einsatz von Wasserstoff in der Eisenherstellung kritische Fragen hinsichtlich seiner Auswirkungen auf die Materialeigenschaften auf: Wie viel Wasserstoff verbleibt in grünem Stahl und führt dies zu Wasserstoffversprödung? Um dies zu untersuchen, wurde der Wasserstoffgehalt in Eisen, das durch HyDR und Wasserstoffplasma-Schmelzreduktion hergestellt wurde, mittels thermischer Desorptionsspektroskopie und Heißextraktion quantifiziert. HyDR-Eisen enthielt 39,90 ± 9,00 wppm Wasserstoff, der nach dem Schmelzen im Elektrolichtbogenofen auf 1,46 ± 0,50 wppm sank, während HPSR-Eisen 0,98 ± 0,50 wppm enthielt. Der Vergleich des Wasserstoffgehalts in grünem Stahl mit konventionellen Methoden deutet darauf hin, dass H_2-basierte Methoden die Wasserstoffversprödung nicht fördern und somit eine nachhaltige Lösung für die großtechnische Stahlproduktion weltweit darstellen.

Die Ergebnisse dieser Dissertation zeigen, dass die Verwendung von Wasserstoff als Reduktionsmittel zur Reduktion von Eisenerz nicht zu Wasserstoffversprödung im Endprodukt führt. Darüber hinaus liefern diese Ergebnisse wertvolle Einblicke über den entscheidenden Einfluss des Wasserstoffdrucks auf die Reduktionskinetik und die mikrostrukturelle Entwicklung des Eisenerzes während des HyDR-Prozesses. Ein steigender Wasserstoffdruck erhöht den Partialdruck von Wasserstoff, was schnellere Reduktionskinetik fördert. Diese Tatsache sollte bei der Gestaltung von industriellen Reaktoren berücksichtigt werden. Diese Erkenntnisse ermöglichen es in Zukunft den Prozess zu optimieren z.B. hinsichtlich der Ofenkonstruktion, des Wasserstoffgasdrucks, und der Prozessparameter.

Preface

This Dr.-Ing. thesis adopts a cumulative format, comprising manuscripts from the following publications. These works are either already published, or prepared for submission. The manuscripts included are:

Paper I

Green Ironmaking at Higher H_2 Pressure: Reduction Kinetics and Microstructure Formation During Hydrogen-Based Direct Reduction of Hematite Pellets.

Özge Özgün, Imants Dirba, Oliver Gutfleisch, Yan Ma, Dierk Raabe

Journal of Sustainable Metallurgy, 2024, 10(3), 1127-1140

My contributions to this work included analyzing the reduction experiments, conducting microstructural investigations, interpreting the data, and drafting the original manuscript.

Paper II

Green ironmaking under high H_2 pressure: Resolving individual reaction steps via in-situ synchrotron high-energy X-ray diffraction

Özge Özgün, Gökhan Gizer, Claudio Pistidda, Laurine Choisez, Dierk Raabe and Yan Ma

Prepared for submission

My contributions to this work comprised planning and performing in-situ reduction experiments, data analysis, microstructural investigations, data interpretation, and drafting the original manuscript.

Paper III

How much hydrogen is in green steel?

Özge Özgün, Xu Lu, Yan Ma, Dierk Raabe

NPJ Materials Degradation, 2023, 7(1), 78

My contributions to this work comprised analyzing the reduction experiments, TDS data analysis, microstructural investigations, data interpretation, and drafting the original manuscript.

List of Abbreviations

BF	Blast Furnace
BOF	Basic Oxygen Furnace
BSE	Backscatter electron
DRI	Direct Reduced Iron
EAF	Electric Arc Furnace
EBSD	Electron Backscatter Diffraction
GF	Gas Film Model
GSAS	Generalized Structure Analysis System
HEXRD	High-energy X-Ray Diffraction
HyDR	Hydrogen-based Direct Reduction
HPSR	Hydrogen-based Plasma Smelting Reduction
HPTGA	High-pressure Thermogravimetric Analysis
MAUD	Material Analysis Using Diffraction
Nano-CT	X-Ray Nano-computed Tomography
NG	Nucleation and Growth model
OPS	Colloidal Particle Suspension
PB	Phase Boundary model
SE	Secondary Electron
SEM	Scanning Electron Microscopy
SD	Solid Diffusion model
TDS	Thermal Desorption Spectroscopy
TGA	Thermogravimetric Analysis
TRL	Technology Readiness Level
XRD	X-Ray Diffraction

List of Symbols

ΔG	Gibbs free energy change
ΔG^0	Standard Gibbs free energy of the reaction
ΔH	Enthalpy change
ΔS	Entropy change
T	Absolute temperature
T_0	Reaction onset temperature
T_p	Hydrogen desorption peak temperature
Q	Reaction quotient
P_{H_2}	Partial pressure of H_2
P_{H_2O}	Partial pressure of H_2O
k	Rate constant
E_a	Activation energy
R	Gas constant
M_0	Initial mass of hematite pellet
M_t	Instantaneous mass of hematite pellet
M_f	Final mass of hematite pellet
λ	X-Ray wavelength
ϕ^f	Apparent chemical reaction constant for the forward reaction
Φ^2	Thiele modulus
R_O	Rate of oxygen removal
A	Pre-exponential factor
t	Time
$X_{i\rightarrow j}$	Conversion degree of phase i to phase j
w_i	Weight fraction of phase i
V_o	Interface velocity
ρ_O	Density of metal
ρ_m	Density of metal

β *and* Φ	Heating rate
n_{Fe}^{i}	Mol of iron in phase i
D_{eff}	Effective diffusivity of H_2
ε	Sample porosity, dimensionless
D_{H_2}	Effective intraparticle diffusivity of H_2
$D_{H_2}^{m}$	Molecular diffusivity of H_2
$D_{H_2}^{k}$	Knudsen diffusivity of H_2
M_{H_2,H_2O}	Molecular mass of H_2 and H_2O
σ_{H_2}	Diffusion volume of H_2, 7.07 cm^3/mol
σ_{H_2O}	Diffusion volume of H_2O, 12.7 cm^3/mol
D_{H_2,H_2O}	Mass diffusivity of H_2 through H_2O
y_{H_2}	Mole fraction of H_2
y_{H_2O}	Mole fraction of H_2O
b_m	the length of the interface
h_m	the thickness of the metal layer

Table of Contents

Thesis Outline

This thesis is composed of seven chapters, structured as follows:

Chapter 1 introduces the decarbonization challenge in the steel industry and explains the urgent need for sustainable steel production methods. It highlights the significant CO_2 emissions associated with traditional blast furnace-basic oxygen furnace steelmaking routes. The chapter delves into hydrogen-based direct reduction (HyDR) as a promising pathway for green steel production. The process of HyDR is briefly explained, including its integration into the iron and steel industry and its potential to eliminate CO_2 emissions. The chapter also highlights critical knowledge gaps, including the impact of hydrogen gas pressure on reduction behavior and microstructural evolution of hematite pellet during HyDR, as well as the risk of hydrogen embrittlement in green steel arising from the use of hydrogen as a reducing agent. These challenges are outlined as critical points for further research to implementation of hydrogen-based ironmaking on an industrial scale.

Chapter 2 provides an overview of the conventional and hydrogen-based steelmaking processes. It delves into the conventional steel production processes, explaining the source of CO_2 emission from iron and steel industry. It provides an explanation of the working principle of blast furnace , basic oxygen furnace, and electric arc furnace, as well as direct reduction technologies such as MIDREX and HYL/Energiron. The chapter then transitions into the HyDR process, providing in-depth information about thermodynamics, reduction kinetics, and microstructural evolution during the reduction of hematite pellets.

Chapter 3 is based on publication "Özgün, Ö., Dirba, I., Gutfleisch, O., Ma, Y., & Raabe, D. (2024). Green ironmaking at Higher H2 pressure: reduction kinetics and microstructure formation during hydrogen-based direct reduction of hematite pellets. *Journal of Sustainable Metallurgy*, *10*(3), 1127-1140." Here, the influence of H_2 gas pressure on the overall reduction kinetics and microstructural evolution or hematite pellets were investigated using thermogravimetric analysis, X-ray diffraction, and scanning electron microscopy equipped with electron backscattering diffraction.

Fundamental questions explored are: How does H_2 gas pressure influence the reduction kinetics of hematite pellets at 700 °C? What is the reaction behavior of hematite pellets under highly reactive conditions, such as 100 bar H_2 gas pressure? How does H_2 gas pressure impact the microstructural evolution of iron during reduction?

Chapter 4 is based on the submitted work: "Özge Özgün, Gökhan Gizer, David Melching, Kartik Umate, Eric Woods, Laurine Choisez, Guillermo Requena, Claudio Pistidda, Dierk Raabe, Yan Ma (2025). Green ironmaking under high H_2 pressure: resolving individual reaction steps via in-situ synchrotron high-energy diffraction. *Submitted to Acta Materialia.". Here a*n *in-situ* synchrotron high-energy X-ray diffraction study is conducted to examine the impact of H_2 gas pressure on the individual reaction steps of hematite reduction. Additionally, Nano-computed X-ray tomography is utilized to analyze the effect of hydrogen gas pressure on the 3D pore morphology of direct reduced iron.

Fundamental questions explored are: How does hydrogen gas pressure influence the kinetics of individual reduction steps in hematite pellets at 700 °C? What is the impact of hydrogen gas pressure on the rate-limiting step in hydrogen-based direct reduction? How does hydrogen gas pressure affect the 3D pore evolution of the final product?

Chapter 5 is based on publication "Özgün, Ö., Lu, X., Ma, Y., & Raabe, D. (2023). How much hydrogen is in green steel?. *npj Materials Degradation*, *7*(1), 78." Here, the hydrogen content in direct reduced iron, melted direct reduced iron, and hydrogen-plasma-reduced iron is analyzed using thermal desorption spectroscopy.

Fundamental questions explored are: How much hydrogen is retained in green iron? Will green steel face significant risks of hydrogen embrittlement? Where is hydrogen trapped within direct reduced iron? What methods can effectively remove hydrogen trapped in direct reduced iron?

Chapter 6 provides a summary of the thesis and discusses the key results.

Chapter 7 provides an outlook on hydrogen-based direct reduction and explores potential future approaches, with a particular focus on the effects of impurities and defective structure of wüstite phase. Preliminary results on Al_2O_3 impacts in hydrogen-based direct reduction are reported, highlighting their influence on solid-gas reaction kinetics and microstructural evolution. The chapter underscores the importance of understanding the chemical composition of the starting pellet to optimize processing before reduction. In the future, my efforts will aim to integrate these findings with atomic-scale characterization techniques for a more comprehensive understanding of the impurity effects during hydrogen-based direct reduction of iron ore.

Chapter 8 provides supplementary information to chapter 4 and chapter 5

1. INTRODUCTION

1.1. Decarbonization challenge in the steel industry and a new pathway to green steel

Steel is by far the most important structural metallic material in terms of its production quantity and versatile applications in numerous sectors, such as construction, civil and industrial infrastructures, transportation, etc. [1] . Since 2010, annually more than 1500 million tons of crude steel is produced [2] **Fig. 1**a. Steel is either produced through the primary steel synthesis, *i.e.,* blast furnace-basic oxygen furnace (BF-BOF) route, or secondary steel synthesis, *i.e.,* recycling of steel scrap in an electric arc furnace (EAF). Currently, primary steel synthesis supplies 2/3rd of global steel production [1], and only 1/3rd of global steel production is met by secondary synthesis [3].

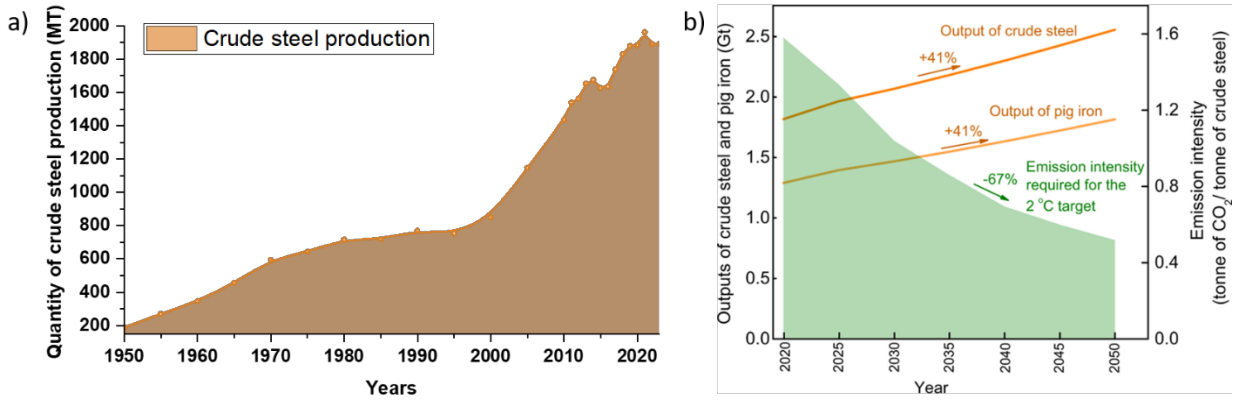

Fig. 1. a) The global crude steel production quantity from 1950 to 2023. The data is obtained from the World Steel Association [2]. b) Projected increase in steel production and CO_2 emissions from steelmaking until 2050. The green-shaded area represents the required reduction in CO_2 emissions to meet the 2°C climate target set under the Paris Agreement, which aims to limit global temperature rise to below 2°C above pre-industrial levels. Reproduced from ref. [4].

The BF route deploys fossil resources (coal and coke) in the reduction of iron ores and thus emits on average ~2.3 tons of CO_2 per ton of steel [5]. Compared with the BF route, EAF steelmaking is more eco-friendly with less energy consumption and CO_2 emissions, *i.e.*, 0.3-0.6 tons of CO_2 emissions per ton of recycled steel [6]. Overall, the steelmaking process contributes significantly to global CO_2 emissions (>2800 MT CO_2 per year [4]), accounting for approximately 10% when indirect emissions from electricity use are included [7]. Due to the increasing demand for steel in developing countries and the global reliance on primary steelmaking is expected to grow in the following decades, **Fig. 1**b. The Paris Agreement is a global accord adopted in 2015 to combat climate change by limiting global temperature rise to below 2°C above pre-industrial levels, with

limiting it at 1.5°C [8]. To align with this target, alternative methods for primary steelmaking with net-zero emissions must be quickly developed and implemented to reduce the massive CO_2 emissions in the steel industry.

Several strategies have been proposed to achieve reduced or zero CO_2 emissions in steelmaking, including increased scrap recycling, the adoption of electrolysis of iron ore [9], carbon capture and storage (CCS) [4, 10], and using hydrogen as a reductant instead of carbon. However, many of these strategies face limitations due to the absence of appropriate materials, economic constraints, or insufficient capacity to meet global steel demand with the available input materials. For instance, the electrolysis of the iron ore faces limitations due to the absence of suitable anode and cathode materials capable of withstanding the extreme conditions of the process, including high temperatures (~1600 °C) and substantial electrical energy requirements (~3700 kWh/t_{Fe}) [11]. Another strategy for reducing CO_2 emissions is carbon capture and storage (CCS), with its market entry dependent on political decisions due to its high cost, energy intensity, and technical complexity, making the process adoption financially and logistically challenging [4]. Regarding steel recycling, the current steel demand cannot be met with recycling when annual steel demand growth and longevity of steel products (*e.g.,* over 50 years in construction and more than 25 years in machinery [12, 13], in average ~35 years [12]) are considered. Among these strategies, the hydrogen-based reduction (HyDR) of iron ore is the most promising and clean production method for steelmaking given that hydrogen is produced from renewable sources [3]. Water electrolysis is the most promising candidate to produce sufficient H_2 for green steelmaking processes (70,000 $km^3_{STP}/h\ Mt_{steel}/year$)[14].

Hydrogen offers a sustainable alternative to carbon-based reductants in steelmaking, given that hydrogen is produced via renewable energy. Unlike traditional methods, the reaction between H_2 and iron oxide produces only water as a by-product, making it significantly more environmentally friendly. Hydrogen-based reduction process can be performed in both its solid and liquid states, known as hydrogen-based direct reduction (HyDR) and hydrogen-based plasma smelting reduction (HPSR), respectively [6, 15]. HPSR is defined as the removal of chemically-bounded hydrogen from the liquid iron oxide with hydrogen in its atomic and plasma states. HyDR, on the other hand, occurs in the solid state and involves the removal of oxygen from the iron oxide lattice through a chemical reaction with H_2.

With a high technology readiness level (TRL 6–8) [3], HyDR is well-suited for industrial implementation and it paves an alternative way for cleaner and more sustainable steel production.

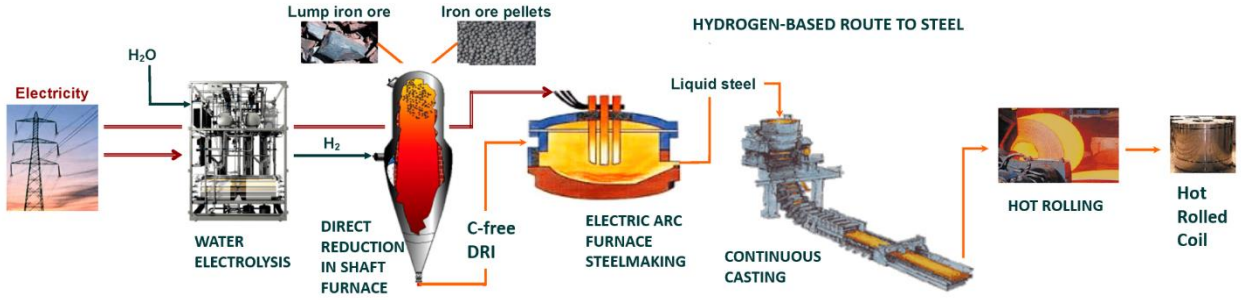

Fig. 2. Hydrogen-based Steelmaking Route: Green hydrogen (H_2) is produced via water electrolysis using renewable electricity. Produced H_2 is used as a reductant in a shaft furnace to reduce lump iron ore or iron ore pellets into direct reduced iron (DRI). The DRI is then fed into an electric arc furnace, where it is melted and refined into liquid steel. The liquid steel undergoes continuous casting to form slabs, which are subsequently processed through the hot-rolling stage to produce a hot-rolled coil. Adapted from ref [16].

Fig. 2. illustrates a sustainable, HyDR steelmaking process designed to reduce CO_2 emissions. This approach integrates green hydrogen production, direct reduction of iron ore, and electric arc furnace (EAF) steelmaking, offering a carbon-free alternative to traditional steelmaking methods. Renewable electricity is utilized in the water electrolysis process to split water into hydrogen and oxygen. Hydrogen produced without CO_2 emission is referred to as "green hydrogen" and it is a critical component of sustainable hydrogen-based steelmaking route. In this process, green hydrogen is used as a reducing agent in a shaft furnace, where it reacts with solid feedstock (*e.g.,* lump iron ore or iron ore pellets) at high temperatures. During this process, hydrogen removes oxygen from the iron oxide in the ore at the temperature range 600-1100 °C, producing direct reduced iron (DRI), a.k.a. sponge iron due to its highly porous nature, in a carbon-free form. Unlike traditional methods that rely on carbon-based reducing agents (i.e., coal and coke), this process eliminates CO_2 emissions by producing water vapor H_2O as a by-product. After reduction, DRI is charged into an EAF (powered by renewable electricity), where it is melted and refined into liquid steel. The liquid steel is processed in a continuous casting system, where it is solidified into slabs. The cast slabs or billets are then sent to the hot-rolling mill, which is rolled at high temperatures to produce hot-rolled coils**.**

1.2. Motivation

Direct reduction is a well-established technology that converts iron ore iron ore pellets (10-16 mm in diameter) into DRI in the solid-state, using steam-reformed natural gas (H_2 and CO from CH_4) or gasified coal as reducing agents. Commercial reduction technologies typically operate at elevated pressures; for instance, the MIDREX process (utilizing 55–80% H_2 in the reducing gas) operates at 2 bar, while the HyL/Energiron process operates at 6–8 bar total pressure. Therefore, understanding the effect of total hydrogen gas pressure on the reduction behavior of iron ore during HyDR is crucial.

However, while previous studies have explored the influence of hydrogen gas pressure on reduction kinetics, systematic investigations into its effect on HyDR remain limited in the literature. For instance, the effect of hydrogen gas pressure on the rate-limiting reaction and driving mechanisms of the rate limiting reaction need to be better understood and effectively integrated into furnace design for the HyDR of iron ore. Furthermore, effect of hydrogen gas pressures on the microstructural evolution of iron ore has not been systematically studied. Particularly, the effect of product morphology on the reaction behavior at the microscopic scale has remained unclear so far. These facts make it challenging to conduct pellet, gas, and process optimization for higher efficiency and faster metallization. These gaps should be addressed by investigating the fundamental solid-state reaction mechanism of HyDR associated with hydrogen gas pressure and the microstructural evolution of iron ore at different hydrogen gas pressures. The aim is to transition the process design from an empirical approach to a knowledge-based approach, providing deeper insight into the higher efficiency of solid-state hydrogen-based ironmaking process.

Additionally, as hydrogen is deployed in metallurgical practices, understanding its consequences becomes critical, particularly due to the potential retention of mono-atomic hydrogen in the final product. Hydrogen atoms, inherited from the reduction process, may became trapped in steel products. Even a small amount of diffusible and weakly trapped hydrogen, particularly in high-strength steel, degrades its mechanical performance and even leads to premature failure. Such detrimental effect induced by hydrogen is known as hydrogen embrittlement. Therefore, hydrogen-based iron making poses critical questions: How much hydrogen is in green steel? Will it pose severe hydrogen embrittlement risk? Addressing these concerns is crucial before scaling hydrogen-

based iron making to industrial levels and introducing green steel into the market. The potential of hydrogen embrittlement in green steel has to be discussed based on the comparison of the hydrogen contents in iron and steel produced by conventional and hydrogen-based iron making approaches. This knowledge is essential for designing a process route that accounts for the effective removal of hydrogen in downstream operations.

2. STATE OF THE ART

2.1. Overview of Iron and Steel Production

The blast furnace (BF), **Fig. 3**., is a high-temperature reactor used since the 15th century for iron production. In the BF, iron ore (Fe_2O_3 or Fe_3O_4), coke (carbon), and limestone ($CaCO_3$) are loaded through a bell system. The furnace is operated based on a counter-current redox principle, where descending iron ore reacts with ascending hot gases, primarily carbon monoxide (CO). The solid-gas reaction takes place between CO and iron ore, leading to the formation of metallic iron with a residual fraction of wüstite. Subsequently, a complete reduction of the pellet and its melting occurs in the lower part of the BF. The molten metal is called pig iron, which contains 3 to 5 wt.% of carbon depending on the S, P, and Si content in the hot metal [17].

The reactions in the BF start with the combustion of coke with hot air burden (preheated to 800-1200 °C) (1.1), containing ~23 wt% of O_2 and 77 wt% of N_2.

$$C_{(s)}+O_{2(g)}\rightarrow CO_{2(g)},\ \Delta H^0=-394.13\ \text{kJ/mol of C} \quad (1.1)$$

The highly exothermic nature of this reaction led to the release of a large amount of heat, ~1650 °C. At this temperature, CO_2 is thermodynamically unstable, thus reacting with C to produce CO, a reducing agent. This reaction is known as *Boudouard reaction* or *gasification reaction* (1.2) [18].

$$C_{(s)}+CO_{2(g)}\rightarrow 2CO_{(g)},\ \Delta H^0=170.7\ \text{kJ/mol of C} \quad (1.2)$$

The reaction of iron ore with CO gas starts at temperatures between 500 and 600 °C. The reaction order above 570 °C is summarized below.

$$3Fe_2O_{3(s)}+CO_{(g)}\rightarrow 2Fe_3O_{4(s)}+CO_{2(g)},\ \Delta H^0_{298}=-52.43\ \text{kJ/mol of CO} \quad (1.3)$$

$$xFe_3O_{4(s)}+xCO_{(g)}\rightarrow 3Fe_xO_{(s)}+CO_{2(g)},\ \Delta H^0_{298}=40.46\ \text{kJ/mol of CO} \quad (1.4)$$

$$3Fe_xO_{(s)}+CO_{(g)}\rightarrow xFe_{(s)}+CO_{2(g)},\ \Delta H^0_{298}=-18.54\ \text{kJ/mol of CO} \quad (1.5)$$

Above 570 °C, Fe_xO is thermodynamically unstable, hence the reaction proceeds from Fe_3O_4 to Fe directly, (1.6).

$$Fe_3O_{4(s)}+4CO_{(g)}\rightarrow 3Fe_{(s)}+4CO_{2(g)},\ \Delta H^0_{298}=-3.79\ \text{kJ/mol of CO} \quad (1.6)$$

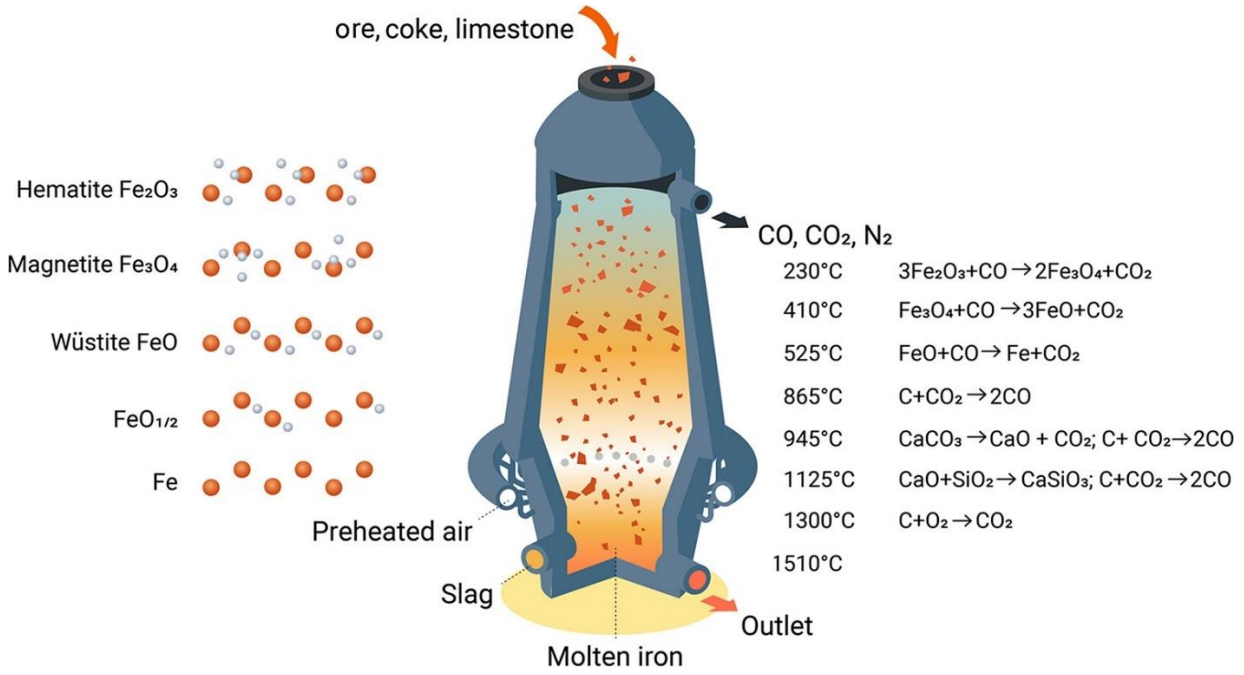

Fig. 3. Illustration of a blast furnace presenting the chemical reactions and their temperature zones during the production of molten (pig) iron. Adopted from Ref [1].

The basic oxygen furnace (BOF) is the second step in conventional steelmaking, which converts pig iron into steel. In this process, pig iron is refined into steel by removing impurities (*e.g.,* C, Si, Mn, P, and S) through the injection of oxygen into the molten pig iron. Oxygen is blown into the molten metal at high speed (*i.e.,* 330 m/s in dry air), creating a turbulent recirculation zone. This turbulence allows oxygen to penetrate the molten metal and form a calci-ferrite slag (CaO-SiO_2-MnO-FeO). High speed of oxygen creates turbulence zone. The formation of the turbulence zone leads to the development of a slag-metal emulsion. The majority of the reaction between carbon and oxygen occurs within this slag-metal emulsion. Oxygen reacts with carbon in the molten metal suspended within the emulsion. As the carbon content in the metal droplets decreases, the density of the droplets increases. When the density of the droplets becomes higher than that of the metal-slag emulsion, the droplets return to the metal bath. The carbon content in the molten iron can be reduced as low as 0.04% in BOF.

The electric arc furnace (EAF) steelmaking process is a highly efficient method for recycling scrap metal into steel. In this process, an electric arc is generated between graphite electrodes and metal scrap, creating the heat necessary to melt the charged materials. The electrical current passes through the charging materials and rapidly melts them. The charging materials of EAF can be

categorized into three classes; metallic materials, slag-forming materials, and oxidizing and carburizing materials.

- The metallic materials used in the electric arc furnace process include steel scrap, direct reduced iron (DRI), pig iron, and ferroalloys. Steel scrap is categorized based on the type and quantity of alloying elements it contains. Direct reduced iron serves as a high-purity iron-rich input, while pig iron is added to tune the carbon content of the steel melt. Ferroalloys play a dual role, acting as deoxidizers and providing essential alloying elements to achieve the desired chemical composition and steel properties.
- The slag-forming materials are used to form slag in the EAF. Metallurgical lime (a CaO carrier) is the basic slag-forming material in the EAF process, where it serves as a flux to remove impurities (i.e., Si, P, and S). The metallurgical lime is typically added in quantities ranging from 1 to 3 wt.% of charge in EAF. In addition, dolomitic lime (*i.e.,* a type of lime containing calcium carbonate and magnesium carbonate with a trace amount of silica and alumina) is added to increase MgO content to protect the refractory lining of EAF walls by increasing the basicity of the slag.
- The oxidizing material in EAF is supplied by injecting the oxygen gas into the metal bath to produce slag. For carburization, pig iron, coal, coke, and scrap graphite electrodes are used as charging material in EAF. Carbon has various functions in EAF such as acting as an alloying element, a source of thermal energy generated from its oxidation reaction, and a slag foaming agent.

EAF works based on the arc melting principle. After charging, graphite electrodes are lowered until they contact the charging materials, creating an electric arc that generates intense heat to melt the charging materials. The melting period of charge changes from 30 to 100 minutes depending on the power of the supply transformer. During this process, oxidation of the metal bath and slag formation occur simultaneously. The slag is formed as a result of the oxidation reaction of charging materials with oxygen injected through the lances and the dissolution of slag-forming materials. Reactions occur at the surface of the slag and the interface between the liquid metal bath and the slag. The primary oxides that are commonly found in EAF steelmaking slag CaO, SiO_2, MgO, MnO, FeO, Fe_2O_3, Al_2O_3, Cr_2O_3, and P_2O_5. At the end of melting, the chemical composition of slag typically consists of the following proportions: CaO (25-35 wt.%), SiO_2 (20-30 wt.%), FeO

(25-40 wt.%) and MgO (5-10 wt.%). Minor components, including MnO, Fe_2O_3, Al_2O_3, and P_2O_5 are present at concentrations less than 2 wt.%.

Once the melting, refining, and alloying processes are complete, and the desired temperature and chemical composition are achieved, the steel is poured into a preheated ladle by tilting the furnace.

Direct reduction of iron ore is another a mature technology and ~135 million tons of steel were produced in 2023 via steam-reformed natural-gas-based and gasified-coal-based direct reduction [19]. During direct reduction, iron ores are converted into metallic iron, commonly referred to as direct reduced iron (DRI) or sponge iron, through a solid-state process that does not involve melting. This reduction occurs using hydrogen (H_2) and carbon monoxide (CO) gas mixtures, following the overall reaction: $Fe_2O_3 + 3H_2\,(CO) \rightarrow 2Fe + 3H_2O\,(CO_2)$. The primary industrial technologies for direct reduction include MIDREX, HYL/Energiron, and Rotary Kilns. In 2023, the MIDREX process led the market, producing ~56% of global direct reduced iron (DRI), followed by Rotary Kilns (~30%) and the HYL/Energiron process (~12%) [20].

In the MIDREX process, **Fig. 4.**, natural gas (CH_4) undergoes a gas reforming process, where it reacts with water steam (H_2O) and carbon dioxide (CO_2) to produce hydrogen (H_2) and carbon monoxide (CO) as reducing gases. The key reactions are:

$$CH_4 + H_2O \rightarrow 3H_2 + CO \quad (1.7)$$

$$CH_4 + CO_2 \rightarrow 2H_2 + CO \quad (1.8)$$

H_2O and CO_2 required for these reactions are collected from the off-gas of the shaft furnace. The reformed gas, containing 55–80% hydrogen [21], is then injected into a shaft furnace to reduce iron ore (10-16 mm in diameter) at temperatures of 800–900°C [22].

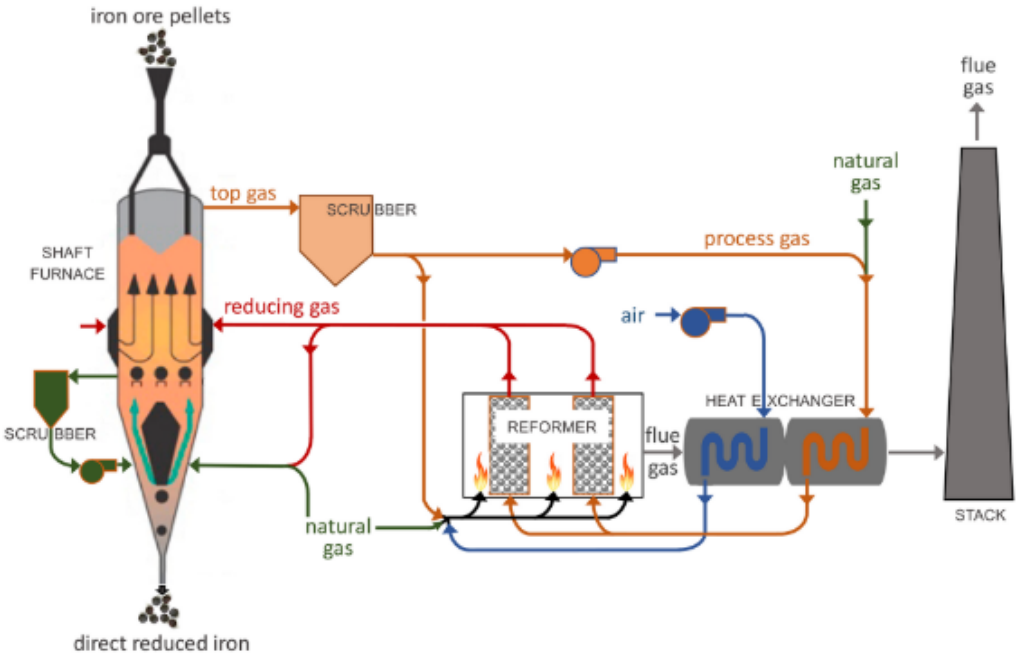

Fig. 4. Schematic illustration of MIDREX direct reduction process for iron ore pellets using natural gas in a shaft furnace. The reformer generates reducing gases (H_2 and CO) from natural gas (CH_4), which are injected into the shaft furnace to reduce iron oxide. The top gas is cleaned in a scrubber and reformed for reuse in the reduction process, while the flue gas is discharged through the stack. Adopted from ref [14].

In contrast, the HYL/Energiron process bypasses the separate gas reformer process. Instead, the reducing gases are generated directly in the shaft furnace through the in-situ reformation of CH_4. In this process, the surface of iron oxide and iron act as a catalyst, facilitating the dissociation of CH_4, and the production of reducing gas[23]. The dissociation of CH_4 is facilitated by high pressure, 6-8 bar [24-27]. The use of elevated pressure conditions facilitates the dissociation of methane over the iron ore pellets in the shaft furnace.

2.2. Hydrogen-based Direct Reduction

HyDR is a solid-gas reaction involving the interaction of oxygen atoms within the iron oxide lattice with monoatomic hydrogen. The HyDR of iron ore is governed by the thermodynamics and kinetics of solid-gas reactions. Thermodynamics and kinetics are two distinct fundamental frameworks that help us understand solid-gas reactions. Thermodynamics tells us whether a reaction is feasible or not under given conditions, *e.g.,* temperature, gas atmosphere, and composition and pressure of reducing gas. Thermodynamics does not give straight information about the rate of the solid-gas reactions. In contrast, reaction kinetics provides information about

how fast the reaction occurs and helps identify the rate-limiting step that controls the overall reaction rate.

2.2.1. Thermodynamics of hydrogen-based direct reduction of iron ores

The feasibility of a chemical reaction is determined by the Gibbs free energy (ΔG) of the reaction under given conditions, which depends on the temperature, enthalpy (ΔH) and entropy (ΔS) changes. A reaction can be enthalpy- or entropy-driven. The Gibbs free energy change of a reaction allows us to predict whether the reaction is spontaneous in the forward ($\Delta G < 0$, called exergonic *i.e.,* work-producing) or reverse ($\Delta G > 0$, called endergonic, *i.e.,* work-consuming) direction. Spontaneous reactions refer to chemical reactions that can occur without external energy input. The sign of ΔG depends on the enthalpy (ΔH) and entropy (ΔS) changes and the temperature (K), as described by the Eq. 2.1;

$$\Delta G = \Delta H - T\Delta S \qquad 2.1$$

When $\Delta G < 0$; the reaction is endothermic with no need for external energy (*e.g.,* heat) to the system for reaction to occur in the forward direction. When $\Delta G > 0$; the reaction is endothermic where external energy needs to be supplied for the reaction to occur. When $\Delta G = 0$, the reaction is in equilibrium.

In a solid-gas reaction, under isothermal conditions, the thermodynamic driving force of the reaction, $\Delta G_{reaction}$, is controlled by the composition of the gas phase. For HyDR, it can be expressed along Eq. 2.2;

$$\Delta G_{reaction} = \Delta G^o + RTlnQ \qquad 2.2$$

wherein ΔG^o represents the standard Gibbs free energy of the reaction, while Q is the reaction quotient at any given moment. For the reaction $Fe_2O_3 + 3H_2 \rightarrow 2Fe + 3H_2O$, the reaction quotient is expressed as $Q = (\frac{P_{H_2O}}{P_{H_2}})$, where P_{H_2} and P_{H_2O} denote the partial pressures of H_2 and H_2O, respectively. The value of Q ranges from zero (representing conditions of pure H_2) to infinity (representing conditions of pure H_2O). An increase in the value of P_{H_2} thus lowers Q, and hence the overall thermodynamic driving force of the chemical reaction increases (*i.e.,* decreasing ΔG to more negative value) [28].

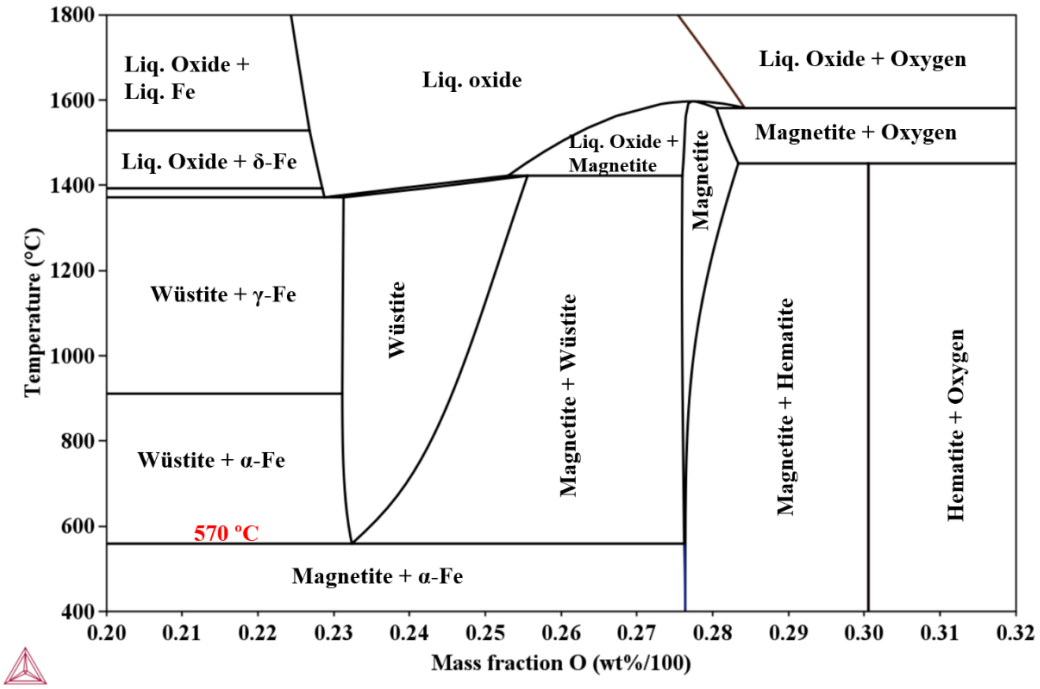

Fig. 5. Fe-O binary phase diagram at 1 atm pressure calculated with Thermo-Calc 2021b (Database: TCOX10: Metal Oxide Solutions v10.1 [29])

The solubility of oxygen is discarded in the iron-oxygen phase diagram, **Fig. 5**., since it is extremely small in α-Fe (4.65×10^{-5} wt.% at 700 ºC [30]) and γ-Fe ($<1.00 \times 10^{-3}$ wt.% [31]). Iron forms three stable oxides with oxygen; hematite (Fe_2O_3), magnetite (Fe_3O_4), and wüstite ($Fe_{(1-x)}O$). The crystal structures of these iron oxide phases are composed of closely packed layers of oxygen anions with iron cations occupying the octahedral and tetrahedral interstitials. Hematite is isostructural with corundum. It has a hexagonal unit cell with a=5.034 Å and c=13.775 Å, containing six formula units per unit cell, **Fig. 6**a. Hematite can also be indexed in a rhombohedral system with a=5.034 Å and α=55.3º and there are two formula units in the unit cell [32]. Magnetite has an inverse spinel (cubic) structure containing closely packed 32 oxygen anions (a=8.396 Å) with 24 iron cations ($16Fe^{3+}$ and $8Fe^{2+}$) distributed in the octahedral and tetrahedral interstitial sites, **Fig. 6**b [33]. Wüstite has a defective halite (rock salt) structure where oxygen anions form a close-packed cubic structure, **Fig. 6**c. Most of the octahedral sites are occupied by Fe^{2+} cations with a small portion of Fe^{3+} to maintain charge neutrality. Because wüstite exhibits a cation-deficient phase (non-stoichiometry), represented as $Fe_{(1-x)}O$ where 1−x varies between 0.83 and 0.95. The lattice constant of wüstite is determined by its stoichiometry (*e.g.,* 4.280 Å at 1−x=0.89; 4.310 Å at 1−x=0.95) [32, 34].

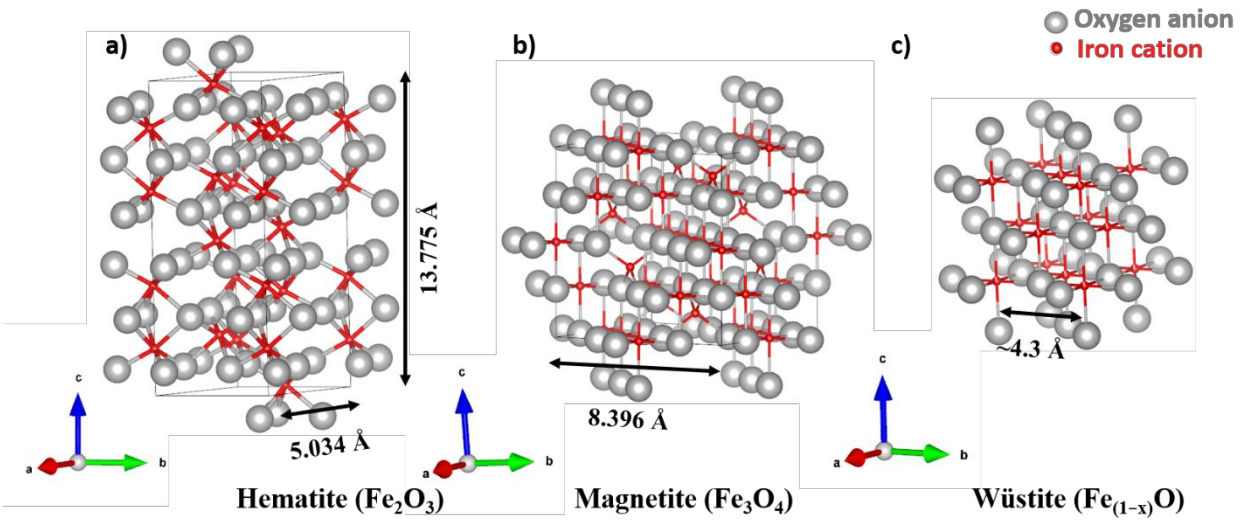

Fig. 6. The illustration of crystal structure of (a) hematite, (b) magnetite, (c) wüstite. The black arrows indicate the lattice parameters of respective directions. The grey spheres represent oxygen anions (O^{2-}) and the red spheres represent iron cations (Fe^{2+} and Fe^{3+}). Produced with VESTA (Visualization for Electronic and Structural Analysis) Ver. 3.5.7.

The stability of the iron-oxygen binary phases can be evaluated based on the temperature and gas composition (*e.g.,* CO-CO_2 and H_2-H_2O). Baur−Glässner diagram illustrates the stability region of different phases as a function of temperature and gas oxidation degree (GOD), **Fig. 7**. The gas oxidation degree can be defined as the ratio of oxidized gas components (*i.e.,* H_2O or CO_2) to the sum of both oxidized and oxidizable gas components, such as H_2 and CO, in the gas environment. The lower GOD indicates a higher driving force of the reaction, driven by the increased partial pressure of the oxidizable gas.

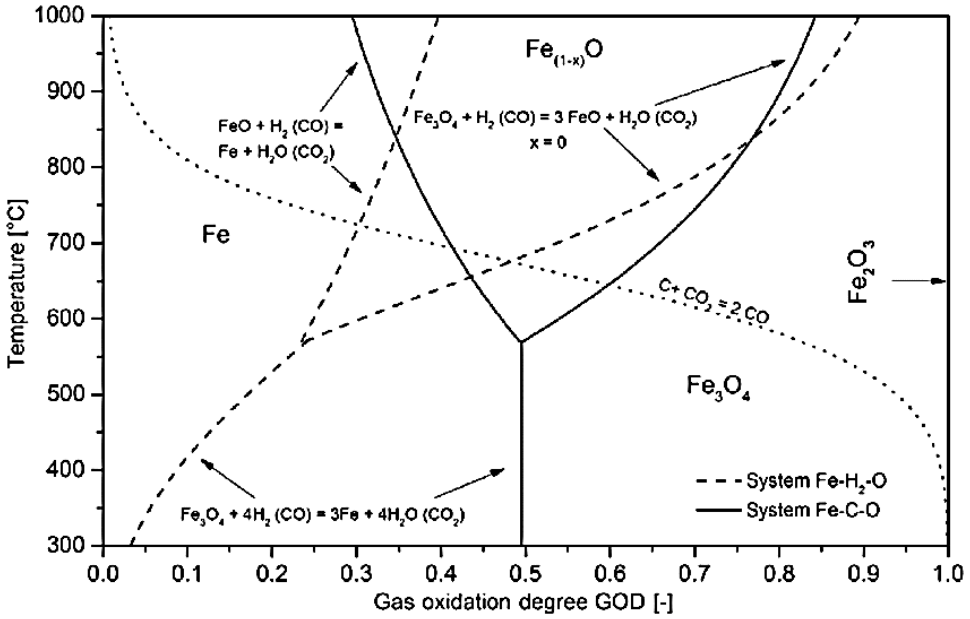

Fig. 7. Baur–Glässner diagram for the Fe–O–H system, marked with a dashed line, and for the Fe–O–C system marked with a solid line. The dotted line represents the equilibrium line for the Boudouard reaction. The diagram was plotted for 1 bar and a carbon activity of 1. It represents the stability ranges of different phases as a function of temperature and oxidizing power of the gas (GOD). Adopted from ref [35].

At temperatures below ~850 ºC, iron has a broader stability range in CO/CO_2 atmosphere than in H_2/H_2O atmosphere. This means that, at low temperatures, the thermodynamic driving force of reduction with CO is higher than that of at high temperatures, the opposite being true for H_2. To ensure complete reduction with H_2, iron oxide should be reduced at the highest possible temperature in a controlled gas atmosphere (*e.g.,* $\frac{P_{H_2}}{P_{H_2}+P_{H_2O}}$ >0.7 at 700 ºC for complete reduction). As the stability range of iron narrows at lower temperatures, the driving force for reduction decreases, which can lead to reoxidation of DRI. For this reason, cooling should be conducted in a gas atmosphere with a high H_2 concentration (*e.g.,* $\frac{P_{H_2}}{P_{H_2}+P_{H_2O}}$ >0.95) to prevent reoxidation [35].

The Ellingham diagram visually shows how ΔG changes for the redox reaction of metal oxides with temperature as well as the corresponding oxygen pressures in equilibrium, **Fig. 8**. The stability of metal oxides decreases from the lower (*e.g.,* Ca and Mg) to the upper portion (*e.g.,* Cu and Fe) of the Ellingham diagram. This means that the reducibility of the metal oxides in the upper part of the diagram is larger than that of metal oxides in the lower portion. The slope of the reaction lines is proportional to the ΔS which is constant with temperature. The ΔG for CO_2 remains relatively stable across different temperatures. In contrast, the ΔG of CO shows a negative slope

on the Ellingham diagram. At ~700 °C, the ΔG lines for CO_2 and CO intersect. This intersect point is significant because it indicates a shift in the stability of carbon oxides: above this temperature, CO becomes the more stable oxide compared to CO_2. According to the Boudouard reaction ($C_{(s)}+CO2_{(g)}\rightarrow 2CO_{(g)}$), higher temperatures favor the formation of CO over CO_2. Consequently, at temperatures above 700 °C, CO acts as a stronger reducing agent, making it more capable of reducing metal oxides, such as iron oxides. The Ellingham diagram is commonly employed in extractive metallurgy to identify suitable reducing agents, determine the necessary reaction temperatures, and assess the required gas composition for the reduction of metal oxides.

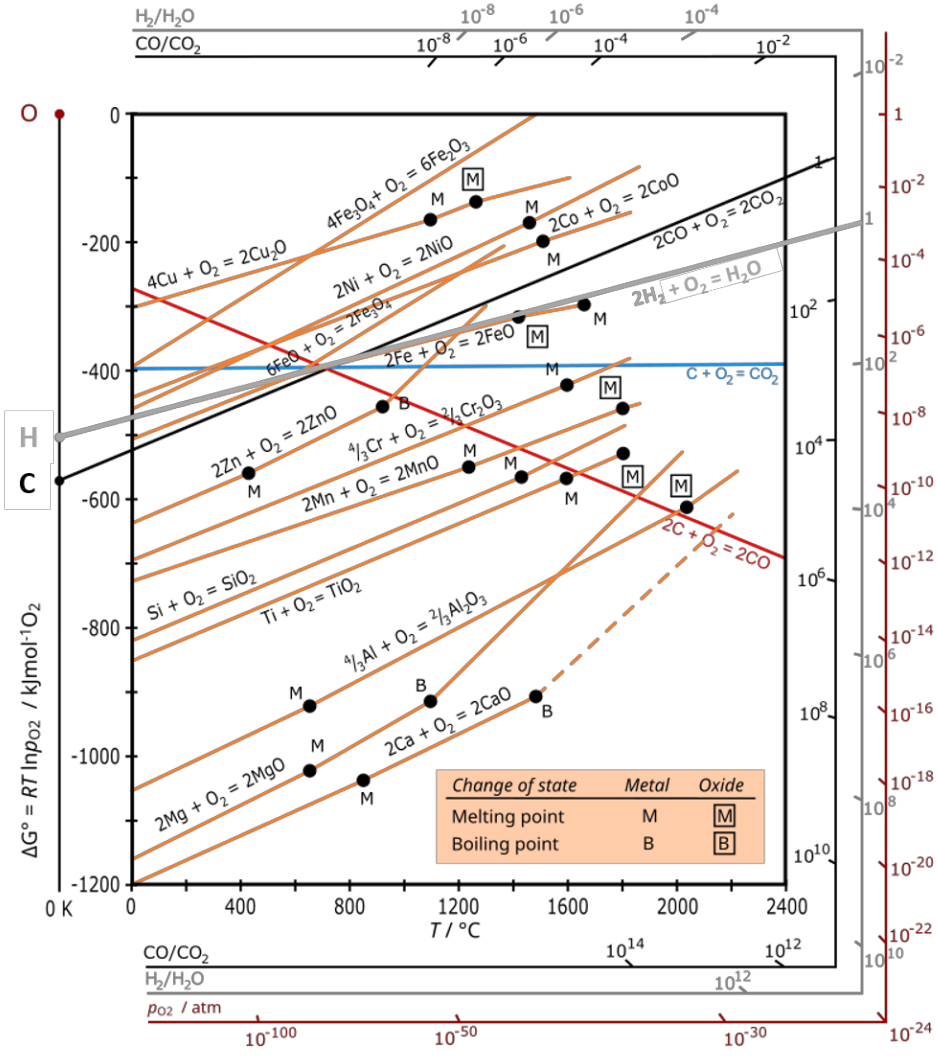

Fig. 8. The Ellingham diagram for various metals shows the free energy of the formation of metal oxides and the corresponding equilibrium oxygen partial pressure. Adopted from REF [36].

2.2.2. The kinetics of hydrogen-based direct reduction

The reduction of hematite is a multistep solid-gas reaction in which hematite is first reduced to magnetite (2.3), followed by wüstite (2.4), and finally to metallic iron (2.5) above 570 °C. Below this temperature wüstite is not thermodynamically stable, see **Fig. 5**, thus Fe is transformed from magnetite without the formation of the wüstite phase (2.6).

$$3Fe_2O_3 + H_2 \rightarrow 2Fe_3O_4 + H_2O \quad (2.3)$$

$$Fe_3O_4 + H_2 \rightarrow 3FeO + H_2O \; T>570\ °C \quad (2.4)$$

$$FeO + H_2 \rightarrow Fe + H_2O \quad (2.5)$$

$$Fe_3O_4 + 4H_2 \rightarrow 3Fe + 4H_2O \; T<570\ °C \quad (2.6)$$

During HyDR, the reaction proceeds as follows; (1) transfer of H_2 molecules to the reaction surface, (2) dissociation of H_2 molecules into mono-atomic hydrogen form (H), and subsequent adsorption of H atoms into vacant interstitial sites at the iron oxide surfaces [37, 38], (3) chemical reaction between hydrogen atoms and oxygen, *e.g.,* formation of H_2O molecules, iron cations, and vacancies (4) desorption of H_2O from the reaction surface, and (5) mass transfer of H_2O back to the gas stream. The reaction sequences of step (2) and step (3) are represented as follows; $H_2 + 2Va^* \rightarrow 2H^*$, $H^* + O^{2-} \rightarrow OH^- + e^-$ and $OH^- + H^* \rightarrow H_2O + e^-$. Va* donates a vacant interstitial site where H_2 molecules dissociate into mono-atomic hydrogen.

The reduction of iron oxide with H_2 starts at the particle surface. As the reaction proceeds, a product layer (*e.g.,* magnetite, wüstite, or iron) forms on the surface, resulting in the development of the oxide-oxide (*e.g.,* hematite-magnetite and magnetite-wüstite) and metal-oxide (*e.g.,* wüstite-iron) phase boundaries. Reactions occur on the solid-gas and solid-solid interfaces. **Fig. 9**. illustrates the mechanism of the iron oxide reduction with H_2 at the atomic scale. At the initial stage of the reduction (*e.g.,* from hematite to magnetite), dissociated hydrogen atoms (H*) remove oxygen anions from the surface, resulting in an increased concentration gradient of Fe^{2+} cations in the magnetite layer. Fe^{2+} cations and electrons diffuse to the internal reaction interface and transform hematite into magnetite ($Fe_2O_3 + Fe^{2+} + 2e^- \rightarrow 3Fe_3O_4$), **Fig. 9**a. The reduction in the magnetite/wüstite proceeds similarly ($Fe_3O_4 + Fe^{2+} + 2e^- \rightarrow 4FeO$).

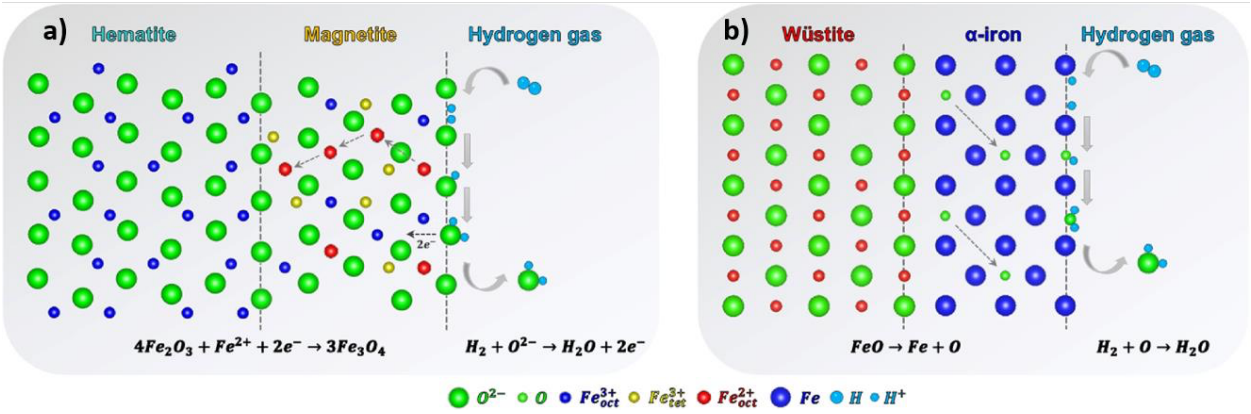

Fig. 9. Illustration of the atomic-scale mechanism of hydrogen-based direct reduction: a) reduction of hematite to magnetite, and b) reduction of wüstite to iron. Adopted from ref [30].

During the initial (hematite to magnetite) and intermediate (magnetite to wüstite) reduction steps, phase transformations are driven by the activity gradient of iron cations and their subsequent ionic diffusion to the internal reaction interfaces. However, at the final stage of reduction (from wüstite to iron), a dense iron layer forms on the oxide surface. The phase transformation from wüstite to iron (FeO → Fe + O) is governed by the oxygen activity gradient, extending from the metal-oxide interface to the external metal-gas interface, **Fig. 9**b. This step is considered the most sluggish step of reduction since the solubility (in α−Fe, 4.65×10^{-5} wt.% at 700 °C) and diffusivity (at 700 °C in α−Fe, 2.160×10^{-11} m^2/s) of oxygen in iron is very small. Therefore, the outbound diffusion of oxygen is mostly governed by the pore surface, cracks, and other defects (*e.g.,* grain boundary) [6, 30].

2.2.2.1. The effect of the reduction parameters on the reduction kinetics

The reduction of iron oxide with H_2 is influenced by reaction parameters such as temperature, gas flow rate, gas pressure, and gas composition [35]. These parameters play a critical role in determining the kinetics and overall efficiency of the reduction process. In the following sections, the individual effects of temperature, gas flow, gas pressure, and gas composition on the reduction of iron oxide will be discussed.

The overall reaction in HyDR is endothermic, making temperature the most critical parameter influencing reaction kinetics. The reduction rate of iron oxides with pure H_2 increase significantly with rising temperature [39-45]. Because, according to the Arrhenius equation, the reaction rate constant, k, depends exponentially on $-Ea/RT$, where Ea is the activation energy (to be overcome

initiate reaction), R is the gas constant, and T is the absolute temperature. Additionally, higher temperatures enhance the diffusion rates of reactive species and increase the velocity of the reaction interface [28, 46]. Thus, maintaining a high-temperature range (to be determined based on P_{H_2} in the reducing gas, **Fig. 7**) throughout the HyDR process is crucial for optimizing the reduction rate.

The composition of the reducing gas is another key factor influencing the reduction kinetics of iron oxides. In the reducing gas mixtures, containing H_2, H_2O, CO, CO_2, and CH_4, the ratio of H_2 plays a critical role in determining the reaction rate. Reduction with H_2 is faster than CO because H_2 diffuses and percolates faster than CO [47-49]. When the rate-limiting step is the mass transport of the reducing gas to the reaction front, an increase in H_2 in the reducing gas mixture enhances the reduction kinetics while an increase in the CO in the reducing gas mixture slows down the reduction kinetics [48]. In industrial applications, adjusting the partial pressure of H_2 and CO is not only critical for reaction kinetics but also for the post-steelmaking process and energy consumption. Because using 100% H_2 can result in high energy consumption due to the endothermic nature of the reaction, exothermic reactions with CO help save energy and facilitate the carbon deposition (*i.e.,* carbon deposition on the iron surface through the Boudouard reaction) on iron which is needed for steel production [50]. Therefore, incorporating CO into gas mixtures is essential, but process parameters must be carefully optimized. For example, lowering the reduction temperature significantly increases carbon deposition on the surface. At 786 ºC with a 50% CO-H_2 gas mixture, the carbon content reaches ~0.52 wt.% as Fe_3C and ~0.12 wt.% as elemental carbon. At 700 ºC, these values rise to ~0.55 wt.% as Fe_3C and ~0.20 wt.% as elemental carbon [49]. Excessive carbon deposition can hinder the mass transport of reducing gas to the reaction surface by forming a dense Fe_3C layer on the iron surface and preventing further reaction.

In addition to the composition of the reducing gas, the pressure of the reducing gas plays a significant role in the rate of reduction kinetics. The effect of hydrogen gas pressure has been studied in the literature for pure gases (e.g., H_2 and CO) [51-53] and gas mixtures (*e.g.,* H_2, H_2O, CO, CO_2, and CH_4) [54, 55]. Studies have identified two major effects of reducing gas pressure:

- An increase in the absolute pressure does not have a substantial effect on reduction kinetics [52, 55];

- Increasing the partial pressure of the reducing gas (*e.g.*, $P_{H_2(or\ CO)} / (P_{H_2(or\ CO)} + P_{H_2O(or\ CO_2)})$ enhances the reduction kinetics by facilitating faster counter-current diffusion of the gaseous reactants and products associated with the underlying redox reactions [47, 52, 56, 57].

In HyDR, increasing H_2 pressure has been shown to enhance the net diffusion of H_2 through the product layer while improving the mass transport of the reducing gas to the reaction zone. In addition, an increase of $P_{H_2(or\ CO)}$ decreases the Gibbs free energy of a solid-gas reaction, see Eq. (2.2).

2.2.2.2. The effect of microstructure on the reduction kinetics

Next, the role of defects in the iron ore pellet during HyDR and influence of these defects on the reduction process will be discussed and how microstructural changes occur due to various factors is explained. The type of defects in the solid feedstock (hematite pellet) divided into two classes, namely, inherited defects and acquired defects. The former addresses the starting microstructure of the pellet which defects were inherited from the pellet preparation process. **Fig. 10**. represents the overview of the microstructure of a hematite pellet. As depicted in Figs. 10a-c, the pellet consists of Fe_2O_3 grains **Fig. 10**c, pores (inherited from the pelletizing process), and gangue oxides such as SiO_2 (1.0 to 6.2 wt.%), CaO(0.1 to 2.4 wt.%), MgO (0.2 to 2.6 wt.%), Al_2O_3 (0.2 to 2.7 wt.%), etc. [58], **Fig. 10**d. The latter is acquired in the course of solid-state reaction of the hematite pellet with H_2.

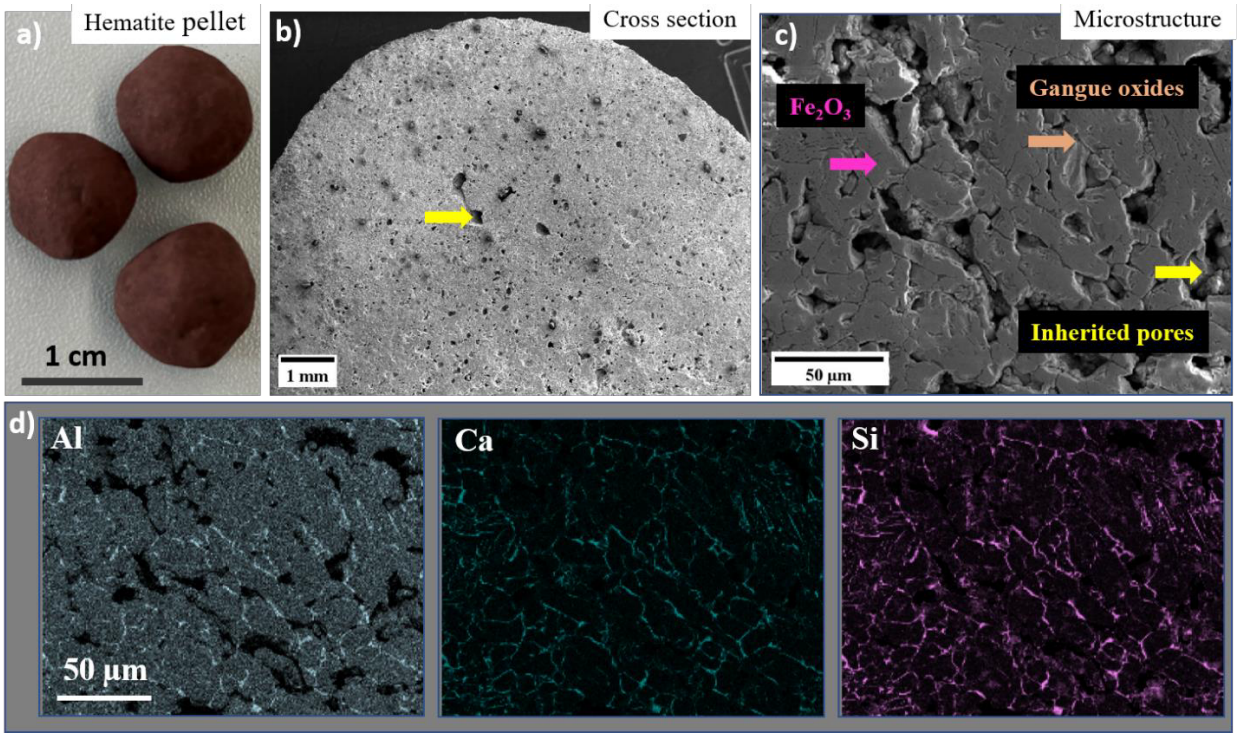

Fig. 10. Overview of the hematite pellet's morphology and microstructure. a) Macroscopic view of the hematite pellets showing their size and shape, consisting of 0.36 wt.% FeO, 1.06 wt.% SiO_2, 0.40 wt.% Al_2O_3, 0.73 wt.% CaO, 0.57 wt.% MgO, 0.19 wt.% TiO_2, 0.23 wt.% V, 0.10 wt.% Mn, with traces of P, S, Na, K, and Fe_2O_3 in balance. b) Cross-sectional SEM image highlighting the inherited pores (yellow arrow). c) The SE image of the microstructure, showing hematite (Fe_2O_3) grains (pink arrow), gangue oxides (orange arrow), and inherited pores (yellow arrow). d) Elemental mapping of Al, Ca, and Si distributions, illustrating the spatial presence of gangue oxides in the pellet matrix.

During HyDR, the microstructural changes occurs via gradual acquired defect evolution. The evolution of defects modifies the local reaction conditions, such as gas composition, mass transport mechanism of gas molecules, and diffusion of anions and cations. These defects occur due to following reasons:

- Loss of mass and volume due to the removal of oxygen, *i.e.,* formation of vacancies and their subsequent coalescence to forms void and pores
- Non-volume conserving and non-commensurate nature of phase transformations, and formation of product phases *i.e.,* different crystal structure of iron oxide phases led to lattice mismatch, creating internal stress and crystal defects
- Local accumulation of the reaction product (H_2O), and subsequent crack formation
- Hydrogen-induced weakening and separation at metal/oxide interfaces

- Thermal stress induced with the presence of impurities (gangue oxides); formation of delamination or crack due to the different thermal expansion properties of impurities, and iron/iron oxide phases.

The evolution of the microstructure of a hematite pellet depends on the reaction boundary conditions *e.g.,* temperature, and H_2 gas pressure [6, 24, 30, 41, 59]. Porosity and its morphology represent critical microstructural features that significantly influence reduction kinetics. Thus, next, the pore formation mechanism and their potential effect on the reduction kinetics and mass transport mechanisms will be discussed.

2.2.2.2.1. Role of pores on reduction kinetics

A reduced pellet contains two types of pores: inherited and acquired. Inherited pores originate from the pelletizing process (*i.e.,* form during the sintering of fine iron oxide particles into commercial pellets, *i.e.,* 10-16 mm in diameter, before reduction.), while acquired pore formation is driven by mass and volume loss due to oxygen removal during the reduction process. In the literature, the formation of acquired pores is attributed to the following reasons [60-62]:

- Coalescence of vacancies inherited from the removal of oxygen from the oxide lattice [63].
- Volume changes associated with the transformation from trigonal hematite to cubic magnetite, and from cubic magnetite into body-centered iron [61]
- Bursting mechanism (a.k.a. breakdown mechanism) resulting from the formation and breakdown of dense iron layers on the oxide surface [62]
- Continuous coupled growth of pore and iron (*i.e.,* formation of elongated pore structure) arising from a continuous coupled reaction with simultaneous iron and pore formation at a planar growth front [64]

Vacancy coalescence mechanism: During the reduction of iron oxide, oxygen anions (O^{2-}) are removed from the iron oxide lattice through a chemical reaction with hydrogen (H_2). When an oxygen anion leaves the lattice, it creates a vacancy. These oxygen vacancies do not remain isolated. Instead, they migrate and coalesce to form voids at the reaction interface where reduction occurs [63, 65]. Newly formed vacancies continue to move and contribute to the already-formed voids, further reducing the overall energy by minimizing the surface area [66]. This process results in the formation of acquired pores in the material as reduction progresses.

Breakdown (bursting) mechanism: During the reduction of iron oxide to iron, the removal of oxygen from the surface increases the local concentration of iron. This creates a chemical potential gradient between the wüstite surface and the bulk wüstite, driving the diffusion of iron ions toward the bulk wüstite ($Fe_{1-x}O$; $0.83 < 1–x < 0.95$). As the reduction progresses, the concentration of iron ions in wüstite increases until it becomes saturated ($Fe_{1-x}O$; (1–x) approaches 0.95). The excess iron accumulates, leading to the formation of iron clusters and nucleation sites. These iron nuclei continue to grow as the reduction of wüstite progresses, **Fig. 11**a. A dense iron layer forms when the metallic iron phase grows faster than the gas/oxide reaction interface advances, **Fig. 11**b(i). If voids are present at the metal/oxide interface, the accumulation of H_2 and H_2O can create gas bubbles, **Fig. 11**b(ii). When the gas pressure within these bubbles exceeds the external reducing gas pressure, the dense iron layer breaks down, leading to the formation of porous iron through a discontinuous breakdown mechanism, **Fig. 11**b(iii). However, if the dense iron layer remains in contact with oxide, its thickness increases, and the reduction process becomes controlled by the solid-state diffusion of oxygen through the dense iron layer. Under low chemical driving forces, the growth rate of the metal phase would exceed that of the pores.

Continuous coupled growth: After iron nucleation on the wüstite surface, if the growth rates of pores and iron phase are equal, a coupled growth of two phases (e.g., metallic iron and H_2O vapor) mechanism occurs, **Fig. 11**c. In this case, the boundary between the oxide (wüstite) and iron grows in a planar geometry as the reduction progresses. However, this geometry is maintained under a high chemical driving force for reaction to ensure that the pores and the iron phase advance together at the same rate, keeping the reaction front stable and planar. If the rate of advance of the gas/oxide interface is faster than the growth of the metallic phase**,** pores or tunnels will continue to develop and extend deeper into the oxide [62, 67-70].

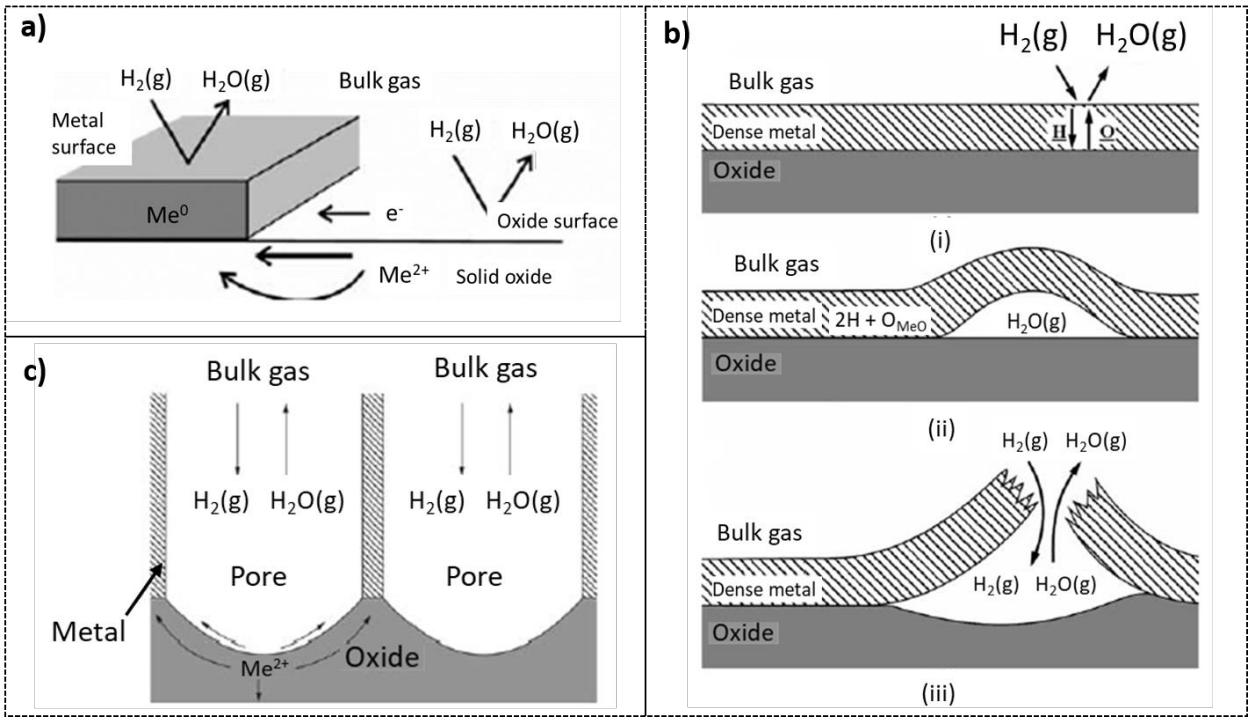

Fig. 11. a) The process of metal (Me^0) formation involves the removal of oxygen from the oxide surface by reaction with H_2 gas, forming H_2O, accompanied by the diffusion of metal cations (Me^{2+}) and electron transfer at the reaction interface. (b) Breakdown mechanism: Morphological evolution at the reaction interface under varying conditions: (i) Formation of dense metal layers due to oxygen removal. (ii) Growth of instability at the interface, driven by local chemical gradients and gas transport. (iii) Complete breakdown of the dense layer, leading to pore formation and exposure of the oxide surface to the reducing gas. (c) Continuous coupled growth: Formation of pores at the metal/oxide interface during reduction, driven by the removal of oxygen ions and the local accumulation of Me^{2+} ions at the reaction front. Pore geometry evolves continuously with growth of metal (iron) phase. Adopted from ref [28]

Porosity plays a crucial role in understanding the reaction mechanism. Pore surface provides fresh surfaces for the reaction to occur. Open pores provide effective pathways for the inbound diffusion of H_2 to the reaction front and the outbound diffusion of H_2O to the gas stream. In contrast, isolated pores (*i.e.,* no opening to the gas stream) can lead to the accumulation of H_2O molecules within the isolated pore, altering the local thermodynamic equilibrium. Changing the thermodynamic equilibrium conditions (*e.g.,* changing the partial pressure of H_2 and H_2O, see Baur Glässner diagram, **Fig. 7**.) in the isolated pore can result in the reoxidation of the isolated pore surfaces, decreasing the efficiency of the reduction process [61, 71]. Zhou et al. investigated the effect of pore formation on redox-driven phase transformations during the hydrogen-based reduction of wüstite to α-Fe by the combination of nanoscale microscopy and phase-field simulations. They demonstrated that H_2O trapped in isolated pores led to local reoxidation, resulting in the formation of a thin wüstite layer on isolated pore surfaces, **Fig. 12**. This reoxidation effect hinders reduction kinetics and reduces overall metallization efficiency (*i.e.,* ~5%).

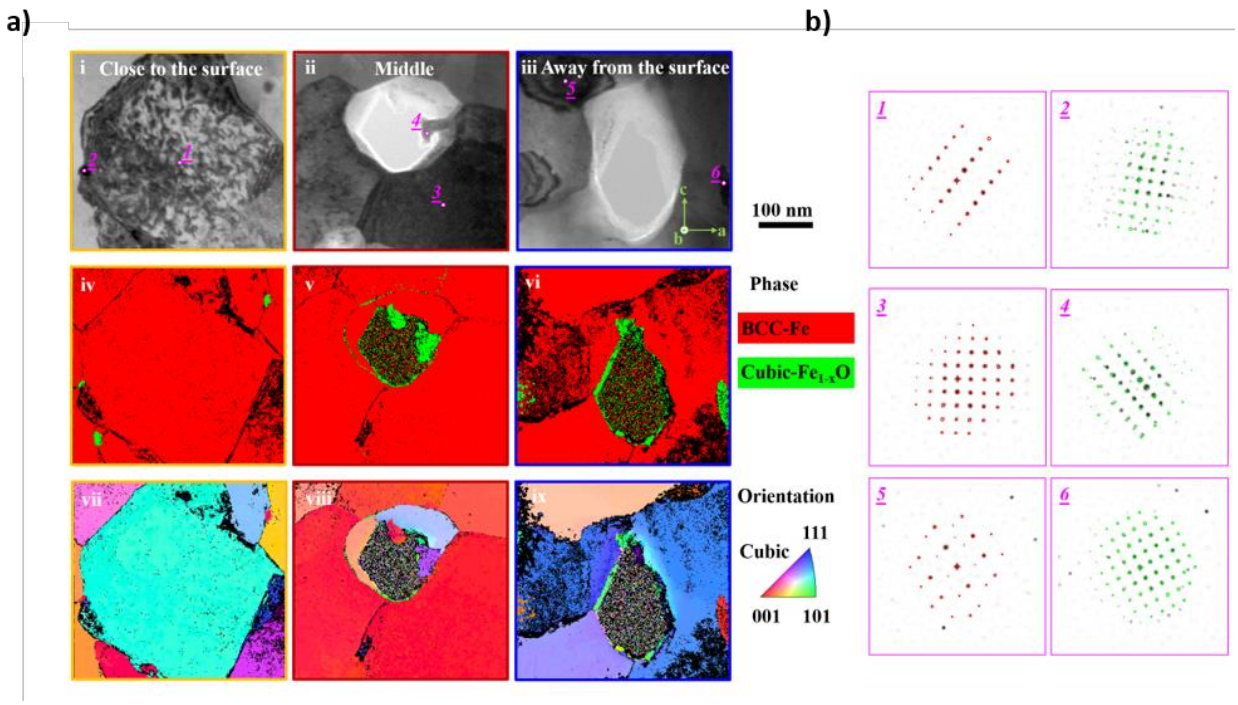

Fig. 12. Reoxidation of isolated pore surface on the single crystal wüstite ($Fe_{1-x}O$) after reduction with 100% H_2 at 700 °C for 2h. (i–iii) Bright-field images of different regions of the reduced wüstite taken with scanning transmission electron microscopy: (i) close to the single crystal surface, (ii) middle, and (iii) deeper regions, showing the increase in pore size from surface to the deeper regions. (iv-vi) Phase maps of α-Fe (red) and cubic wüstite (green) phases, with the surface region predominantly reduced to α-Fe, while wüstite persists in particularly near pores. (vii-ix) Inverse pole figures of grains showing crystallographic orientations in the cubic phase. (1–6) Corresponding diffraction patterns from numbered regions in the bright field images (i–iii), confirming the presence of wüstite in the isolated pore surface. Adopted from ref [61].

The morphology and size of pores influence the mass transfer mechanism of H_2 and H_2O and the reaction kinetics of the HyDR of iron oxide. The size of pores increases with temperature [14, 30, 44, 67, 72]. For instance, Turkdogan et al. [73] reported growth of mean pore diameter from approximately 0.09 µm at 600 °C to 6 µm at 1200 °C. Larger pores are advantageous for faster reduction kinetics, as they reduce the chance of turbulent flow of gas within the pore channel and enhance effective gas diffusion [74]. Under a highly reactive environment (*i.e.,* high partial pressure of H_2), pores tend to be finer, uniformly distributed, and random in shape which is associated with rapid oxygen removal [53, 60, 62]. Conversely, under less reactive conditions, large and elongated pore structures form, often associated with slower reduction rates [75]. These dynamic changes in pore size and structure, influenced by temperature, H_2 pressure, and the rate of reduction, underscore the importance of understanding the gas dynamics with pores to optimize reaction conditions for efficient hydrogen-based direct reduction [67, 76, 77].

Paul et al. [77], investigated gas transport dynamics within iron oxide pellets during HyDR, focusing on the roles of pore connectivity, particle refinement, and gas permeability. By combining nano- and micro-computed X-ray tomography to reconstruct 3D images of the pore network, gas permeability measurements to evaluate hydrogen and water vapor transport, and percolation theory with slip-flow permeability modeling, they analyzed the relationship between pore structure, gas transport properties, and reduction kinetics. A percolation threshold of 0.1 ± 0.007 porosity is determined for pore connectivity. In other words, pore connectivity is achieved when porosity exceeds 10%. The study found that 70% of the pores, ranging from 0.3 to 10 μm in size, correspond to Knudsen numbers (K_n: the ratio of the mean free path of gas molecules to pore diameter) between 0.01 and 1.0, representing slip and transitional flow regimes. In the slip flow regime, gas-wall interactions dominate hydrogen flow. At the pellet scale, where pore sizes range from 0.1 to 100 μm, the Knudsen mechanism dictates gas flow dynamics, making pore size a critical factor in defining hydrogen transport through channels inside or between pellets. However, at the reactor scale, macroscopic continuum flow dominates (*i.e.,* gas behavior becomes independent of channel size). These fluid dynamic mechanisms, combined with hydrogen concentration as the primary chemical driving force, determine local equilibrium and gas transport efficiency in HyDR reactors. Various types of pores have been described in the literature, with their amount, size, and shape closely linked to the chemical reaction rate [62, 78-81]. Understanding the interplay between pore size, fluid dynamics, and chemical equilibrium is essential for optimizing hydrogen flow and reduction efficiency in industrial processes.

3. GREEN IRONMAKING AT HIGHER H_2 PRESSURE: REDUCTION KINETICS AND MICROSTRUCTURAL FORMATION DURING HYDROGEN-BASED DIRECT REDUCTION

This chapter is based on the publication: Özge Özgün, Imants Dirba, Oliver Gutfleisch, Yan Ma, Dierk Raabe (2024). Green ironmaking at Higher H2 pressure: reduction kinetics and microstructure formation during hydrogen-based direct reduction of hematite pellets. *Journal of Sustainable Metallurgy*, *10*(3), 1127-1140.

Hydrogen-based direct reduction (HyDR) of iron ores has attracted immense attention and is considered a forerunner technology for sustainable ironmaking. It has a high potential to mitigate CO_2 emissions in the steel industry, which accounts today for ~8-10% of all global CO_2 emissions. Direct reduction produces highly porous sponge iron via natural-gas-based or gasified-coal-based reducing agents that contain hydrogen and organic molecules. Commercial technologies usually operate at elevated pressure, *e.g.*, the MIDREX process at 2 bar and the HyL/Energiron process at 6-8 bar. However, the impact of H_2 pressure on reduction kinetics and microstructure evolution of hematite pellets during HyDR has not been well understood. Here, we present a study about the influence of H_2 pressure on the reduction kinetics of hematite pellets with pure H_2 at 700 °C at various pressures, *i.e.,* 1, 10, and 100 bar under static gas exposure, and 1.3 and 50 bar under dynamic gas exposure. The microstructure of the reduced pellets was characterized by combining X-ray diffraction (XRD) and scanning electron microscopy (SEM) equipped with electron backscatter diffraction (EBSD). The results provide new insights into the critical role of H_2 pressure in the HyDR process and establish a direction for future furnace design and process optimization.

3.1. Introduction

Steel is the foundation material of modern civilization, serving in construction, infrastructure, machinery, transportation, *etc*. Its massive annual production has approached 2 billion tons per year in 2023 [19]. Currently, the established integrated route of iron- and steelmaking, providing 2/3rd of the global market, proceeds in a two-step process. The first one consists of the reduction of iron oxides to pig iron, a near-eutectic Fe-C compound, in blast furnaces. The second one is steelmaking, which consists of the conversion of pig iron to steel (usually with a much lower C content of 0.01-0.4 wt.%) in a basic oxygen furnace [1]. However, this integrated route is based on the use of fossil agents (*i.e.*, coal and coke) as energy sources and reducing agents, leading to 1.9-2.2 tons of CO_2 emissions per ton of steel. Thus, the steel industry alone accounts for ~8-10% of global CO_2 emissions [1]. To reduce these immense CO_2 emissions from the steel sector and thus cap the biggest single contributor to global warming, hydrogen is considered a promising alternative to carbon-based reductants, given that hydrogen can be produced in the required amounts by electrochemical or plasma processes using renewable electrical energy [30, 82]. In this context, hydrogen-based direct reduction (HyDR) is the most compelling technology for green ironmaking due to its high technology readiness level, that is TRL 6-8 [3]. HyDR is a multistep solid-state reaction, where iron ores (hematite or magnetite) are gradually reduced to iron at high temperatures of 500-1100 °C [35]. H_2 reduces the iron oxides by reacting with the chemically bound oxygen and the reaction sequence proceeds gradually from iron's highest to its lowest oxidation state, *i.e.*, through hematite (Fe_2O_3) to magnetite (Fe_3O_4), wüstite ($Fe_{1-x}O$, where x indicates the deficiency of Fe in the lattice), and metallic iron (Fe). At temperatures below 570 °C, wüstite is thermodynamically unstable, and thus magnetite is directly reduced to metallic iron.

Direct reduction is a mature technology and ~125 million tons of steel were produced in 2021 via steam-reformed natural-gas-based and gasified-coal-based direct reduction [19]. The commercial reduction technologies used today are usually operated at elevated pressures. For example, the MIDREX and HyL/Energiron processes, using iron ore pellets (10-16 mm in diameter), are operated at 2 bar and 6-8 bar total pressure, respectively [24-27]. These operating pressures refer to the total gas pressure values of the charged reductant mixtures. In the MIDREX process hydrogen ratio in the reducing gas mixture (*i.e.*, H_2, CO, CH_4, CO_2, and H_2O) is typically in the range of 55-80% [21]. In the MIDREX reduction method, methane (CH_4) goes first through a gas

reforming step wherein a mixture of H_2 and CO reductants is produced in a reformer via the following reactions: $CH_4+H_2O \rightarrow 3H_2+CO$ and $CH_4+CO_2 \rightarrow 2H_2+2CO$ (H_2O and CO_2 are obtained by collecting the off-gas of the shaft furnace). The reformed gas is then purged into the shaft furnace to reduce iron oxide [22]. In the HyL/Energiron process variants, there is no separate reformer system and the reducing gases are generated by *in-situ* reformation of natural gas inside the shaft furnace. The use of elevated pressure conditions facilitates the dissociation of methane over the iron ore pellets in the shaft furnace (*e.g.,* the HyL/Energiron Zero Reformer process). The CIRCORED process is another solid-state reduction furnace variant. It is based on a fluidized bed principle and is operated at 4 bar to enable the fluidization of fine iron ore particles (50-100 μm) [24, 83-88].

In terms of the reduction kinetics, the effects of the pressure of the pure reducing gases (*e.g.*, H_2, and CO) [51, 52] and reducing gas mixtures (*e.g.*, H_2, H_2O, CO, CO_2, and CH_4) [54, 55] have been investigated in the literature. It has been found that the pressure of reducing gas mixture has two major effects: (1) An increase in the absolute pressure (*e.g.,* gas mixtures with total pressure from 1 to 3 bar containing 0.55 bar H_2, 0.09 bar CO, 0.05 bar CO_2 and N_2 in balance) does not have a substantial effect on reduction kinetics [52, 55]; (2) Increasing the partial pressure of the reducing gas (*e.g.,* $P_{H_2(or\ CO)} \ / \ (P_{H_2(or\ CO)} + P_{H_2O(or\ CO_2)})$ enhances the reduction kinetics by facilitating faster counter-current diffusion of the gaseous reactants and products associated with the underlying redox reactions (*e.g.*, increasing P_{H_2} from 0.55 to 1.65 bar doubled the reduction rate at the initial and medium stages of reduction) [47, 52, 56]. For HyDR, it has been suggested that an increase in H_2 pressure increased the net diffusion rate of the H_2 through the product layer and enhanced the mass transport of the reducing gas to the reaction zone, thus improving overall reduction kinetics by up to 25% for an H_2 pressure range of 5-35 bar [57]. The H_2 gas pressure plays an important role not only in the reduction kinetics but also in the microstructure evolution of iron ore during reduction [6, 24, 30, 41, 59]. Specifically, the reduction behavior of iron ore pellets shifts from the classical topochemical features (at ~1 bar) to spatially more homogeneous reaction features, revealed by the homogeneous distribution of the partially reduced iron oxides (magnetite and wüstite) at higher pressures of H_2 and CO gas mixtures (~3 bar) [54].

However, the impact of H_2 pressure on reduction kinetics and microstructure evolution during iron ore reduction with H_2 has not been systematically investigated and understood in terms of the

underlying mechanisms. Particularly, the local reaction behavior at the microscopic scale has remained unclear so far [89-91]. These facts make it challenging to conduct pellet, gas, and process optimization for higher efficiency and faster metallization [16, 92-95]. In the current investigation, we studied the detailed mechanisms and microstructure effects observed upon the change in H_2 pressure, to turn efforts towards further process design from an empirical to a knowledge-based approach. We investigated the influence of pressure on the reduction kinetics of hematite pellets with pure H_2 at 700 °C at various pressures, *i.e.,* 1, 10, 50, and 100 bar, under static and dynamic reductant gas exposure conditions. The microstructure of partially and fully reduced pellets was characterized by combining X-ray diffraction (XRD) and scanning electron microscopy (SEM) equipped with electron backscatter diffraction (EBSD). The local porosity evolution and grain morphology of metallic iron were thoroughly characterized to better understand the effects of H_2 pressure on the local reaction behavior. The results obtained provide new insights into the critical role of H_2 (partial) pressure in the HyDR process and establish a direction on future pellet, furnace, and process design.

3.2. Experimental Method

3.2.1. Reduction of hematite pellets with hydrogen

Commercial direct-reduction hematite pellets of 2.8±0.2 grams were used in this study, consisting of 0.36 wt.% FeO, 1.06 wt.% SiO_2, 0.40 wt.% Al_2O_3, 0.73 wt.% CaO, 0.57 wt.% MgO, 0.19 wt.% TiO_2, 0.23 wt.% V, 0.10 wt.% Mn, with traces of P, S, Na, and K, and Fe_2O_3 in balance.

The reduction of hematite pellets was performed at various pressures in two setups, namely, (1) a static gas reactor and (2) a dynamic gas reactor. In the static gas setup, hematite pellets were reduced at 700 °C for 5, 30, and 120 minutes in a custom-made high-pressure vessel inside a tube furnace with a chamber volume of 0.095 L [96]. The pure H_2 gas (99.999 % purity, Air Liquide) was pressurized at room temperature to reach 1, 10, and 100 bar at 700 °C. The pellets were heated up to 700 °C with a heating rate of 5 °C/min in hydrogen gas. It is worth mentioning that additional H_2 was supplied against potential gas leakage to maintain a constant pressure of 100 bar. After reduction, the samples were cooled down to room temperature in the furnace. The reduction parameters are listed in **Table 1**. In the dynamic gas exposure experiments, pellets were reduced in a high-pressure thermogravimetric analysis (HP-TGA, DynTHERM, TA Instrument) setup. The

gas pressures were set to be 1.3 and 50 bar (the maximal pressure allowed in the HP-TGA). The pellets were first heated to 700 °C in Ar at elevated pressures at a heating rate of 10 °C/min. When the temperature was stabilized, the gas was changed to the pressurized H_2. The gas flows were 200, and 500 mL_s/min for 1.3 and 50 bar, respectively. Real-time mass loss of hematite pellets was recorded by a magnetic suspension balance. The reduction degree (R) of the pellets was determined by Eq. (3.1), where M_0, M_f, and, M_t are the initial mass, the instantaneous mass, and the theoretical mass after the complete reduction of the hematite pellet, respectively [97].

$$R = \frac{M_0 - M_f}{M_0 - M_t} \times 100\% \quad (3.1)$$

Table 1. The list of samples and their reduction conditions.

Reduction condition	Sample designation	Temperature (°C)	Gas pressure (bar)	Reduction time (min)	Gas flow (mL_s/min)
Static gas (interrupted tests)	S1bar5min	700	1	5	-
	S1bar30min		1	30	-
	S1bar120min		1	120	-
	S10bar5min		10	5	-
	S10bar30min		10	30	-
	S10bar120min		10	120	-
	S100bar5min		100	5	-
	S100bar30min		100	30	-
	S100bar120min		100	120	-
Dynamic gas (continuous tests)	D1bar	700	1.3	120	200
	D50bar		50	120	500

3.2.2. Microstructural characterization

The reduced pellets were sliced into disk-shaped samples from the middle of the pellets with a thickness of ~1 mm using a diamond wire saw. Subsequently, the samples were grinded using SiC papers from 320 to 4000 grits and followed by polishing using diamond suspension with a particle size of 3 µm and 1 µm and final polishing with colloidal silica suspension (OPS). The microstructure of the samples was then characterized using secondary electron (SE) and backscattered electron (BSE) imaging modes in a Zeiss Merlin scanning electron microscope

(SEM). In addition, electron backscatter diffraction (EBSD) was employed to characterize the local distribution of the phases. The step size of the EBSD measurement was 50 nm and the EBSD data were analyzed using the software OIM Analysis^{TM} V9. The porosity analysis was performed on 12 SE images (500× magnification, corresponding to 38590 μm^2 imaging area) using the software ImageJ. The inherited pores from the pelletizing process were identified to be >95 μm^2 in the unreduced hematite pellet. To reveal the fraction and size of the acquired pores in reduced pellet, pores with a size below 95 μm^2 were further analyzed.

To identify the phases in the samples, X-ray diffraction (XRD) analysis was employed using a Rikaku SmartLab diffractometer equipped with Cu-K_α radiation (λ = 1.5406 Å). The beam size was set to be 0.5×0.5 mm^2. To reveal also the spatial distribution of the individual phases in the pellet samples [91], XRD measurements were performed from the pellet surface to the center with a step size of 1 mm, as shown in **Fig. 13**a. The Rietveld refinement method was used to quantify the individual phases in conjunction with the Material Analysis Using Diffraction (MAUD) software, **Fig. 13**b [98].

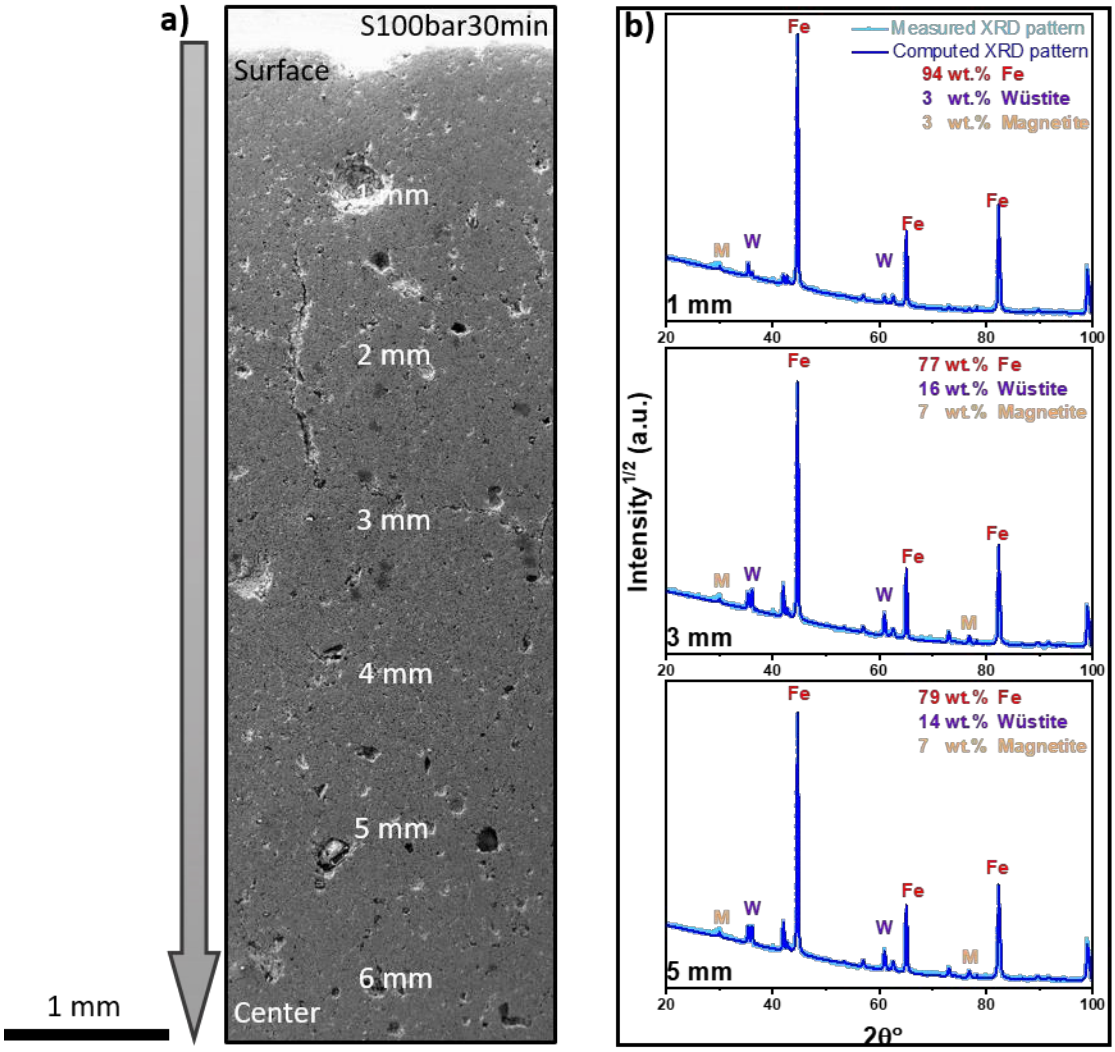

Fig. 13. Demonstration of the phase distribution in the sample S100bar30min. a) Secondary electron image of the sample from surface to the center. b) X-ray diffraction profiles from a distance of 1, 3, and 5 mm below the pellet surface. All experiments were conducted at 700°C. (M stands for magnetite, W for wüstite, and α-Fe for bcc-iron.). The values of error bars in phase analysis are smaller than 0.6 wt%.

3.3. Results

3.3.1. Influence of H_2 pressure on reduction kinetics under static condition

The spatial distribution of the magnetite, wüstite, and α-iron along the pellet diameter was probed using XRD, as shown in **Fig. 14**. After 5 min of reduction, the hematite completely transformed into magnetite in all the pellets reduced at different H_2 pressures. At the macroscopic scale, pellets exhibited the typical topochemical characteristics of reduced pellets in the solid state, as clearly revealed by the spatial gradient of individual phases along the pellet diameter. Here, the term

'topochemical characteristics' refers to the spatial gradient of high and low oxidation states of iron, for instance, an increasing trend in the quantity of the high oxidation state of iron from the pellet surface to the center since the reaction starts at the pellet surface and proceed through the pellet interior [91].

The comparison of the distribution of phases in the pellets reduced at different pressures for the same duration indicated that an increase in the H_2 pressure resulted in faster reduction kinetics. For example, the pellet reduced at 1 bar for 5 min (S1bar5min) showed ~70 wt.% magnetite and ~30 wt.% wüstite on average in the pellet (**Fig. 14**a), whereas an increase in H_2 pressure to 10 bar resulted in 48 wt% magnetite, 51 wt% wüstite, and a subtle amount of α-iron (1 wt%) in the pellet reduced for 5 min (**Fig. 14**d). When the H_2 pressure was further increased to 100 bar, a higher fraction of α-iron was found in the surface region (~15 wt%) (**Fig. 14**g). Such differences strongly suggested an enhancement of the reduction kinetics when increasing the H_2 pressure in the static gas condition. The same trend was also observed with prolonged reduction time. After 120 min, less than 10 wt% α-iron was found in the pellet reduced at 1 bar (**Fig. 14**c). In contrast, more than 98 wt% α-iron was observed at 100 bar (**Fig. 14**i), suggesting an almost completed reduction in the latter case.

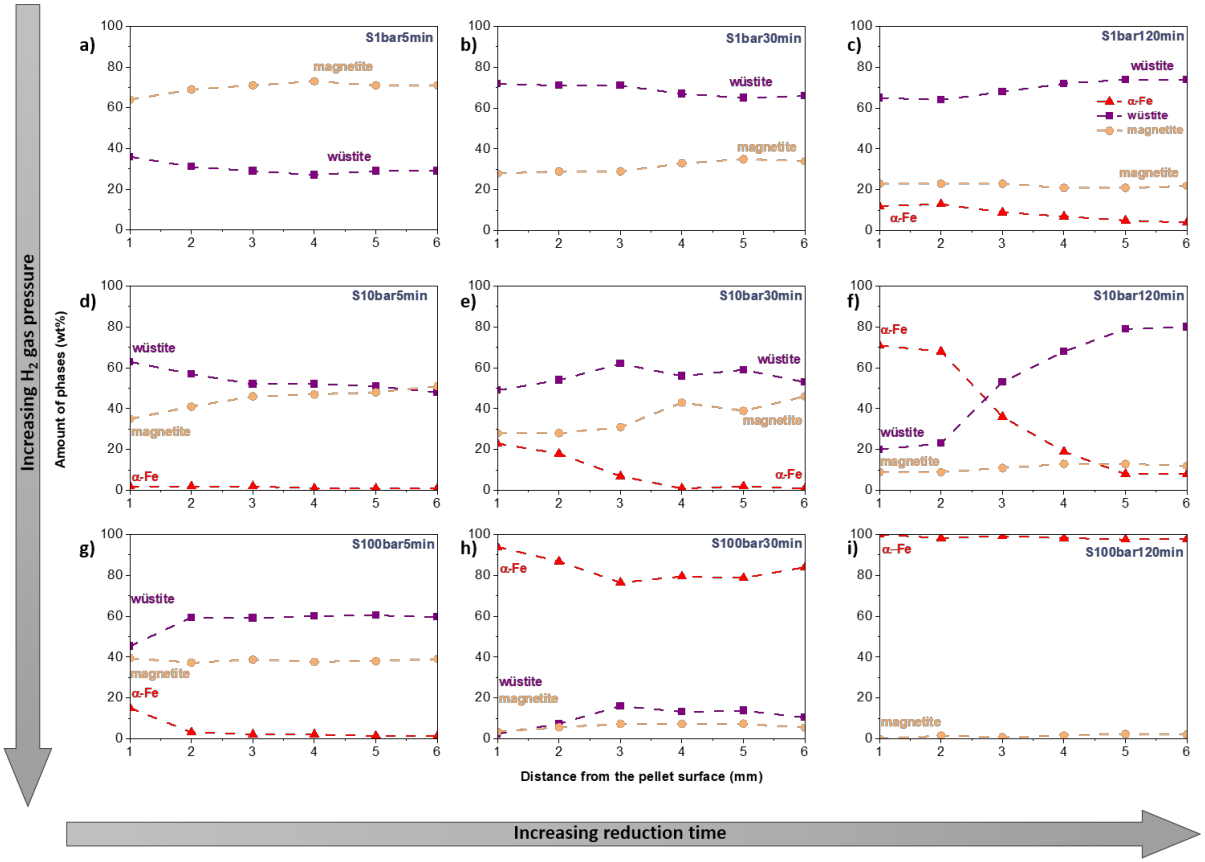

Fig. 14. Spatial distribution of individual phases as a function of pellet diameter from the surface to the center for the pellet reduced under the static gas condition **a-c)** at 1 bar, **d-f** at 10 bar, and **g-i)** at 100 bar; **a**, **d**, **g)** for 5 min, **b**, **e**, **h)** for 30 min, and **c**, **f**, **i** for 120 min. The amount of phase was probed using X-ray diffraction (XRD) with a beam size of 0.5 mm × 0.5 mm. All experiments were conducted at 700 °C.

3.3.2. Influence of H_2 pressure on microstructure formation under static gas exposure condition

Fig. 15 reveals the evolution of the pore morphology of pellets reduced at 700°C for 5 min at 1, 10, and 100 bar H_2 pressures, respectively. The regions marked by dark orange and yellow arrows are iron oxides (here a mixture of magnetite and wüstite) and pores, respectively. All pellets had a large amount of inherited (~30%) pores distributed among dense hematite grains, see **Fig. 15**a, as well as the acquired pores. The former were generated during pelletization (high-temperature sintering of the ore fines), while the latter formed and evolved during reduction, due to the gradual removal of oxygen and the formation of cracks [6, 99]. The formation of the pores and their connectivity are critical for the overall reduction kinetics as they provide fresh oxide surfaces for chemical reactions and pathways for the outbound gaseous diffusion of the redox product gases H_2O and CO_2, respectively [76]. For the pellet reduced at 1 bar for 5 min (S1bar5min), elongated

pores were observed within the iron oxide grains (here a mixture of magnetite and wüstite), as shown in **Fig. 15**b. In contrast, the sample reduced at elevated pressure values of 10 bar (**Fig. 15**c) and 100 bar (**Fig. 15**d), respectively, for 5 min revealed circular pores instead of the elongated morphology.

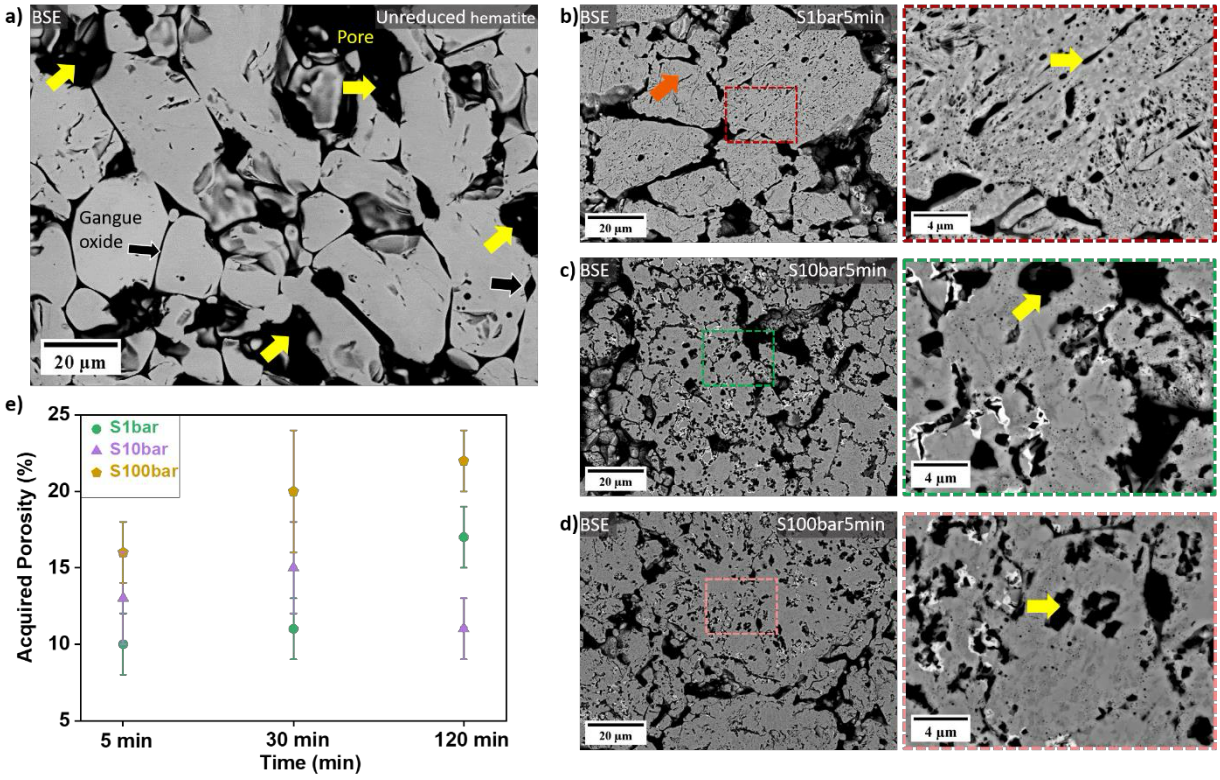

Fig. 15. The backscattered electron image of **a)** unreduced pellet and pellets reduced for 5 min at **b)** 1 bar, **c)** 10 bar, **d)** 100 bar, and **e)** evolution of acquired porosity as a function of reduction time at various H_2 pressures (Analysis based on secondary electron images taken from the region about 2 mm below the pellet surface). All experiments were conducted at 700 °C.

The evolution of the acquired porosity of pellets reduced under static gas conditions is shown in **Fig. 15**e. Pellets reduced at 1 bar and 100 bar exhibited a similar trend. The acquired porosity of these two pellets increased progressively to 17% (1 bar) and 22% (100 bar) with further removal of oxygen over time. Pellets reduced at 100 bar possessed a higher porosity since the reduction degree was higher (*e.g.*, 98% for 120 min) than that of pellets reduced at 1 bar (73% for 120 min). The evolution trend of the acquired porosity in pellets reduced at 10 bar differed from those reduced at 1 and 100 bar. It was observed that the porosity was 13% in the pellet reduced at 10 bar for 5 min, and it slightly increased to 15% after HyDR for 30 min, followed by a decrease to 11% in the pellet reduced for 120 min. Such a decrease might be due to the coalescence of the acquired

pores and growth into pores with a size larger than 95 μm^2 to minimize the total interfacial energy [66], *i.e.* this would be a statistical effect in data analysis.

In addition to the change in the morphology of the pores, the morphology of the α-iron also evolved differently at elevated pressure. **Fig. 16** demonstrates the α-iron formed in the S1bar120min (**Fig. 16**a), S10bar30min (**Fig. 16**b), and S100bar5min (**Fig. 16**c) samples. These particular materials were selected due to their comparable α-iron fractions close to the pellet surface (~15% at S1bar120min, ~20% at S10bar30min, and ~18% at S100bar5min). The formation of α-iron was primarily found in the proximity of pores. In the sample reduced at 1 bar for 120 min, dense iron layers formed and encapsulated the unreduced iron oxides (**Fig. 16**a). A similar morphology and distribution behavior of α-iron was also observed in the sample reduced at 10 bar (**Fig. 16**b). In contrast, α-iron revealed a porous structure at 100 bar of H_2 pressure (**Fig. 16**c).

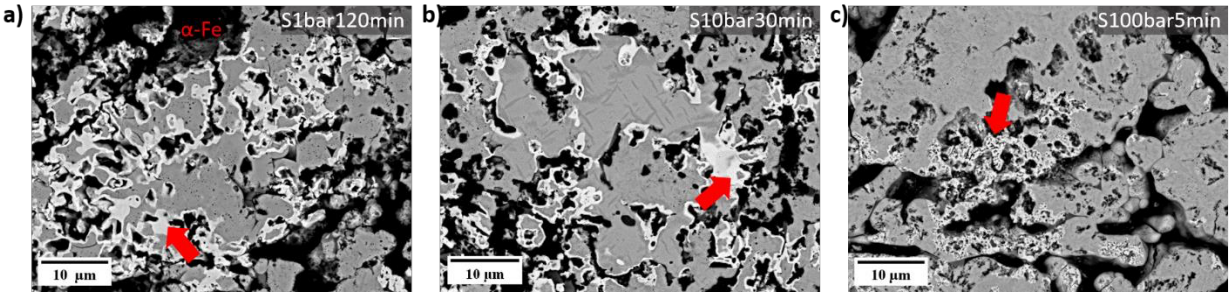

Fig. 16. The morphology changes of metallic iron as a function of various H_2 pressures in **a)** S1bar120min, **b)** S10bar30min, and **c)** S100bar5min samples. All experiments were conducted at 700 °C.

The morphology of α-iron under 100 bar H_2 pressure evolved with reduction time, **Fig. 17**. After HyDR for 5 min, porous iron with 1.0±0.1 µm grain size formed on the iron oxide surface. The S100bar5min sample revealed a homogeneous distribution of magnetite (52 area%) and wüstite (43 area %), deviating from the topochemical pattern (**Fig. 17**b). As reduction proceeded for 30 min, the iron oxide (22 area % wüstite, 8 area % magnetite) was encapsulated by ultrafine iron grains (0.5±0.2 µm), **Fig. 17**c. It is worth noting the presence of magnetite layers between wüstite and α-iron (**Fig. 17**d) in the S100bar30min pellet. This phenomenon might result from the phase decomposition of wüstite into iron and magnetite during cooling since wüstite is not thermodynamically stable below 570 °C. As the HyDR proceeded, the ultrafine iron grains coarsened to 2.3±0.2 µm, as depicted in **Fig. 17**e-f.

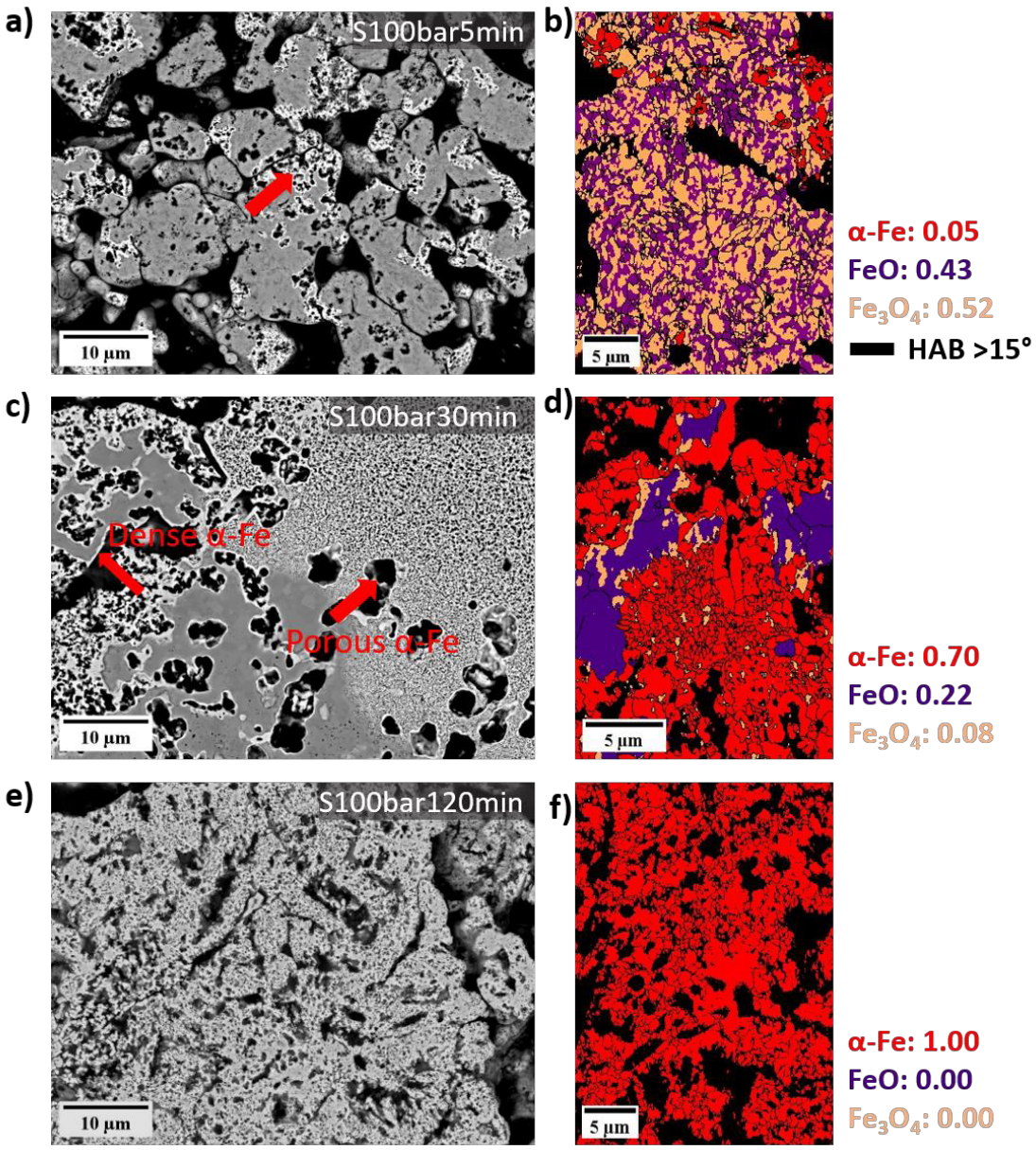

Fig. 17. The backscattered electron (BSE) image and phase map and phase fractions (area%) probed by electron backscatter diffraction (EBSD) of **a-b)** S100bar5min, **c-d)** S100bar30min, **e-f)** S100bar120min pellet. All experiments were done at 700°C. HAB stands for high-angle grain boundary.

In summary, the H_2 partial pressure affected the microstructure of hematite pellets in two aspects under static gas exposure conditions: (1) the acquired pores as a result of the reduction showed elongated morphology at low H_2 pressure (1 bar), while circular pores were observed at elevated H_2 pressure (10 bar and 100 bar); (2) Porous iron formed at high pressure (100 bar), while dense iron layers were observed at low and moderate H_2 pressure (1 bar and 10 bar).

3.3.3. Influence of H_2 pressure on reduction kinetics under dynamic gas exposure conditions

Fig. 18 presents the reduction kinetics of pellets reduced at 1.3 and 50 bar H_2 gas pressure under dynamic gas exposure conditions. As an example, the instantaneous mass loss of the pellet reduced at 50 bar (D50bar) is demonstrated in **Fig. 18**a. After purging H_2 for approximately 1.5 min, the onset of mass loss was observed. The mass loss reached a steady state at ~650 mg after ~50 min at 700°C, suggesting completion of reduction. **Fig. 18**b represents the reduction degree of pellets as a function of time. At the initial stage of reduction, pellets exhibited an incubation period for 3 and 1 min at H_2 pressure of 1.3 and 50 bar, respectively. The apparent incubation period may stem from the time needed for gas exchange within the reaction chamber, *i.e.,* from Ar to H_2. The reduction degree of D1bar and D50bar pellets reached ~0.95 after 49 and 33 minutes, respectively. In addition, the plots of reduction rate (dR/dt, **Fig. 18**c) revealed a higher reduction rate in the pellet reduced at 50 bar compared with that reduced at 1 bar. In both cases, the reduction rate decreased gradually in the stage when wüstite started to transform into α-iron. Such a decrease was supposed to be due to the limited removal kinetics of oxygen through the dense iron layers, encapsulating the remaining wüstite [6, 91].

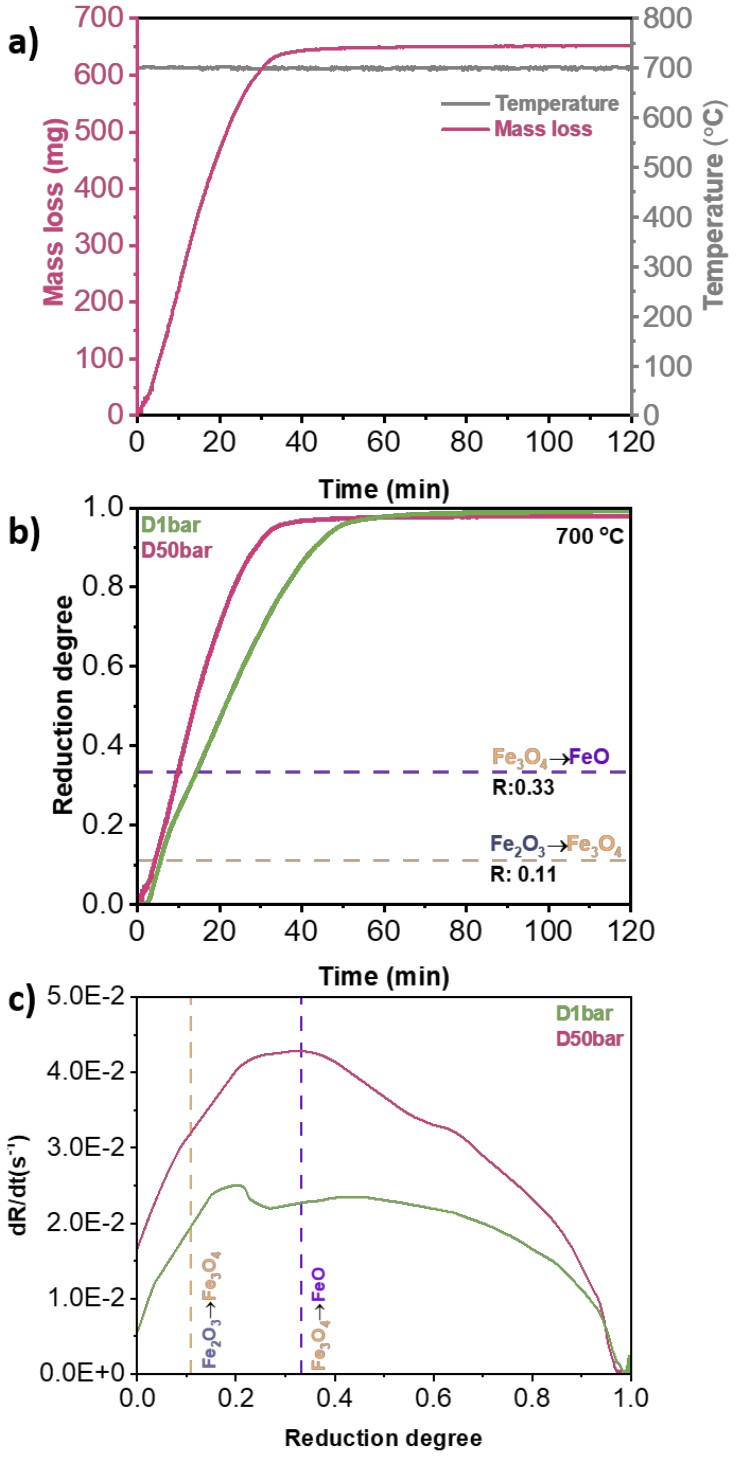

Fig. 18. The reduction kinetics of hematite pellets reduced at 700 °C in pure H_2 at different pressures under the dynamic gas condition **a)** Instantaneous mass loss of the pellet reduced at 50 bar, measured by thermogravimetry analysis **b)** Reduction degree (R) of the pellets reduced at different H_2 pressure values. Yellow and purple dash lines mark the theoretically expected reduction degree from hematite to magnetite (R = 0.11) and from magnetite to wüstite (R = 0.33), respectively. **c)** Plots of reduction rate (dR/dt) versus reduction degree (R). All data acquired from reduction experiments at 700°C.

3.3.4. Microstructure evolution under the dynamic gas condition

Fig. 19 shows the microstructure of the reduced pellets at 1.3 and 50 bar H_2 gas pressure at 700 °C for 120 min under the dynamic gas condition. The pore morphology in the reduced pellets changed from an elongated shape at ambient pressure (**Fig. 19**a) to a more circular one at 50 bar (**Fig. 19**b), similar to the morphology observed under static gas exposure. This finding was further quantitatively supported by a decrease in the aspect ratios of acquired pores from 1.83 (at 1.3 bar) to 1.64 (at 50 bar) with an increase in H_2 pressure. The pellets reduced at 1.3 bar and 50 bar showed similar porosity values, *i.e.*, 21.0±4.0% at 1.3 bar and 19.0±5.0% at 50 bar. In addition, the grain size of the reduced iron was significantly finer, *i.e.*, dropping in average size from 9.0±1.0 µm (at 1.3 bar) to 1.0±0.8 µm (at 50 bar) when treated under an increased H_2 gas pressure.

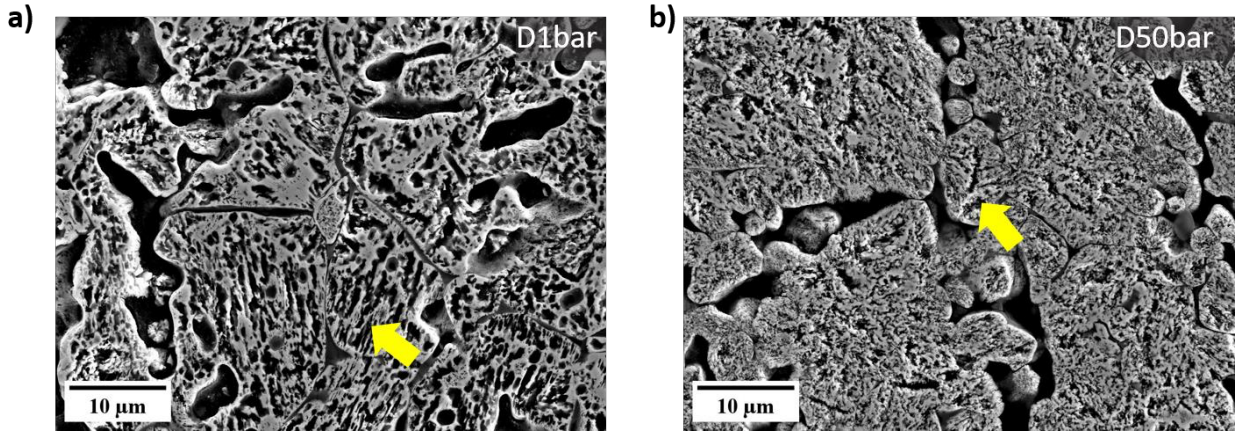

Fig. 19. Secondary electron (SE) images of the sample reduced at **a)** 1.3 bar, and **b)** 50 bar under the dynamic gas condition. Yellow arrows indicate pores. Experiments were done at 700°C.

3.4. Discussion

3.4.1. Influence of H_2 pressure on reduction kinetics

Table 2 shows the average fractions of the individual phases in the spherical pellets. The spatial distribution curves for magnetite, wüstite, and α-iron along the pellet radius (**Fig. 13**) were fitted individually using polynomial functions available in the OriginPro 2022 software. Subsequently, the polynomial equations were integrated for the spherical volume to calculate the phase fractions in the spherical pellets.

Table 2. The quantity of α-iron, wüstite, and magnetite in the pellets reduced under the static gas reduction conditions at 700°*C*.

Sample	Metallic iron (wt.%)	Wüstite (wt.%)	Magnetite (wt.%)
S1bar5min	-	29	71
S1bar30min	-	67	33
S1bar120min	6	71	23
S10bar5min	1	51	48
S10bar30min	7	64	29
S10bar120min	18	70	12
S100bar5min	1	38	61
S100bar30min	80	12	8
S100bar120min	99	-	1

During HyDR, the reaction occurs in several steps: (1) Transport of H_2 molecules to the reaction front (*e.g.,* pellet and surface of open pores); (2) Dissociation of H_2 into H atoms on the iron oxide and metallic iron surfaces [37, 38]; (3) Adsorption of H atoms; (4) Oxygen removal via H reaction with the oxygen in the iron oxides, *i.e.,* formation of H_2O, iron cations, and anion vacancies; (5) Desorption of H_2O from the reaction surface; (6) Diffusion of H_2O and transport with the gas stream.

Next, the influence of H_2 pressure on these individual steps will be discussed for reduction kinetics under static gas exposure conditions. During the early stage of HyDR, the kinetics is controlled by a mixture of mass transfer of gas molecules to the reaction front and the chemical reaction [47]. At high pressure, the collision frequency of H_2 molecules with the iron oxide surface increases [100]. In this study, thus, the reduction kinetics at the initial stage was supposed to be most pronounced at 100 bar. Regarding steps (2) and (3), Li et al. [101] investigated the dissociation and adsorption behavior of H_2 on hematite and iron at various pressure levels (1 to 1000 bar) and temperatures (from room temperature up to 627 °C) by applying a combination of density functional theory calculations and statistical thermodynamics. They suggested that high pressure facilitates the dissociation and adsorption of H_2 molecules. The increase in the quantity of absorbed H_2 molecules on wüstite and hematite with increasing H_2 pressure is also supported by the work of Cheng et al. [102], who arrived at a similar conclusion by using ReaxFF molecular dynamics simulations. Step (4) can be assessed according to Le Chatelier's principle [103], considering that

the overall reaction of HyDR is $Fe_2O_{3(s)}+3H_{2(g)}\rightarrow 2Fe_{(s)}+3H_2O_{(g)}$. Le Chatelier's principle suggests that variations in total pressure should not significantly impact the rate equilibrium of a reaction when the number of moles of the gas molecules in both reactants and products is the same. This in turn means that the rate of the chemical reaction should not be affected by the absolute pressure. Steps (5) and (6) can be assessed considering the counter-current diffusion of H_2 (inward) and H_2O (outward) molecules through the reaction front (pore or pellet surface). Assuming that the same amount of hematite was reduced into iron at different H_2 pressures, the amount of the produced H_2O should be the same. Since the amount of H_2 molecules in a confined volume is higher at 10 and 100 bar (*i.e.,* ×10 for 10 bar, and ×100 for 100 bar) than that at 1 bar, the partial pressure of H_2 ($P_{H_2} / (P_{H_2} + P_{H_2O})$) will be highest at 100 bar, followed by 10 bar and finally 1 bar. This condition results in a faster outward flux of H_2O at 100 bar than at 10 and 1 bar due to the higher concentration gradient of H_2 and H_2O between the reaction surface and the gas stream.

Also, the change in partial pressure of H_2 has a substantial effect on the thermodynamics of the reaction. The Gibbs energy of a solid-gas reaction can be expressed along Eq. 3.2;

$$\Delta G = \Delta G^0 + RT \ln Q \tag{3.2}$$

wherein ΔG^0 is the standard Gibbs free energy of the reaction and Q is the instantaneous reaction quotient. For the reaction $Fe_2O_{3(s)}+3H_{2(g)}\rightarrow 2Fe_{(s)}+3H_2O_{(g)}$, $Q = \frac{(p_{H_2O})^3}{(p_{H_2})^3}$, ranging from zero (*i.e.,* for pure H_2) to infinity (*i.e.,* for pure H_2O). p_{H_2} and p_{H_2O} are the partial pressure of H_2 and H_2O, respectively. An increase in the value of p_{H_2} thus lowers Q. Hence, the overall thermodynamic driving force of the chemical reaction increases (*i.e.,* decreasing ΔG to a more negative value). In addition, the kinetics of the removal of oxygen increases with increasing H_2 partial pressure [28], as expressed by Eq. 3.3:

$$R_0 = \phi^f P_{H_2}[1 - exp(\Delta G / RT)] \tag{3.3}$$

where, R_o is the rate of oxygen removal from the iron oxide surface and ϕ^f is the apparent chemical reaction constant for the forward reaction ($Fe_2O_{3(s)}+3H_{2(g)}\rightarrow 2Fe_{(s)}+3H_2O_{(g)}$). Since the value of p_{H_2} in the reducing gas is highest at 100 bar, followed by 10 and 1 bar, the rate of oxygen removal follows the same sequence for the rate of reaction at 100, 10, and 1 bar. Consequently,

the enhanced reaction rate at elevated pressures of H_2 gas under static gas conditions is attributed to the increase in the partial pressure of H_2.

Under dynamic gas conditions, the pellet reduced at 50 bar exhibited a higher reduction rate compared with the pellet reduced at 1.3 bar. All the aforementioned aspects, relating pressure to reaction rates, also apply to the dynamic reduction experiments. Similar to the static gas exposure conditions, the partial pressure of H_2 in the reaction chamber is higher at 50 bar compared with 1.3 bar, resulting in an enhancement of the overall reduction kinetics. An additional contribution to the enhanced reduction kinetics at 50 bar H_2 gas pressure may stem from the higher H_2 flow rate at 50 bar (500 mLs/min**)** than at 1.3 bar (200 mLs/min) [104]. Compared with the reduction at 1 and 10 bar under static conditions, the faster reduction kinetics of the reduction conducted at 1.3 bar under dynamic reductant exposure is attributed to the continuous hydrogen supply to the reaction chamber.

3.4.2. Influence of H_2 pressure on the pellets' microstructure formation

In this study, our findings highlighted two major effects of pressure on the microstructure formation and its temporal evolution during HyDR. First, the morphology of the acquired pores changed from an elongated to a more circular shape, as pressure increased from ambient to elevated pressures, as depicted in **Fig. 15** and **Fig. 19**a. Second, the morphology of the iron altered from dense iron layers found at H_2 pressures of 1 and 10 bar to porous iron at 100 bar (**Fig. 16**). Several studies have investigated the correlation between the morphology of iron and the composition of the reducing gas [62, 78-81]. In these studies, it has also been observed that the morphology of metallic iron depends on the partial pressure of the reducing gas (*i.e.,* H_2 or CO). Increasing the partial pressure of H_2 results in the formation of porous iron, while an increase in the partial pressure of H_2O causes denser iron growth, which is associated with the effect of the partial pressure of H_2 on the rate of oxygen removal.

During the reduction of the wüstite to iron, the local concentration of iron increases on the wüstite surface as a result of the removal of oxygen. The increase in local concentration of iron in the surface regions causes a chemical potential gradient between the outer surface and the bulk wüstite inside of the pellet that drives the diffusion of iron towards the bulk wüstite ($Fe_{1-x}O$; $0.83<1-x<0.95$). As reduction proceeds, the concentration of iron ions in the wüstite increases, and

eventually wüstite becomes saturated with iron ions ($Fe_{1-x}O$; (1-x) approaches 0.95). The accumulation of excess iron results in iron clusters and iron nucleation events. Iron nuclei grow with the incoming flux of reduced iron at the iron-wüstite interfaces [62].

The morphology of α-iron (*i.e.*, dense layer or porous iron) is controlled by the competition between the rate of oxygen removal from the surface and the rate of iron diffusion from the wüstite towards the metallic iron phase [60, 105]. **Fig. 20**. schematically shows the formation of the dense iron layer and the porous iron during HyDR. When the diffusion rate of iron is higher than the rate of oxygen removal, excess iron readily diffuses in a direction perpendicular to the wüstite surface. The concentration of excess iron exhibits a homogeneous distribution throughout the wüstite surface. In this case, a planar wüstite surface is maintained. When the iron ions are saturated inside the wüstite, excess iron nucleates homogeneously on the surface and a dense iron layer forms, **Fig. 20**a. When the removal rate of oxygen is faster than the diffusion rate of iron from wüstite to the metallic iron phase, the morphology of the iron alters. The presence of a perturbation (*i.e.,* distortion on the surface at the atomic/molecular level) induces an instability in the form of an alternating sequence of concave and convex features that can protrude into the wüstite, **Fig. 20**b. This instability results in the rejection of iron in the direction parallel to the wüstite surface. Consequently, the concentration of iron on the tip of the perturbation becomes less than that of the planar surface. Due to the lower concentration of iron, the rate of chemical reaction on the tip of such a perturbation feature becomes faster than that of a planar surface. This process continues until the planar surface becomes unstable, resulting in the formation of porous iron [68], **Fig. 20**b. The removal rate of oxygen is determined by the combination of temperature and reducing gas composition, while the diffusion rate of iron is determined only by temperature and by the local chemical potential gradient. As indicated in Eq. 3.3, the removal rate of oxygen at 100 bar is faster compared with 1 and 10 bar, yet the diffusion rate of the iron remains the same. Therefore, the formation of the porous iron at 100 bar H_2 pressure can be attributed to the faster removal of oxygen from the iron oxide compared with the unchanged diffusion rate of the iron, while the formation of the dense iron layer at 1 and 10 bar is attributed to the slower removal rate of oxygen compared with iron diffusion.

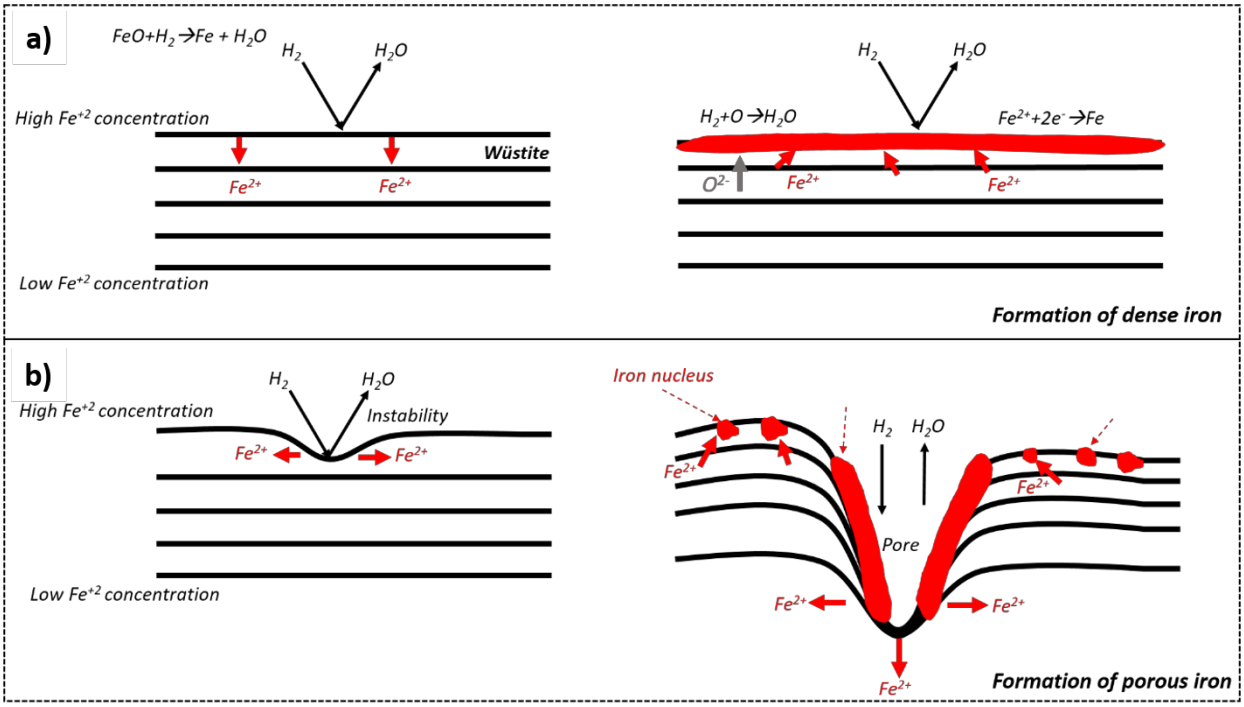

Fig. 20. Schematic illustration of the formation of **a)** dense and **b)** porous α-iron depending on the respective rates of pressure-dependent oxygen removal and iron diffusion [68].

Furthermore, changes in the H_2 pressure causes also a change in pore morphology, from elongated pores at ambient pressure to pores with circular shapes at elevated pressures. The literature suggests two mechanisms that could initiate the formation of porous iron on the wüstite surface: the breakdown (or bursting) of a dense iron layer and the formation of an instability on the oxide surface [62]. The former results from the water production and accumulation at the iron/wüstite interface when hydrogen diffuses through the dense iron layer and reacts with oxygen at the interface. If a void exists at the interface, H_2O or H_2 gas bubbles form and gradually expand the void. Once the gas pressure at the interface becomes larger than the pressure of the reducing gas, the breakdown of the dense iron layer occurs and forms a pore [69]. The latter case is the same as the formation of porous iron due to the faster removal rate of oxygen from the iron surface [68]. The formation of elongated pores at D1bar and S1bar5min samples may stem from the instability formation and its growth during the transition from wüstite to the α-iron phase. At the H_2 pressure of 1 bar, the rate of the reduction at the initial stage (for 5min) can be much faster due to the high initial hydrogen partial pressure and the removal rate of oxygen can suppress the diffusion rate of iron [60].

The grain size of α-iron in fully reduced pellets, namely S100bar120min and D50bar samples, is 2.3±0.2 and 1.0±0.8 μm, respectively. Moreover, the grain size of α-iron decreased from 1.0±0.1 μm (S100bar5min) to 0.5±0.1 μm (S100bar30min) at 100 bar H_2 pressure under the static gas conditions. Such ultrafine grain size of α-iron indicates a high density of iron nucleation events on the wüstite surface during HyDR when exposed to high H_2 pressure conditions. In this case, α-iron is likely to grow by transporting iron from the saturated wüstite adjacent to these nuclei. This scenario suggests that the morphology of the pores is dominated by the nucleation of iron. Consequently, small radii and a large number of pores form around the fine iron grains.

3.5. Conclusion

In this study, we studied the hydrogen-based direct reduction of commercial polycrystalline hematite pellets at elevated H_2 pressure under both static (1, 10, and 100 bar) and dynamic (1.3 and 50 bar) gas exposure conditions at 700 °C, to understand the effects of H_2 pressure on the reduction kinetics and microstructure formation. The main conclusions are summarized as follows:

(1) The hematite pellets exhibited increasing reduction kinetics with an increase in H_2 pressure under both static gas exposure conditions (1, 10, and 100 bar) and dynamic gas exposure conditions (1.3 and 50 bar).

(2) Under both static and dynamic reduction conditions, the morphology of the pores in the reduced pellets changed from an elongated structure at ambient pressure to a circular structure at an elevated H_2 pressure. The elongated pores form due to an instability formation and its growth during the reduction of wüstite to α-iron when the diffusion rate of iron is slower than the removal rate of oxygen. At elevated pressure, a high number density of iron nucleation results in the formation of a large number of pores with small radii.

(3) The reduction of iron ore at a hydrogen gas pressure of 100 bar represents an extreme scenario regarding the current direct reduction furnace operations at the industrial scale. Nonetheless, our observations have unveiled reduction kinetics and microstructure formation (*i.e.,* ultra-fine grains) in the direct reduced iron under such extreme conditions. This study could also inspire applications related to the hydrogen-based redox

reactions of iron oxides at high pressure, such as for catalytical applications, as well as the fabrication of ultrafine microstructure via hydrogen-based direct reduction.

(4) Pellets reduced at an H_2 pressure of 1 and 10 bar, respectively, exhibited dense iron formation on wüstite as a consequence of the low partial pressure of H_2 and the slow reduction kinetics. The slower oxygen removal compared with the diffusion rate of iron resulted in the formation of a dense iron layer. In contrast, elevated H_2 pressure resulted in fast oxygen removal compared to the unchanged iron diffusion from the reaction interface towards the iron nuclei favors the formation of porous iron structures.

(5) The H_2 pressure plays an important role in the reduction kinetics and microstructure formation during hydrogen-based direct reduction of iron oxides. An increasing H_2 pressure increases the partial pressure of H_2, which promotes faster reduction kinetics. This fact should be considered for the design of industrial reactors.

4. GREEN IRONMAKING UNDER HIGH H2 PRESSURE: RESOLVING INDIVIDUAL REACTION STEPS VIA *IN-SITU* SYNCHROTRON HIGH-ENERGY DIFFRACTION

This chapter is based on the publication: Özge Özgün, Gökhan Gizer, David Melching, Kartik Umate, Eric Woods, Laurine Choisez, Guillermo Requena, Claudio Pistidda, Dierk Raabe, Yan Ma (2025). Green ironmaking under high H_2 pressure: resolving individual reaction steps via in-situ synchrotron high-energy diffraction. *Submitted to Acta Materialia.*

Hydrogen-based direct reduction (HyDR) of iron ore presents a promising route for green ironmaking without CO_2 emission, offering a sustainable solution to decarburizing steel production. HyDR proceeds via a solid-gas reaction involving multiple reduction steps from hematite to magnetite, wüstite, and metallic iron. While the overall reduction kinetics and microstructural evolution are known to be influenced by H_2 gas pressure, its effect on the individual reaction steps remains unclear. Here, we employed in-situ synchrotron high-energy X-ray diffraction to monitor real-time phase transformations during the HyDR of hematite at 700 °C under varying H_2 pressures ranging from 1 bar to 100 bar. Microstructure of the reduced samples was characterized using scanning electron microscopy equipped with electron backscatter diffraction, and the three-dimensional pore morphology was analyzed using X-ray nano-computed tomography. Our results show that elevated H_2 pressures accelerated reduction kinetics across all steps and lowered the onset temperatures of phase transformations. The reduction of wüstite to iron remained the rate-limiting step, governed by a localized phase-boundary-controlled mechanism. Increasing H_2 pressure enhanced the thermodynamic driving force and kinetics of this step by accelerating the interface movement. Moreover, pore morphology transitioned from elongated to equiaxed shapes with increasing pressure, indicating a shift in the balance between vacancy diffusion and interface mobility. The results offer valuable insights into the pivotal role of H_2 gas pressures in HyDR, paving the way for improving the reduction efficiency of corresponding reactor operations.

4.1. Introduction

Global steel production has averaged approximately 1800 million tons annually over the past decade. Around 70% of steel is produced via the integrated blast furnace-basic oxygen furnace (BF-BOF) route [106], using carbon as both a reducing agent and an energy source. Consequently, the iron and steel industry is highly carbon-intensive, accounting for 8-10% of global CO_2 emissions [1]. Growing pressure to reduce these emissions has driven the shift toward fossil-carbon-free ironmaking processes. In this context, hydrogen-based metallurgical processes offer a potentially sustainable route to decarbonize this industrial sector, as the reaction of hydrogen with iron oxides yields only water as a by-product [1, 3, 82, 107], provided that H_2 is generated using renewable energy sources. Among emerging green steel production technologies, hydrogen-based direct reduction (HyDR) is currently the most advanced and scalable one, with a technology readiness level of 6-8 [3].

HyDR involves a solid-gas reaction, in which hydrogen atoms interact with chemically bonded oxygen in the iron oxide lattice and reduce it to metallic iron at temperatures between 500-1100 °C [6, 30, 35]. The reaction proceeds in multiple steps, in which hematite (Fe_2O_3) is gradually reduced to magnetite (Fe_3O_4), wüstite ($Fe_{1-x}O$; $0.05 \leq x \leq 0.17$), and metallic iron (Fe) above 570 ºC. Below this temperature, the reduction proceeds directly from magnetite to metallic iron, as wüstite is thermodynamically unstable under these conditions. The kinetics of HyDR can be governed by several processes, including (1) the inward diffusion of H_2 molecules to the reaction front and the outward diffusion of H_2O molecules to the gas stream [47], (2) the rate of the chemical reaction at the reaction interface, (3) the nucleation and growth of the product phases [108, 109], and (4) the mobility of advancing phase boundaries within the solid (*e.g.,* oxide/oxide or metal/oxide interfaces) [110, 111]. Among these steps, the slowest one determines the overall kinetics and is referred to as the rate-controlling mechanism.

Key parameters, such as temperature, gas flow rate [104], gas pressure [112], and microstructure evolution of iron oxide [30, 62, 78], play a crucial role in determining the rate-controlling mechanisms of HyDR [46]. For instance, at elevated temperatures, the chemical reaction rate increases to the point where it no longer limits the overall reduction. Instead, mass transport, namely, the inward diffusion of H_2 and the outward diffusion of H_2O, can become the rate-controlling factor. Moreover, insufficient H_2 flow rate and low gas pressure may restrict the supply

of reducing gas to the reaction front, making mass transport the rate-controlling mechanism [53, 104]. In contrast, high flow rates and elevated H_2 pressure facilitate mass transport and increase the local concentration of H_2, shifting the rate control to the chemical reaction at the reaction front (*e.g.,* gas/oxide or metal/oxide interface) [38, 101, 102, 113]. Thus, variations in H_2 gas pressure can significantly affect the rate-controlling step in HyDR.

The effect of reducing gas pressure on reduction kinetics has been investigated for both pure gas atmospheres (*e.g.*, H_2 and CO) [51-53, 112] and mixed gas systems (*e.g.*, mixing of H_2, H_2O, CO, CO_2, or CH_4) [54, 55]. A consistent trend reported in the literature indicates that increasing H_2 pressure enhances the overall reduction kinetics. This is primarily attributed to the increase in H_2 partial pressure (P_{H_2}), which promotes faster oxygen removal from the iron oxide lattice [28, 53]. Among the sequential reaction steps in HyDR, the reduction of wüstite to metallic iron is identified as the most kinetically limiting one. Despite its significance, the effect of H_2 pressure on the kinetics and underlying mechanism of this final transformation step remains poorly understood due to the overlap of several reactions in the overall kinetic measurements usually via thermogravimetry analysis. Thus, real-time monitoring of the evolution of individual phases during reduction under varying H_2 pressures is essential to gain deeper insights into the governing mechanisms and close this critical knowledge gap.

In this study, we performed *in-situ* high-energy X-ray diffraction (HEXRD) measurements during the HyDR of hematite to investigate the effect of H_2 gas pressure on the kinetics of individual reaction steps. Experiments were conducted at pressures of 1, 10, 50, and 100 bar. In addition, the influence of H_2 gas pressure on pore morphology of the reduced iron was analyzed for the samples reduced at 1 bar and 100 bar using X-ray nano-computed tomography (Nano-CT) to highlight the impact of H_2 gas pressure on the microstructure of the final product. Through real-time monitoring of phase transformations, our findings provide critical insights into how H_2 gas pressure influences the reduction kinetics and underlying reaction mechanisms of HyDR.

4.2. Materials and methods

4.2.1. Materials

A commercial direct-reduction hematite pellet was used in this study, which contains 0.36 wt.% FeO, 1.06 wt.% SiO_2, 0.40 wt.% Al_2O_3, 0.73 wt.% CaO, 0.57 wt.% MgO, 0.19 wt.% TiO_2, 0.23

wt.% V, 0.10 wt.% Mn, with traces of P, S, Na, and K, and Fe_2O_3 in balance. Rectangular cuboid samples with dimensions of ~0.5 mm × 0.5 mm ×5 mm were cut from the hematite pellet using a diamond wire saw.

4.2.2. In-situ synchrotron high-energy X-ray diffraction

In-situ synchrotron HEXRD was employed to monitor the real-time reduction kinetics and to resolve the phase transformation behavior of individual reduction steps during HyDR of hematite at various H_2 gas pressures of 1, 10, 50, and 100 bar. The HEXRD experiments were performed in transmission mode at the Powder Diffraction and Total Scattering Beamline P02.1 of PETRA III at DESY [114]. The beamline operated at a fixed beam energy of 60 keV, corresponding to a wavelength of ~0.207 Å. The spot size of the X-ray beam was set to 0.5 mm × 0.5 mm. A rectangular cuboid hematite sample was placed in an *in-situ* reaction cell with a single-crystal sapphire capillary (inner diameter: 0.6 mm; length: 80 mm) [115], **Fig. 21**a. The reaction cell was filled with high-purity H_2 gas (99.999%) at a designated pressure. The sample was heated from room temperature to 700 °C using a hot air blower (**Fig. 21**a), at an average heating rate of 1.4±0.3 °C/s, **Table 3**., The holding time at 700 °C in all the experiments was limited to ~1800 s, due to the beamtime constraints. Then, the experiments were stopped and the samples were cooled to room temperature by switching off the hot air blower. Temperature at the sample position was calibrated using a type K thermocouple. The heating profile for each experiment was fitted with a linear model using OriginPro 2022 to determine the average heating rate. It is worth noting that all experiments were conducted under static gas conditions. The HyDR parameters are summarized in **Table 3** for each sample.

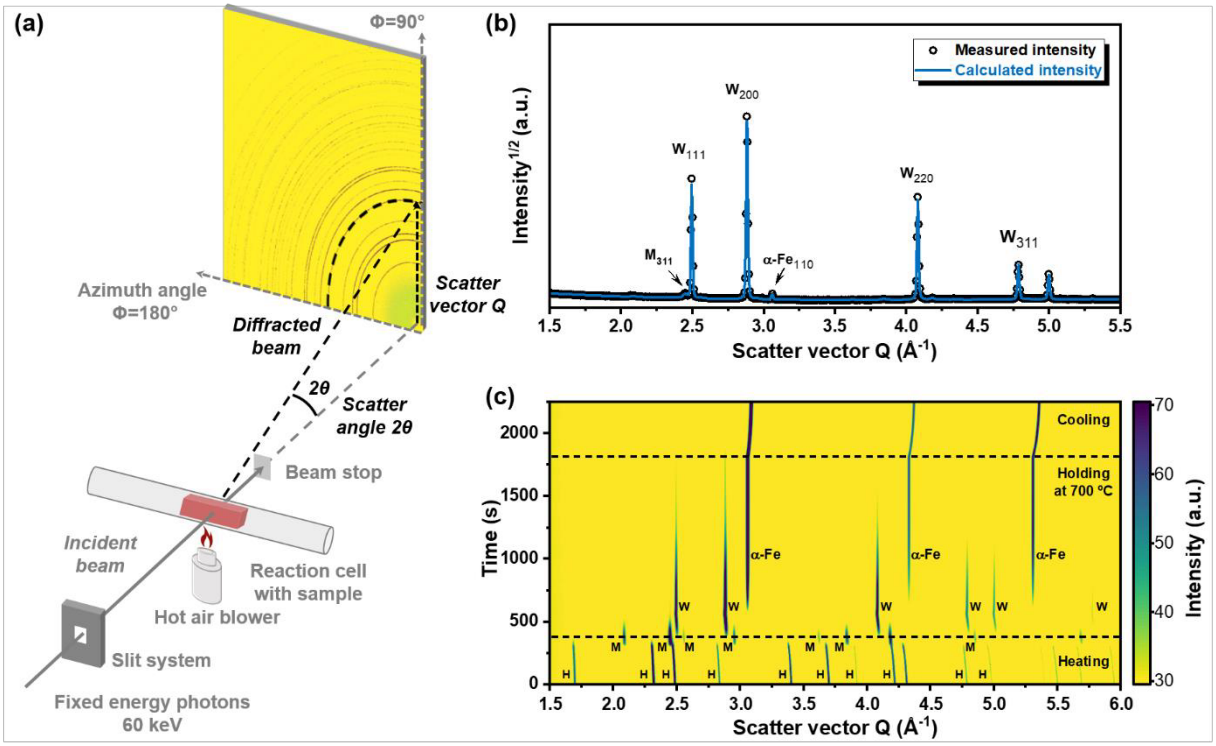

Fig. 21 In-situ synchrotron high-energy X-ray diffraction during reduction of hematite samples: **a)** Schematic illustration of the experimental setup with the reaction cell. **b)** An example of an integrated diffraction profile (open dots) over an azimuth angle of 90° and the corresponding calculated profile (solid curve) of the sample reduced at 1 bar H_2 for 580 seconds (at the temperature of 700 °C). **c)** Contour map of the integrated intensity of hematite sample at 1 bar H_2 gas pressure as a function of reduction time, H stands for hematite, M for magnetite, W for wüstite, and α-Fe for bcc-iron.

Table 3 Sample designation and reduction parameters for in-situ synchrotron high-energy X-ray diffraction experiments

Sample designation	H_2 pressure (bar)	Average heating rate (°C/s)	Holding time at 700 °C (s)	Reduction degree at the end of the experiments (-)
P1	1	1.7	1420	0.96
P10	10	1.1	1770	0.95
P50	50	1.3	1460	1.00
P100	100	1.1	320	1.00

During the HEXRD experiments, diffraction patterns were recorded every two seconds using a fast area detector Varex XRpad 4343CT (2880 pixels × 2880 pixels with a pixel size of 150 µm × 150 µm) with a quarter-ring configuration. The sample-to-detector distance was set to ~1700 mm,

which was calibrated using the NIST standard LaB_6 powder. The two-dimensional diffraction patterns were integrated over an azimuth angle of 90° (from 90° to 180°, as shown in **Fig. 21**a) into diffraction profiles using the software General Structure Analysis System (GSAS II) [116], as exemplarily shown in **Fig. 21**b (open dots). The two-dimensional contour plot as a function of time illustrates the progression of hematite reduction to iron, highlighting the phase evolution during HyDR at the H_2 pressure of 1 bar, **Fig. 21**c. The Rietveld refinement method was used to quantify the fraction of individual phases with the aid of the Material Analysis Using Diffraction (MAUD) software package [98], **Fig. 21**b (solid curve). The goodness of the refinement was indicated by the weighted profile R-factor, which was below 8% for all the analyses.

The conversion degree of wüstite reduction into α-iron reaction is calculated by accounting the weight fractions of relevant phases, derived from *in-situ* HEXRD measurements. The conversion degree of wüstite into metallic iron, α-Fe, ($X_{\text{Wüs}\rightarrow\alpha-\text{iron}}$) was determined by the ratio of transformed phase (*i.e.,* α-iron) to the total amount of the initial phase (*i.e.,* wüstite), using Eq. (4.1);

$$\text{From wüstite to α-iron : } X_{\text{Wüs}\rightarrow\alpha-\text{iron}} = \frac{w_{Fe}}{w_{Fe}+w_{FeO}} \tag{4.1}$$

where, w_{FeO} and w_{Fe} represent the amount of wüstite, and α-iron measured by HEXRD, respectively.

To provide a quantitative measure of the reduction progress, the overall reduction degree of each sample was calculated using the phase compositions of hematite, magnetite, wüstite, and α-iron (in wt.%) obtained from *in-situ* HEXRD measurements. These weight fractions were converted to moles of each phase, and the corresponding moles of iron were determined based on the known stoichiometry of each phase. Assuming no iron loss during reduction, the total moles of iron initially present (calculated from the initial mass of pure hematite) were equated to the sum of iron moles in all reduced phases. Using this iron balance, the overall reduction degree was calculated as the ratio of the actual mass loss (due to oxygen removal) to the theoretical maximum mass loss expected if complete reduction to α-iron had occurred (See Appendix 8.2.1).

4.2.3. Microstructure characterization

The reduced samples were embedded in a PolyFast resin to enable surface preparation for metallographic investigations. Embedded samples were ground using SiC papers from 1000 grits

to 4000 grits, followed by polishing with 3-µm and 1-µm diamond suspensions. The sample preparation was completed with a polishing step using colloidal particle suspension (OPS). The microstructure of samples was characterized using a Zeiss Merlin scanning electron microscope (SEM) in backscattered electron (BSE) and secondary electron (SE) modes at an acceleration voltage of 15 keV. In addition, electron backscatter diffraction (EBSD) was performed with a step size of 50 nm to characterize the local phase distribution. The EBSD data were analyzed with the OIM Analysis^{TM} V9 software package. Kikuchi patterns were indexed using the spherical indexing method [117].

4.2.4. Synchrotron X-ray nano-computed tomography

Three-dimensional porosity of the samples reduced at 1 bar and 100 bar was investigated using synchrotron X-ray nano-computed tomography (nano-CT) in holotomography mode. The nano-CT experiments were conducted at the Nano-analysis Beamline ID16B of the European Synchrotron Radiation Facility (ESRF) [118]. The samples for the nano-CT measurements were prepared using focused ion beam cutting in an FEI Helios dual-beam system with a Xe plasma source. A cuboid lamellar with dimensions of 40 µm × 40 µm × 40 µm was lifted out and mounted on a copper rod with a sharp tip of ~60 µm in diameter. The cuboid lamellar was milled into a cone shape with a tip diameter of ~20 µm using focused ion beam (see Appendix **Fig.**A 1). In nano-CT experiments, samples were exposed to a monochromatic X-ray beam with an energy of 29.6 keV in a transmission mode. The two-dimensional projections were recorded by a PCO camera. The corresponding voxel size was 25 nm × 25 nm × 25 nm. The samples were rotated 360° during the NanoCT scans. For the sample reduced at 1 bar, a rotation speed of 3.98°/s was used with an exposure time of 30 ms per projection, yielding 3013 projections with a step size of approximately 0.12°. For the sample reduced at 100 bar, the rotation speed was increased to 5.95°/s with an exposure time of 30 ms per projection, yielding 2016 projections with a step size of approximately 0.18°. The phase retrieval process was performed using a custom in-house octave script based on a Paganin-like approach [119], with a delta/beta ratio of 78. The tomographic reconstruction was then performed using the standard filtered back-projection algorithm PyHST2 implemented at ESRF [120]. The semantic segmentation of pores was performed on stacks of 2D tomographic slices using deep learning [121]. For this, a U-Net architecture [122] with four encoding and likewise four decoding blocks was used. Each block consisted of two convolutional layers with

batch normalization and leaky ReLU activation. Down-sampling was performed via max pooling and up-sampling was performed using transposed convolutions. Skip connections, a main feature of the U-Net architecture, were employed between corresponding encoder and decoder blocks. Representative tomographic slices were manually labeled for training. For samples reduced at 1 bar, 6, 2, and 1 slice(s) were used for training, validation, and testing, respectively. For the more challenging 100-bar case (with finer pores and a higher porosity), 10, 2, and 2 slices were used. Models were trained for 200 epochs using the Adam optimizer with a batch size of 8 and a learning rate of 10^{-4}. Dice loss was used as the loss function. To increase data diversity and reduce overfitting, data augmentation was applied, including random horizontal and vertical flips, random rotations between -20° and 20°, and random cropping to 512 × 512 pixels. For inference, the models with the lowest validation Dice loss were used. Larger tomographic slices were segmented using a sliding-window approach with overlapping tiles in a checkerboard pattern. Overlapping predictions were averaged to obtain the final segmentation. The 3D rendering, and analysis of volume and connectivity of the pores were conducted using the software Dragonfly Version 2024.1. Furthermore, pore size distribution was analyzed using the granulometry algorithm in the software ImageJ [123].

4.3. Results

4.3.1. Reduction kinetics of hematite at different H_2 gas pressures

The real-time phase evolution during HyDR at different H_2 pressures was followed by *in-situ* HEXRD and the amounts of individual phases was plotted in **Fig. 22**. For all the samples, reduction started during the heating stage to 700 °C (at an average heating rate of 1.4±0.3 °C/s, see **Table 3**). In samples P1, P10, and P50, the reduction proceeded in a sequential manner, **Fig. 22**a-c. Hematite was first completely reduced to magnetite; subsequently, magnetite was reduced to wüstite, followed by the formation of α-iron. Notably, α-iron only appeared once a significant portion of magnetite had transformed into wüstite (*e.g.,* >83% of wüstite before α-iron appeared at 1 bar). In contrast, the P100 sample revealed a non-sequential reduction pathway, **Fig. 22**d. Particularly, α-iron and wüstite formed at a temperature of 450 °C and 495 °C, respectively, before hematite was fully consumed. Such non-sequential reduction behavior is attributed to the highly reactive atmosphere at 100 bar. Moreover, an increase in the H_2 pressure lowered both the onset

and completion temperatures of individual reduction steps (**Table 4**) as determined by the first appearance and complete disappearance of the XRD peaks associated with each phase. For instance, the onset temperature of the magnetite formation was 540 °C in the sample P1, while it sharply decreased by more than 100 °C to 430 °C in the sample P100. Such strong decreases of the onset temperatures suggest that HyDR is favored at lower temperatures as the H_2 pressure increases.

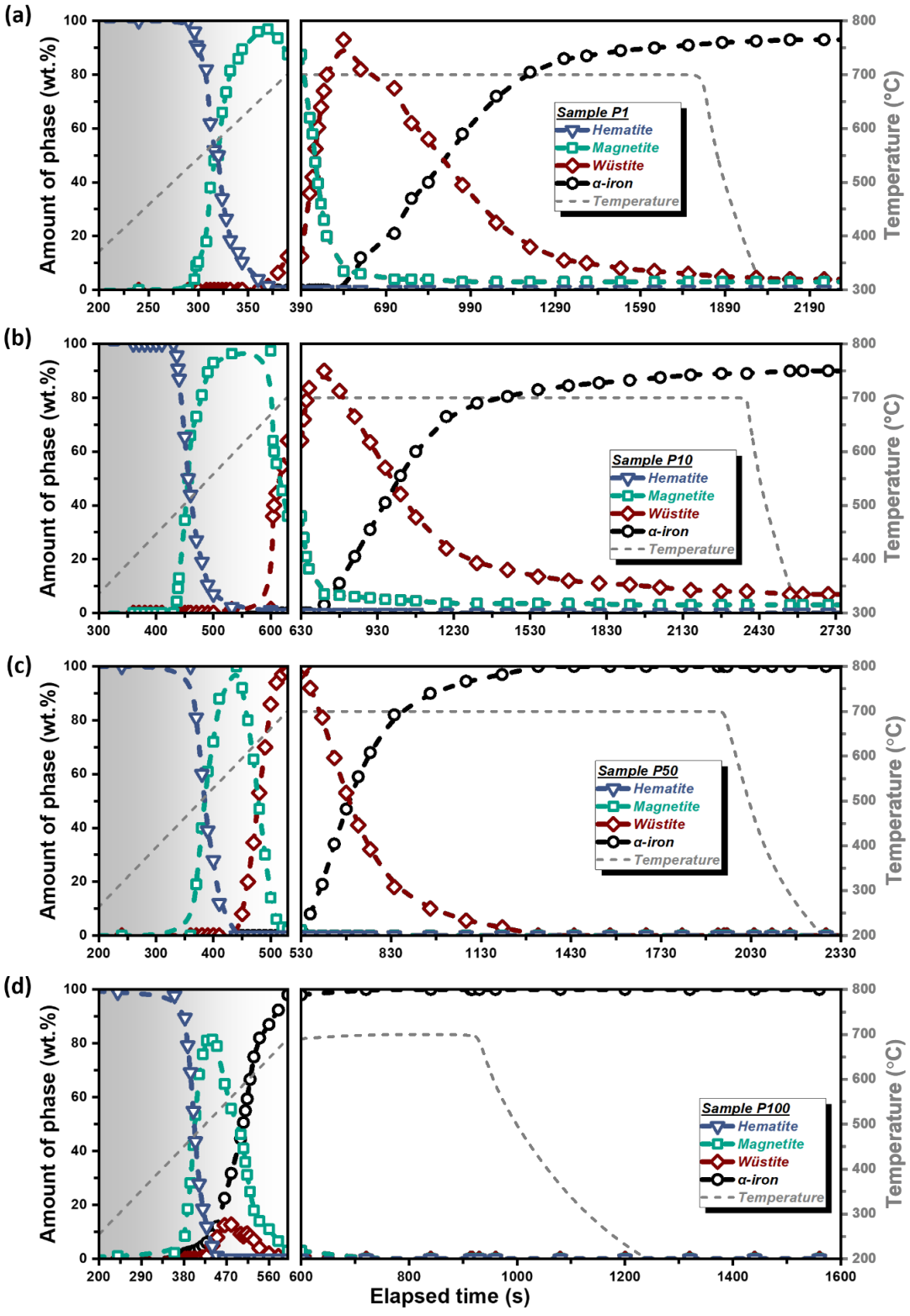

Fig. 22 Real-time phase evolution of hematite samples reduced at different H_2 gas pressures: **a)** 1 bar (P1), **b)** 10 bar (P10), **c)** 50 bar (P50), and **d)** 100 bar (P100). The amount of phase was measured by in-situ synchrotron high-energy X-ray diffraction.

Table 4 Onset and final (completion) temperatures (in °C) for each phase formed during the hydrogen-based hematite reduction for samples P1, P10, P50, and P100. (Deviations in temperatures were determined based on the difference between the reaction cell temperature and the fitted temperature, and quantified using standard deviation analysis.)

Phase	P1 (±7.4 °C)		P10 (±14.1 °C)		P50 (±25.6 °C)		P100 (±7.8 °C)	
	Onset	Final	Onset	Final	Onset	Final	Onset	Final
Magnetite	540	684	485	674	475	580	430	544
Wüstite	666	700	595	700	580	700	495	700
α-iron	700	700	700	700	700	700	450	700

The evolution of the amount of α-iron revealed a sigmoid shape. Also, among all phase transformations in the P1, P10, and P50 samples, the reduction of wüstite to α-iron was the most sluggish reaction and thus kinetically most limiting step. For example, hematite reduction to magnetite and magnetite to wüstite required on average of 100±10 s and 170±70 s, respectively, for ~95% completion. In contrast, the reduction of wüstite to α-iron required a significantly longer duration, with ~90% transformation taking place over an average of 1200±400 s, **Fig. 22**a-c.

The acceleration of HyDR by the enhanced H_2 pressure was also evidenced by higher reduction rates of individual reaction steps and a higher overall reduction degree (**Fig. 23**). An increase in H_2 pressure elevated the consumption rate of hematite systematically. For instance, it was ~6.8 times higher in sample P100 compared with that in sample P1, as shown in **Fig. 23**a. Moreover, the formation rate of α-iron was also promoted by H_2 pressure. At the local maxima (at ~50 wt.% of α-iron), the formation rates of α-iron were enhanced by a factor of 1.3, 2.7, and 6.5 for the samples P10, P50, and P100, respectively, as compared with that of the sample P1, **Fig. 23**b. For the overall reduction kinetics (as calculated based on the method described in Appendix 8.1.1.), as shown in **Fig. 23**c, the sample P1 reached 0.14 (corresponding to 13 wt.% wüstite and 87 wt.% magnetite in the sample) when it was heated to 700 °C; while an increase in H_2 pressure to 50 bar accelerated the reduction to an overall reduction degree of 0.33 (the sample consisting of 98 wt.% wüstite and 2 wt.% magnetite). The sample P100 was completely reduced to α-iron during heating, achieving an overall reduction degree of 1.00 at the time when temperature reached 700 °C. During HyDR at 700 °C, iron oxides (here, mainly wüstite and magnetite) were gradually reduced into α-iron in the samples P1, P10, and P50, **Fig. 22**a-c. Within the elapsed time during the HEXRD experiments, the amount of α-iron reached 93 wt.%, 90 wt.%, and ~100 wt.% in the samples P1, P10, and P50, respectively, **Fig. 22**a-c. These corresponded to overall reduction degrees of 0.96,

0.95, and 1.00, respectively, **Fig. 23**c. Due to the sluggish reduction kinetics in the last step, there was a small amount of oxides unreduced in the sample P1 (3 wt.% magnetite and 4 wt.% wüstite) and P10 (3 wt.% magnetite and 7 wt.% wüstite).

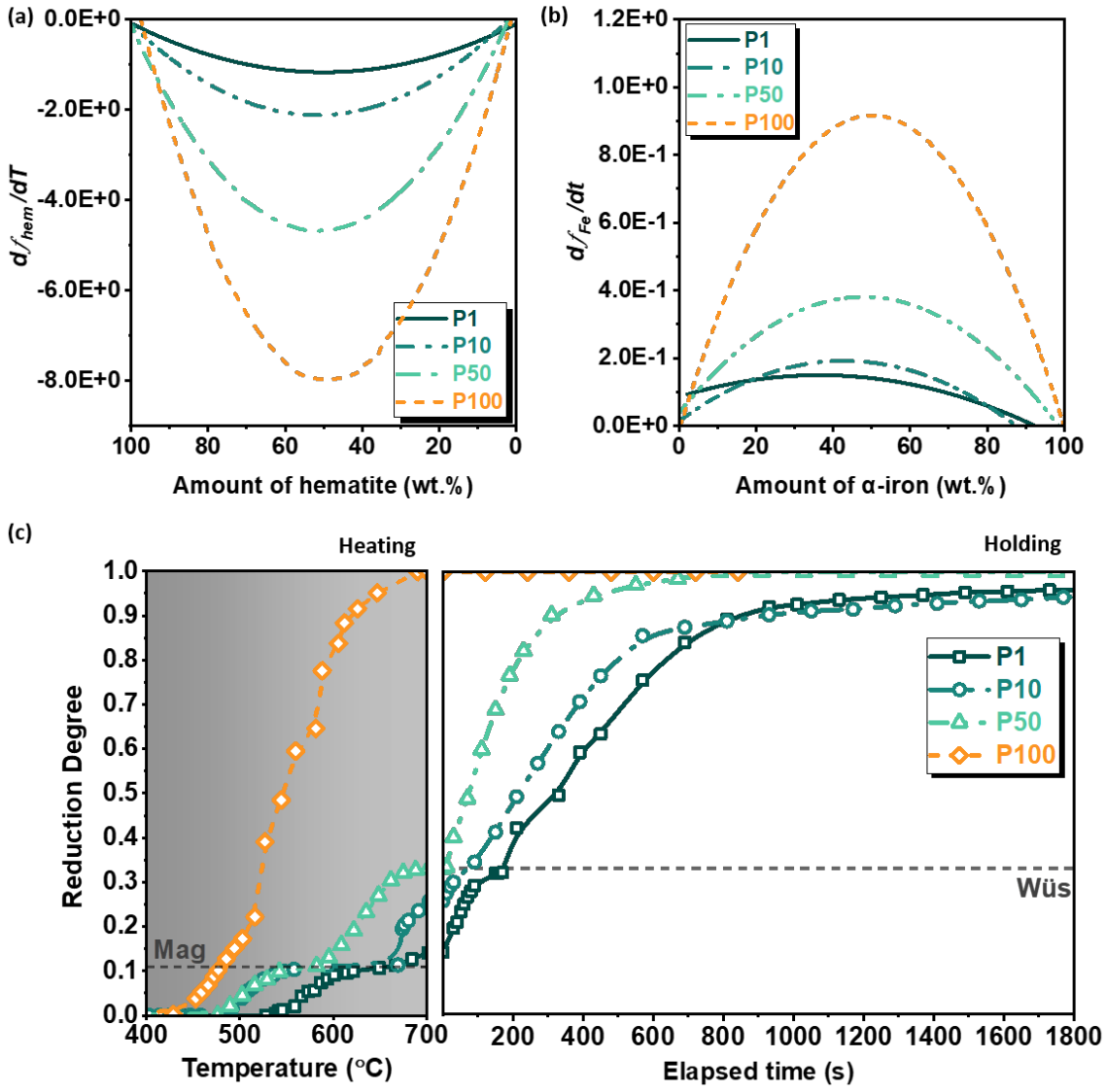

Fig. 23 Kinetics of HyDR at different H_2 pressures. **a)** Consumption rate of hematite as a function of the amount of remaining hematite in wt.%. The consumption rate was calculated from the derivative of the amount of hematite against temperature (df/dT) during heating to 700 °C. **b)** Formation rate of α-iron as a function the amount of the produced α-iron in wt.%. The formation rate was calculated from the derivative of the amount of α-iron against time (df/dt), since α-iron formation was under an isothermal condition for the samples P1, P10, and P50 during holding at 700 °C, and under a non-isothermal condition for the sample P100 during heating to 700 °C. **c)** Overall reduction degree as a function of temperature during heating stage and as a function of relative time during holding at 700 °C . The dotted lines refer to the reduction degrees of the completed reduction from hematite to magnetite (0.11) and from hematite to wüstite (0.33)

4.3.2. Microstructure evolution during HyDR at different H_2 gas pressures

Microstructures of the partially reduced samples at the H_2 pressure of 1 bar for 900 s (P1-900s, the corresponding reduction degree was 0.56) and 100 bar for 180 s (P100-180s, the corresponding reduction degree was 0.27) are shown in **Fig. 24**. The samples revealed distinct spatial distribution behavior of α-iron. The micrograph (**Fig. 24**a) suggested the formation of α-iron in sample P1 was primarily on the surfaces of oxide particles in the regions accessing inherited pores, as confirmed by the EBSD phase map, **Fig. 24**b. In contrast, ultrafine-grained α-iron (~100 nm) was observed within the oxide particles in the sample P100 during the early stage of the α-iron formation, **Fig. 24**c and **24**d. Considering the three-dimensionality of the sample, this feature can be attributed to a progressing metal-oxide phase boundary initiated by α-iron nucleation at an internal pore surface or the outer surface of sample during reduction.

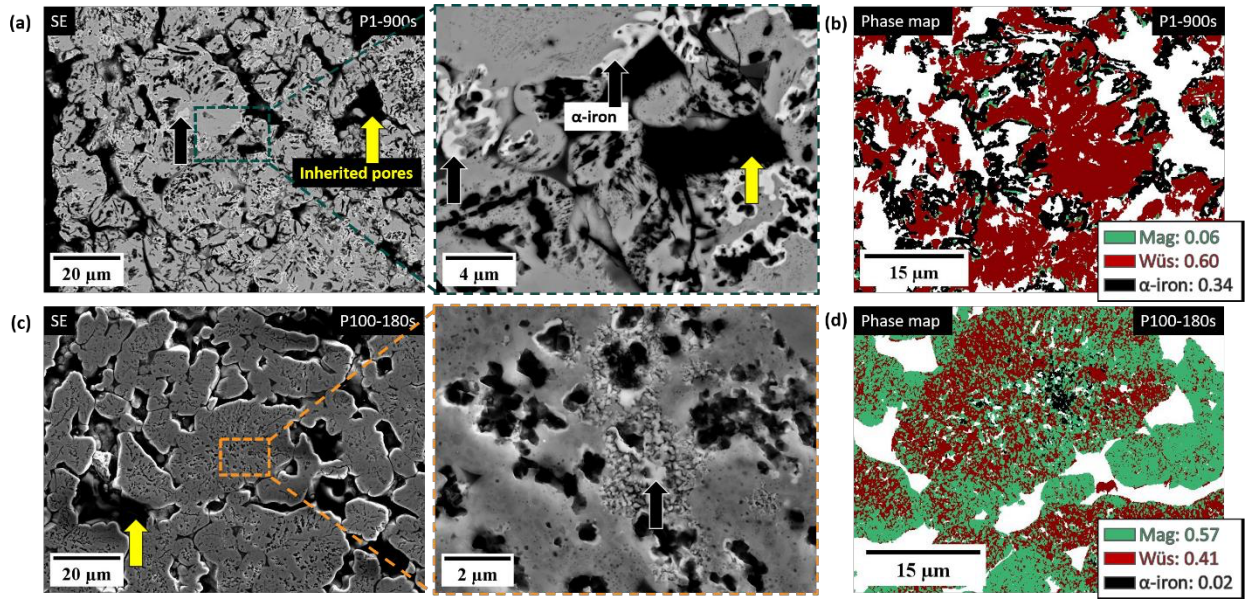

Fig. 24 Microstructures of the partially reduced samples: Secondary-electron images of the specimen **a)** P1 reduced for 900 s (P1-900s) and **c)** P100 for 180 s (P100-180s), where α-iron is highlighted by black arrows; **b)** and **d)** Phase maps of P1-900s and P100-180s probed by electron backscatter diffraction.

Fig. 25 shows the microstructure of the specimens after the HEXRD experiments. The hematite specimen containing inherited pores and dense hematite particles (**Fig. 25**), transformed into porous α-iron (**Fig. 25**b-e). Some remaining oxide islands were observed in specimens P1 (**Fig. 25**b) and P10 (**Fig. 25**c), surrounded by metallic iron. The average grain size of α-iron was reduced by an increase in H_2 pressure, **Fig. 25**f. For instance, the average grain diameter of the specimen

P1 was 0.50±0.40 µm, and it was reduced to 0.30±0.20 µm in the specimen P100. Such notable grain refinement is mainly due to the high density of iron nucleation events occurring on the oxide surface during HyDR under high thermodynamic driving force of reaction at elevated H_2 pressure conditions, as discussed in Ref. [53].

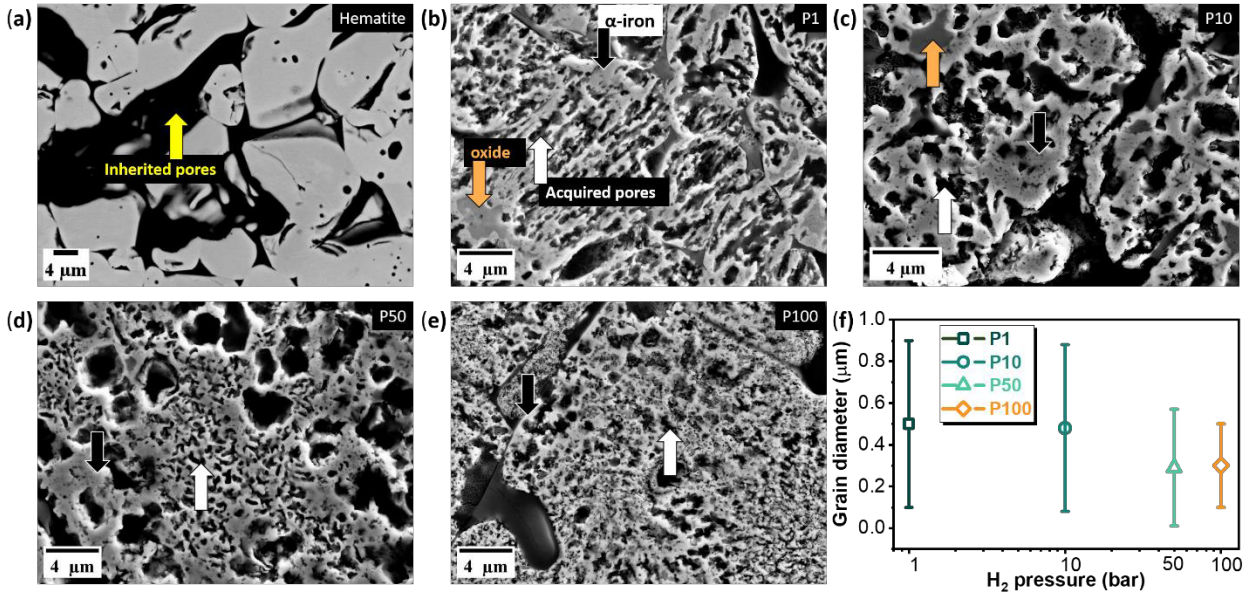

Fig. 25 Effect of H_2 gas pressure on the microstructure of the reduced specimens: The microstructures of reduced specimens **a)** unreduced hematite sample **b)** P1, **c)** P10, **d)** P50, and **e)** P100; The yellow and white arrows mark inherited and acquired pores, respectively. The orange arrow marks remaining oxide layers. **f)** The grain diameter of α-iron as a function of H_2 gas pressure measured by electron backscatter diffraction.

The pore structure is a crucial microstructural characteristic of direct reduced specimens. Connected pores enable the diffusion of H_2 gas molecules to the interior surfaces of the sample and facilitate the efficient outward diffusion of H_2O molecules to the gas stream. They also serve as fresh surfaces for the reduction reactions to occur. Thus, the connectivity of pores has a significant impact on the reduction kinetics of HyDR [61, 77]. To investigate H_2 gas pressure effect on the structure and connectivity of pores, 3D pore analysis of P1 and P100 specimens was conducted using synchrotron X-ray nanoCT (**Fig. 26**). As shown in **Fig. 26**a, the pore morphology of reduced α-Fe evolved with the increase in H_2 pressure. Consistent with our previous findings [53], the P1 sample possessed large, elongated pores (**Fig. 26**a (i)), which changed into finer and more random-shaped pore morphology with an increase in H_2 pressure to 100 bar (**Fig. 26**a (ii)), (see also **Fig. 25**b-e). 3D analysis of pores revealed that the P100 sample exhibited lower overall porosity (37.6%) compared with the P1 sample (49.1%), which aligns well with 2D pore analysis results, 46.8±5.0% for P1 and 40.0±4.0% for P100, **Fig. 26**c. The fraction of isolated pores in the

P100 specimen (1.38%) was nearly eight times higher than that of P1 specimen (0.18%), indicating a substantial increase in pore isolation with increasing H_2 gas pressure, **Fig. 26**b and **26**c. However, it is worth noting that some pore interconnections may still be present in the P100 sample but fall below the spatial resolution limit of the nanoCT technique (in this study, it is ~100 nm). Features smaller than 100 nm are considered artifacts resulting from data processing. Consequently, pore connectivity (calculated as the volume fraction of connected pores divided by the total pore volume fraction) decreased slightly, declining from 99.6% in P1 to 96.3% in P100. In addition, the average pore diameter of the P1 sample (0.73 µm) was three times larger than that of the P100 sample (0.23 µm), **Fig. 26**d.

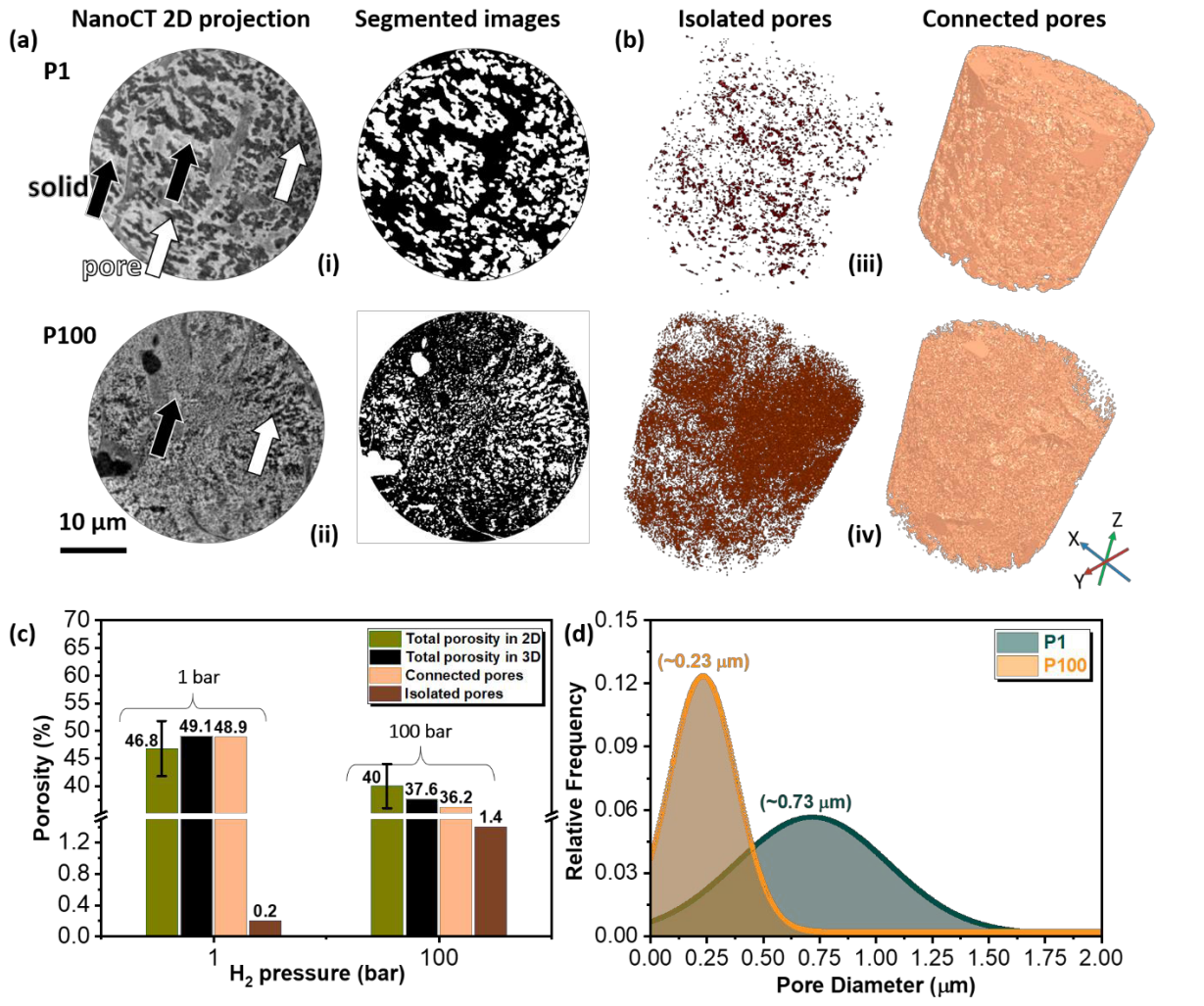

Fig. 26 X-ray nanoCT analysis of porosity in samples P1 and P100. **a)** 2D projection images from nanoCT scans, with black and white arrows indicating pore regions and solid phases and corresponding segmented binary images where white represents pores and black represents the solid phase of (i) P1 and (ii) P100 specimens. **b)** 3D visualization of isolated and connected pores in (iii) P1 and (iv) P100 specimens. **c)** Evolution of 3D porosity at varying H_2 gas pressures: total, connected, and isolated porosity (Analysis based on nanoCT) and 2D porosity (Analysis using secondary electron images of the entire cross-section of specimens

magnified 500× after reduction). **d)** Pore size distribution of P1 and P100 specimens analyzed using granulometry algorithm using the software ImageJ [123].

4.4. Discussion

4.4.1. Kinetics of overall reaction

The results reveal that the rate of overall reduction is dependent on H_2 gas pressure and gets enhanced with increasing H_2 pressure (**Fig. 22** and **Fig. 23**c). Under static pressure conditions, the partial pressure of H_2 (P_{H_2}) in the system increases with the applied H_2 gas pressure ($P_{H_2}^{100} > P_{H_2}^{50} > P_{H_2}^{10} > P_{H_2}^{1}$). Thus, the enhanced reduction rate at elevated H_2 pressures and the decrease in the reaction onset temperature can be attributed to the following reasons [47, 124]; (i) Enhanced thermodynamic driving force: Increasing P_{H_2} in the reducing gas atmosphere decreases the Gibbs free energy of the reduction reaction (see Appendix **Fig.A** 3) [28, 53] and increases the chemical potential gradient of oxygen between the solid and gas phases [124]. This fact strengthens the thermodynamic driving force for iron formation and promotes larger oxygen flux from the oxide to the gas phase to reduce the chemical potential of oxygen in the solid [28, 125]. (ii) Enhanced solid-gas interaction in a closed system: Higher H_2 pressure raises the molecular collision frequency (*e.g.,* as H_2 gas pressure increases, the collision frequency of H_2 molecules rises by two orders of magnitude, *i.e.,* from ~8.85×10^7 s^{-1} at 1 bar to ~8.83×10^9 s^{-1} at 100 bar at 700 °C) and reduces the mean free path (*i.e.,* from 362,1 nm at 1 bar to 3,621 nm at 100 bar) [125], thereby increasing the quantity of impinging H_2 molecules on the solid surface, thus significantly raising the probability of chemical reaction occurrence on the surface (see Appendix **Fig.A** 2). (iii) Enhanced surface coverage of monoatomic hydrogen: Higher H_2 pressures increase the adsorption and dissociation of H_2 molecules α-iron, wüstite, and magnetite on the surfaces. This leads to higher surface concentrations of reactive atomic hydrogen, thereby accelerating reduction reactions taking place on the surface [101, 102]. (iv) Enhanced H_2 and H_2O diffusion flux: Increased chemical potential gradients of H_2 and H_2O (within interconnected pores and at the reaction interface) under high-pressure conditions promote greater molecular flux. This results in more efficient transport of H_2O away from the reaction front compared to low-pressure systems.

4.4.2. Mechanism of rate-limiting reaction step

During HyDR, the reduction of hematite occurred stepwise (Chapter 4.3.1.). Based on the HEXRD results, the most sluggish reaction among individual reactions was transformation of wüstite into α-iron in all specimens (**Fig. 22**a-c), acting as rate-limiting reaction. Here, the effect of H_2 gas pressure on the kinetics of this rate-limiting reaction (*i.e.,* from wüstite to α-iron) will be discussed based on the kinetic model fitting method of the experimentally measured kinetics. Note that the kinetic models were applied exclusively to the specimens P1, P10, and P50, as the reduction from wüstite into α-iron in these samples occurred under isothermal conditions.

The rate of a solid-gas reaction (here, wüstite reduction with H_2) can be formulated by Eq. (4.2):

$$\frac{dX}{dt} = k(T)f(X) \tag{4.2}$$

where, X is the conversion degree of wüstite to α-iron ($X = 0$ corresponds to wüstite, $X = 1$ to α-iron), $f(X)$ is kinetic model of the solid-gas reaction to be fitted and $k(T)$ is the rate constant, given by the Arrhénius equation:

$$k(T) = Ae^{-\left(\frac{E_a}{RT}\right)} \tag{4.3}$$

where, A is the pre-exponential factor, E_a is the activation energy in kJ/mol, T is temperature in Kelvin, and R is the gas constant.

Integrating Eq. 4.2, the reaction rate can be expressed as $g(X)$:

$$g(X) = \int \frac{1}{f(X)} dX = kt \tag{4.4}$$

To identify the rate-controlling mechanism of this reaction step, four kinetic models, i.e., gas-film (GF) model, phase-boundary (PB) model, nucleation and growth (NG) model, and solid diffusion (SD) model, were employed, as listed in **Table 5**. Each model reflects distinct physical mechanisms governing a solid-gas reaction. The GF model, also known as the gas diffusion model, assumes that the reaction rate is limited by diffusion rate of H_2 molecules to the sample surface through the gas boundary layer surrounding the reacting solid [126]. The PB model, also known as the core-shell or geometrical contraction model, proposes that the reaction initiates at the outer surface of the solid, forming a solid-solid interface (*e.g.,* oxide-oxide or oxide-α-iron) that moves inward toward the core [126, 127]. The advancement rate of this reaction interface limits the rate

of the reaction. According to the NG model, which is also known as Avrami-Erofeev model, reaction is limited by the nucleation and subsequent growth of the product phase[127]. The SD model assumes that the reaction is controlled by the diffusion of reactants and products through the product layer of the reaction [126].

Table 5 Mathematical description of the kinetic models for solid-gas reactions. In NG model, n donates the dimensionality of nuclei growth (ranging from 2 to 4).

Kinetic model	**Abbreviation**	**Integral form $g(X) = kt$**	**Ref.**
Gas film	GF	X	[126]
Phase boundary	PB	$1-(1-X)^{1/3}$	[126, 127]
Nucleation and growth	NG	$(-ln(1-X))^{1/n}$	[128]
Solid diffusion	SD	$1-3(1-X)^{2/3}+2(1-X)$	[126, 127]

The quality of fitting for each reaction model was assessed using the coefficient of determination (R^2), as summarized in **Table 6**. In all cases, the R^2-values for the PB and NG models were higher than those of the GF and SD models. However, these models do not account for the effect of porosity. This fact may lead to inaccurate interpretation of the kinetic behavior, as the rate of a reaction can additionally be controlled by the diffusion of gas molecules through the connected pores in a porous solid. To verify this, the Thiele modulus (Φ^2) was used to distinguish among controlling regimes of (i) reactant gas diffusion control through pores ($\Phi^2 > 10^3$), (ii) a mixed-control regime ($1 < \Phi^2 < 10^3$), and (iii) a surface reaction controlled regime ($\Phi^2 < 1$) [129]. The Thiele modulus (Φ^2) was estimated based on Eq. (4.5) (see Appendix 8.1.2.):

$$\Phi^2 = \frac{k_n r_p}{D_{eff}} \tag{4.5}$$

where, k_n is the rate constant for the reduction (*i.e.,* here from wüstite to α-iron), r_p is the half-length of the specimen (*i.e.*, ~3 mm), which has a rectangular prism shape, and D_{eff} is effective diffusivity [95]. The calculated Φ^2 values for reduction at 1 bar and 100 bar are 6.5×10^{-7} and 8.6×10^{-5}, respectively, indicating that all reactions are limited by chemical reactions under the boundary conditions in this study, rather by the diffusion of gas molecules through the connected pores. Therefore, it is appropriate to treat the sample as a collection of particles rather than as a continuous pellet.

Table 6 The goodness of model fitting, as quantified by R^2-values. The best fit of the kinetic models is highlighted in **bold**. GF, PB, NG, and SD stand for gas film, phase boundary, nucleation and growth and solid state diffusion, respectively.

Specimen	Reaction designation	Reaction condition	GF	PB	NG	SD
P1	$X^{1}_{\text{Wüs}\rightarrow\alpha-\text{iron}}$	Isothermal	0.674	**0.998**	0.991	0.941
P10	$X^{10}_{\text{Wüs}\rightarrow\alpha-\text{iron}}$	Isothermal	0.477	**0.995**	0.994	0.905
P50	$X^{50}_{\text{Wüs}\rightarrow\alpha-\text{iron}}$	Isothermal	0.634	0.996	**0.998**	0.976

Fig. 27 compares the fitted NG and PB models for conversion degrees of wüstite to α-iron in specimens P1, P10, and P50. Both PB and NG models yielded similarly quality of fits for the wüstite to α-iron conversion in all specimens, as indicated by the very close R^2-values, **Table 6**, which can lead to ambiguity between the PB and NG models. To resolve this uncertainty, microstructural investigations of partially reduced specimens was conducted. For P1 specimen, α-iron initially forms near the pores and progressively covers the wüstite as a core-shell structure, as shown in **Fig. 24**b, which indicates that the PB model is the controlling mechanism for wüstite particles. The EBSD phase maps of partially reduced P10 (for 600 s, **Fig. 28**a), and P50 (for 450 s, **Fig. 28**b) specimens show that α-iron nucleation starts from the surface of wüstite (on the vicinity of pores) and grows toward the center of the particle with a local core-shell structure, similar to P1 specimen (**Fig. 24**b). These findings suggest that conversion of wüstite into α-iron is more likely controlled by PB model in all P1, P10, and P50 specimens at the individual particle level.

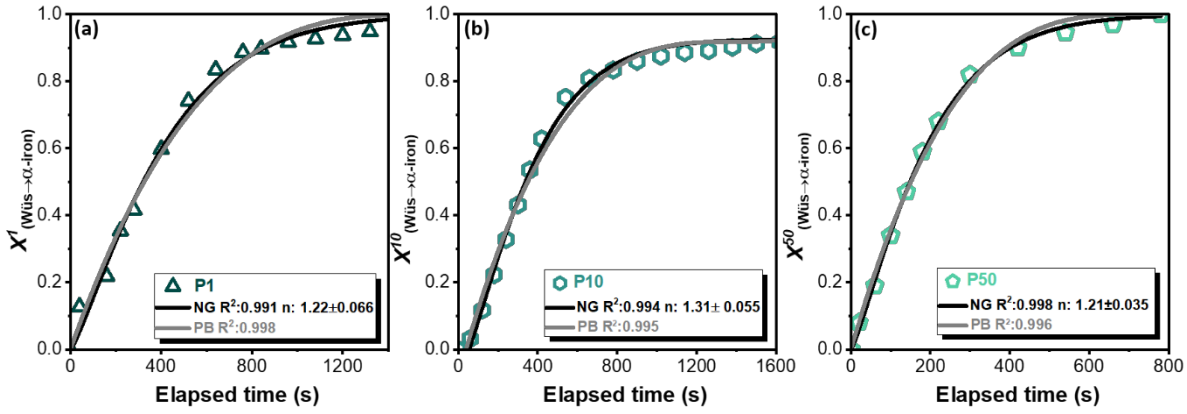

Fig. 27 Fitting curves of the nucleation and growth (NG) and phase-boundary (PB) models to the conversion degrees of wüstite to α-iron at different H_2 gas pressures of **a)** 1 bar, **b)** 10 bar, and **c)**50 bar, respectively.

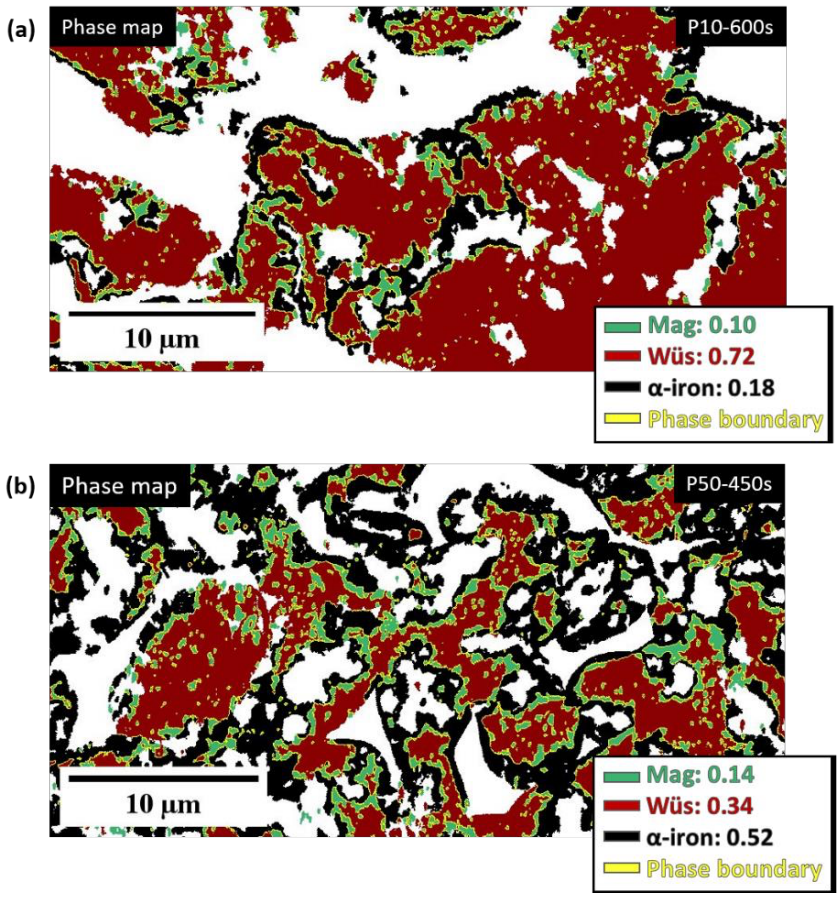

Fig. 28 Electron backscatter diffraction (EBSD) maps of specimens partially reduced with H_2 at 700 °C: **a)** Specimen P10 reduced for 600 s; **b)** Specimen P50 reduced for 450 s. The yellow line donates boundaries between magnetite, wüstite, and α-iron phases. White regions within the image frame represent pores in the reduced specimen.

The advancement rate of this wüstite-iron interface is governed by oxygen removal kinetics from wüstite to a free surface through α-iron [6, 91]. As reported by Hayes, the interface velocity, V_m, depends on P_{H_2}, the rate of reaction in the forward direction, ϕ_m^1, and the Gibbs free energy of the reaction, $\Delta G_{reaction}$. V_m increases with higher P_{H_2} and lower $\Delta G_{reaction}$, resulting in faster advancement of wüstite-iron interface as shown in Eq. (4.6) [28].

$$V_m = \left(\frac{b_m}{\rho_m h_m}\right) \phi_m^1 P_{H_2} \times \left[1 - \exp\left(\frac{\Delta G_{reaction}}{RT}\right)\right] (ms^{-1}) \qquad (4.6)$$

where, b_m, h_m, and ρ_m are the length of the interface, the thickness of the metal layer, and the density of the metal, respectively. An increase in P_{H_2} enhances the oxygen removal rate [28, 80], thereby accelerating advancing interface. In addition, the increase in the rate of the advancing

interface can be attributed to the exponential decrease in the reaction Gibbs free energy ($\Delta G_{reaction}$) with increasing P_{H_2} according to Eq. (4.7):

$$\Delta G_{reaction} = \Delta G^0 + RT \ln \frac{(P_{H_2O})^3}{(P_{H_2})^3}. \quad (4.7)$$

where, ΔG^0 is the standard Gibbs free energy of the reaction and P_{H_2O} is the partial pressure of H_2O.

4.4.3. Influence of H_2 gas pressure on the formation of pores

Next, we discuss the change in the pore's morphology from an elongated shape to an equiaxial shape as the H_2 pressure increased from 1 to 100 bar (**Fig. 24** and **Fig. 26**a). Pore formation predominantly occurs during the last reduction step due to the highest relative volume loss by ~41% in the transformation step from wüstite to α-iron. As shown in **Fig. 29**a and **29**b, the oxide region remains mostly dense whereas iron regions are more porous. During wüstite reduction, pores form due to the removal of oxygen atoms from the wüstite lattices. The oxygen atoms diffuse through the α-iron lattice to an open surface to produce H_2O with H_2. At the wüstite-iron interface, wüstite dissociates into iron and oxygen atoms, resulting in the formation of a vacant oxygen ion site, a neutral iron atom, and an interstitial neutral oxygen atom within the α-iron lattice [30], as demonstrated in the reaction below:

$$Fe_{Fe}^x + O_O^x \rightarrow Fe_{metal}^x + V_o^x + O_i^x$$

where, Fe_{Fe}^x and O_O^x represents an iron cation and an oxygen anion occupying their regular lattice sites in wüstite, respectively. Fe_{metal} donates a neutral iron atom participating to the metallic iron phase. V_o^x is an oxygen vacancy at the metal wüstite-iron interface and O_i^x represents a neutral oxygen atom occupying an interstitial site in α-iron lattice. The removal of oxygen at the wüstite-iron interface and formation of vacant oxygen sites lead to interfacial rearrangement due to the volume mismatch between wüstite (82.45 $Å^3$ at 700 °C) and α-iron (24.42 $Å^3$ at 700 °C) lattices and results in formation of voids at the interface [63, 65]. Newly formed vacant oxygen sites participate in voids to further reduce the interfacial energy by decreasing the total surface area produced with void formation [66]. This phenomenon is assumed to be one of the dominant mechanisms resulting in development of acquired pores.

During reduction the morphology of pores is governed by the velocity of the advancing interface [64]. According to Eq. (4.6), the velocity of the wüstite-iron interface is proportional to P_{H_2} and is inversely proportional to $\Delta G_{reaction}$. This causes an exponential increase in the rate of the advancing interface as H_2 gas pressure increases, as shown in **Fig. 29**c (see Appendix 8.1.3. for plot details). In contrast, the mobility of a vacancy is only temperature-dependent and unaffected by P_{H_2} (**Fig. 29**c, indicated by grey blue dotted line).

At lower P_{H_2} (*e.g.,* ≤10 bar), the lower mobility of interface allows vacancies to migrate and coalesce into larger voids at the interface (**Fig. 29**e (i)-(ii)). This facilitates directional pore growth perpendicular to the advancing interface, resulting in formation of elongated pores (**Fig. 29**e (iii), bottom) within the reduced α-iron layers. Thus, at 700 °C and low pressure regime (1 to 10 bar), the pore morphology is interface velocity controlled (green region in **Fig. 29**c) [65, 130]. In contrast, at higher P_{H_2}(*e.g.,* ≥50 bar), the interface advancement is accelerated. The diffusion of vacancies is not able to catch up with the interface movement. Consequently, any voids that form at the interface will be left behind as the interface advances. This results in a fine, equiaxed, and uniformly distributed pores (**Fig. 29**e (iii), top), as observed in P50 (**Fig. 25**d) and P100 (**Fig. 25**e) specimens, which formed via vacancy mobility controlled mechanism (**Fig. 29**c, light orange region). This fact also leads to a decrease in the connectivity of pore in the reduced specimen. Moreover, the porosity was observed to be lower in P100 specimen (37.6%) than P1 specimen (49.1%). This difference might stem from the pressure-assisted densification of iron grains at 700 °C [131].

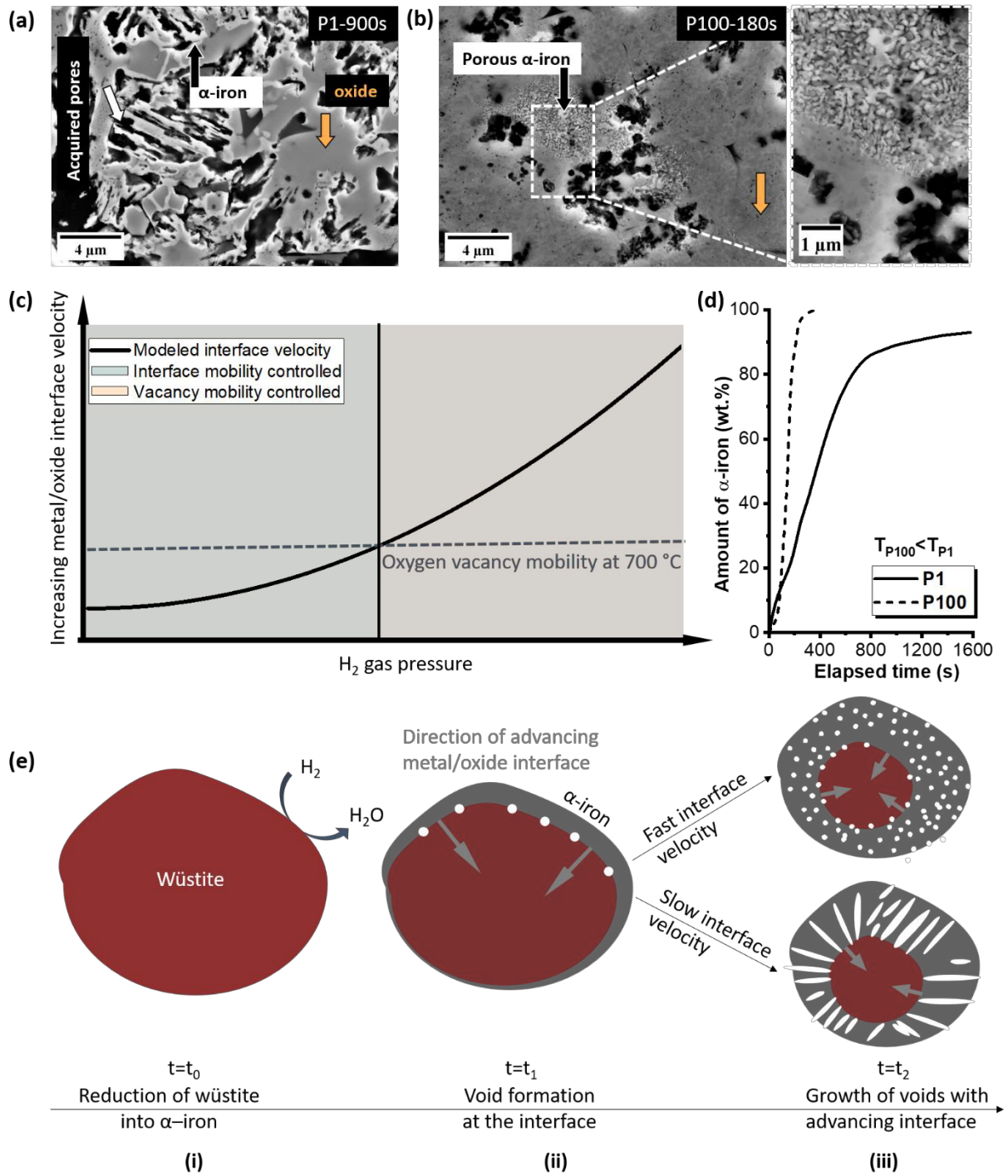

Fig. 29 Effect of H_2 gas pressure on the morphology of acquired pores. SE images showing the cross-sectional area of the **a)** P1 and **b)** P100 specimens after partial reduction at 700 °C. **c)** Schematic plot illustrating the interface velocity and mobility of a vacancy as a function of H_2 gas pressure. At low pressure (green region), the pore morphology is controlled by the advancing interface. At high pressure (orange region), the pore morphology is controlled by the local coalescence of vacant oxygen sites. **d)** The amount of α-iron forming as a function of time. Dash lines indicate the change in the amount of α-iron in P100 specimen, whereas the solid line shows the change in the amount of α-iron changes as a function of time at P1 specimen. **e)** Conceptual model sketch describing the effect of the rate of advancing wüstite-iron interface on morphology of pores at different H_2 gas pressures: (i) the onset of wüstite reduction, (ii) formation of α-iron layer on wüstite surface and void formation at the wüstite-iron interface (iii) growth of voids into elongated, and equiaxed pores at low, and high H_2 gas pressures, respectively.

4.5. Conclusion

In this study, we employed *in-situ* synchrotron high-energy X-ray diffraction to study the hydrogen-based direct reduction of hematite at different H_2 gas pressures (from 1 bar to 100 bar) at 700 °C. This approach enabled resolve the individual reduction steps in real time, allowing us to identify the rate-limiting reaction mechanism and its dependency on H_2 pressure. In addition, we used X-ray nano computed tomography to assess the effect of H_2 gas pressure on the three-dimensional pore structures. The main conclusions are summarized as follows:

(1) Elevated H_2 pressure lowered the onset temperatures of reduction steps, providing a more favorable thermodynamic condition for the reactions to initiate at lower temperatures.

(2) Overall reduction kinetics improved with increasing H_2 gas pressure, as the reaction rates of all individual steps (*i.e.,* hematite to magnetite, magnetite to wüstite, and wüstite to α-iron) were accelerated (*i.e.,* the rate of α-iron formation was 6.5 times faster at P100 sample then P1 sample). The pressure effect became particularly pronounced at 50 and 100 bar, where enhancement of reaction rates was substantial (*e.g.,* when temperature reached at 700 °C, the reduction degree was 0.14 at 1 bar, 0.33 at 50 bar, and 1.00 at 100 bar)

(3) The reduction of wüstite to α-iron was identified as the rate-limiting step at all studied H_2 pressures. Analysis of reaction kinetics and microstructure confirmed that this step follows a phase-boundary-controlled mechanism at 1, 10, and 50 bar H_2 gas pressures. Increasing the H_2 pressure significantly enhanced the thermodynamic driving force and kinetics of this transformation step by accelerating the rate of the advancing wüstite-iron interface.

(4) Pore morphology evolved with H_2 pressure, transitioning from elongated structure at ambient pressure to an equiaxed structure at elevated H_2 pressures. This transition is attributed to a shift in the balance between vacancy diffusion and interface mobility: at low pressure, faster vacancy diffusion to advancing interface led to elongated pore, whereas at high pressure, accelerated interface advancement outpaced vacancy mobility leaving behind equiaxed pores.

Overall, H_2 pressure plays a critical role in both the reduction kinetics and microstructural evolution during hydrogen-based direct reduction of iron oxides. This underscores the importance of carefully controlling gas pressure in the design and optimization of industrial-scale hydrogen-based direct reduction reactors.

5. HOW MUCH HYDROGEN IS IN GREEN STEEL?

This chapter is based on the publication: Özge Özgün, Xu Lu, Yan Ma, Dierk Raabe (2023). How much hydrogen is in green steel?. *npj Materials Degradation*, *7*(1), 78.

Hydrogen-based reduction of iron ores is the key technology for sustainable ironmaking, to mitigate the CO_2 burden from the steel industry, accounting for ~7-8% of global emissions. However, hydrogen can lead to catastrophic failure of metallic parts, a phenomenon called hydrogen embrittlement. This raises the question of how much hydrogen remains from green ironmaking in the metal produced. Here we answer this question by quantifying the amount of hydrogen in iron produced via hydrogen-based direct reduction and hydrogen-based plasma smelting reduction. We show that using hydrogen in green steel production is not creating a threat of hydrogen embrittlement.

5.1. Introduction

Steel is the most important metallic material in terms of versatility (>3500 grades) and production quantity (1.95 billion tons in 2021[132]), serving in construction, energy conversion, infrastructure, transport, safety, and appliances, *etc*. However, the steel industry stands for about 7-8% of the global CO_2 emissions, making it the largest cause of global warming[3]. Particularly, the primary steel synthesis, responsible for about two thirds of today's global steel market, is highly CO_2-intensive owing to the use of fossil reductants (such as coal, coke, or natural gas) to reduce iron oxides[133]. It emits on average ~2 tons of CO_2 per ton of crude steel [134]. Because of the growing global steel demand and its longevity (often >50 years in construction and >25 years in machines[12]), the volume made via primary synthesis will remain on a similar level as today during the next decades. Thus, alternative synthesis methods with drastically reduced CO_2 emissions must be urgently developed to overcome the decarbonization challenge for steel[135].

Hydrogen-based reduction processes have qualified in recent years as possible alternatives, provided that a sufficient amount of green hydrogen is available and economically viable[136-138]. In this case, the by-product of the redox reaction is water. Hydrogen-based reduction works with solid and liquid oxides, where the former is referred to as hydrogen-based direct reduction (HyDR)[139] and the latter as hydrogen plasma smelting reduction (HPSR)[140]. In both processes, hydrogen not only reduces iron oxides but can also get trapped inside the produced metal. The latter effect has fueled concerns about the amount of hydrogen remaining in green steel, as even a few ppm of diffusible and weakly trapped hydrogen can have an enormously embrittling effect, particularly on advanced high-strength steels, leading to catastrophic failure[141, 142]. This detrimental phenomenon, known as hydrogen embrittlement, has been studied for nearly 150 years[143]. Different mechanisms have been explored as possible causes for this effect[144], including hydrogen-enhanced localized plasticity[145, 146], hydrogen-enhanced decohesion[147], hydrogen adsorption-induced dislocation emission[148], hydrogen-enhanced strain-induced vacancy formation[149]. For all these potential internal damaging mechanisms, the types of hydrogen traps inside the material are of high relevance[150]. Here, hydrogen traps refer to microstructural features, which absorb and capture hydrogen atoms[151].

Thus, the use of hydrogen creates a nexus between sustainable steel production and hydrogen embrittlement. This concern must be taken seriously because steel serves as the backbone material

in safety-critical components and green steel that is not safe would be useless. Motivated by this conflict, we study here two key questions that need to be answered before implementing hydrogen as a reductant at the industrial scale for green steel production: (1) How much hydrogen is in green steel? (2) Will green steel suffer from severe hydrogen embrittlement? To answer these questions, we investigate the concentration of residual hydrogen in iron produced by hydrogen-based ironmaking processes using thermal desorption spectroscopy

5.2. Methods

5.2.1. Materials and process

Commercial hematite pellets were used in this study. HyDR was conducted in a laboratory thermogravimetry analysis set-up [152]. The pellets were exposed to pure hydrogen gas (purity of 99.999%) at 900 ºC for 1 hour. The heating rate was 5 °C/s. The flow rate of hydrogen gas was 30 L/h. The details of hematite pellets and the HyDR procedures were described elsewhere[6]. Subsequently, ~6 grams of HyDR product were melted in an arc furnace (inner volume of 18 L) with a tungsten electrode under the pure Ar atmosphere for three times. Each melting cycle lasted for 65 seconds. Moreover, hematite pellets (~12 grams) were processed by HPSR in the same arc furnace with a gas mixture of Ar-10%H_2 at a total pressure of 900 mbar, which was operated in 15 cycles. In each cycle, the sample was exposed to an electric arc with hydrogen plasma for one minute. The pellets were simultaneously melted and reduced. After individual cycles, the furnace chamber was replenished with the fresh gas mixture[15].

5.2.2. Microstructural characterization

Disc-shaped specimens with a thickness of 1.0-1.5 mm were sliced from the middle of the produced iron using a diamond wire saw. The surfaces were ground with SiC papers down to 4000 grit. Subsequently, the surfaces were polished using diamond suspensions with a particle size of 3 μm and 1 μm, followed by final polishing using colloidal silica suspension (OPS). The microstructure of samples was characterized using a Zeiss Merlin scanning electron microscope (SEM). The 2D porosity analysis of the HyDR sample was performed on 15 SE images using ImageJ software for statistics. The elemental distribution was probed by energy-dispersive X-ray spectroscopy (EDX). In addition, electron backscatter diffraction (EBSD) was conducted to

characterize the crystallographic information (*e.g.*, grain size and types of grain boundaries). The step size of the EBSD measurement was 100 nm and the EBSD data were analyzed using the software OIM Analysis^{TM} V8.6. Further, X-ray diffraction (XRD) analysis was employed to identify the phases using Seifert Theta/Theta diffractometer equipped with cobalt K_{α} radiation. The phase fractions were quantified by the Rietveld refinement method using the Material Analysis Using Diffraction (MAUD) software[98].

5.2.3. Thermal desorption spectroscopy (TDS)

To quantify hydrogen content and to investigate hydrogen trapping behavior in different samples, TDS measurements were conducted using G4 Pheonix DH equipment (Bruker Co.). The samples were heated up to 800 °C using an infrared furnace with either three constant heating rates (*i.e.,* 800, 1000, and 1200 °C/h) or a rapid heating procedure (within 1 min). A mass spectrometer precisely recorded the current flow of desorbed hydrogen, and the integration of this current flow yielded the total hydrogen content. The gap between the sample preparation and the measurement of hydrogen content was about two to four weeks. This period concurs with the shipment or storage durations of the semi-products (here, sponge iron) usually for downstream processing.

5.3. Results

5.3.1. Microstructure of sponge iron produced by hydrogen-based direct reduction

The HyDR on commercial direct-reduction hematite pellets was conducted at 900 °C under a pure hydrogen atmosphere using a thermogravimetry setup. After isothermal holding at this temperature for approximately 690 seconds, the reduction degree reached ~99%, suggesting completion of reduction, **Fig. 30**a. The XRD result confirmed that the HyDR product consisted of mainly α-Fe and a minor trace of magnetite (~1.5 wt.%), **Fig. 30**b. The typical microstructure of the HyDR product is shown in **Fig. 30**c. It revealed a porous structure, with a porosity of 45.0±4.0%. The average size of the micro-pores was 2.97±1.94 μm, and some nano-pores were also observed with an average size of 269±167 nm (**Fig. 30**h**)**. These acquired pores evolved during reduction due to the net volume loss caused by the removal of oxygen. Thus, the HyDR product is also called sponge iron. The elemental maps probed by energy-dispersive X-ray spectroscopy (*e.g.*, Si, Al, Ca, and Mg in **Fig. 30**d-g, respectively) revealed the inherited gangue inclusions and their

heterogeneous distribution in the HyDR product. Due to the thermodynamic constraints, *i.e.*, their higher affinity to oxygen (compared with hydrogen and iron)[153], these elements were hardly reduced and remained as complex oxide compounds[154]. The grain size of the reduced sponge iron was in a wide range of 0.02-30.50 μm^2, as quantified using electron backscatter diffraction (see Appendix **Fig.A** *4*a, **4**b). Low-angle grain boundaries (rotation angle <15º, composed of dislocation arrays) constituted the major type of planar defects with an area density of 0.61 $\mu m/\mu m^2$, while the density of high-angle grain boundaries (rotation angle >15º) was 0.19 $\mu m/\mu m^2$ (see Appendix **Fig.A** *4*c). Several high-angle grain boundaries are exemplarily shown in **Fig. 30**i. No dislocations were observed within the grain interior (**Fig. 30**i). All these observed microstructure defects, *e.g.*, pores[155], residual magnetite[156], gangue oxides[157, 158], high-angle grain boundaries[159-161], dislocations in low-angle grain boundaries[161], *etc.*, could potentially trap hydrogen in the HyDR iron. After melting the sponge iron in an arc furnace, the solidified iron became compact (Appendix **Fig.A** *5*a). Some gangue inclusions (mainly SiO_2) with spherical morphology remained after melting, homogeneously distributed in the solidified iron. The HPSR product revealed a similar microstructure to the melted sponge iron (Appendix **Fig.A 5**b).

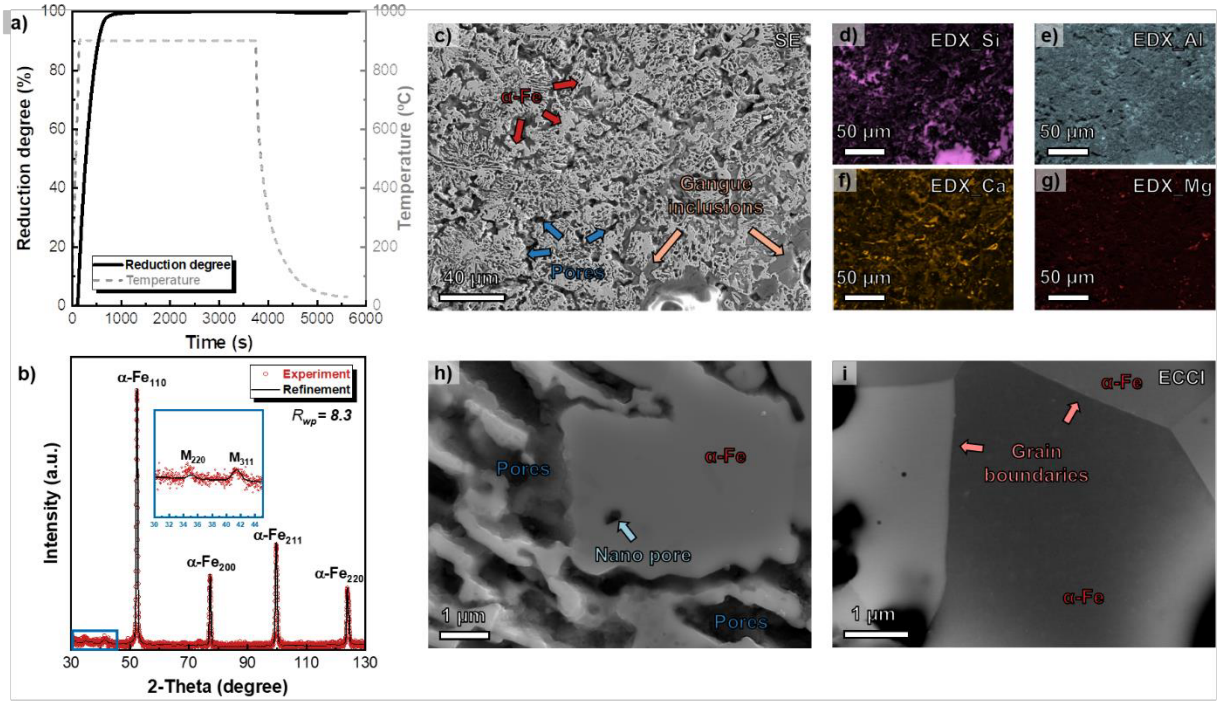

Fig. 30. a) Reduction degree of hydrogen-based direct reduction (HyDR) of a hematite pellet at 900 °C. **b)** Phase identification from X-ray diffraction of the HyDR product (M stands for magnetite). **c)** Secondary electron (SE) image of characteristic microstructure of reduced sponge iron. **d-g)** Corresponding elemental maps of Si, Al, Ca, and Mg of (**c**) probed by energy-dispersive X-ray spectroscopy (EDX). **h)** SE image highlighting a nano-pore. **i)** Electron channeling contrast imaging (ECCI) showing high-angle grain boundaries.

5.3.2. Hydrogen trapping sites in reduced iron

Fig. 31a shows the hydrogen desorption spectra of the samples during continuous heating at a ramping rate of 800 °C/h. The HyDR product in its as-reduced solid state possessed the highest amount of hydrogen compared with the same sample after melting (HyDR+melt) and the HPSR product, as shown by the largest area below its desorption spectrum. By integrating the spectrum, the average hydrogen content in the HyDR product was evaluated to be 39.90±9.00 wppm (**Fig. 31**b). The measurement results from both ramping (solid square) and rapid heating (open circle) tests were in good agreement. To identify the hydrogen trapping sites, the hydrogen desorption spectra were deconvoluted into four peaks, as shown in **Fig. 31**d for the ramping rate of 1000 °C/h. The activation energies of the individual peaks were determined to be 4.32±0.31, 15.15±4.10, 59.14±20.13, and 126.07±7.04 kJ/mol using the Kissinger method[162] (**Fig. 31**e, details in Appendix 8.2.1.). These values correspond to the theoretically determined activation energies for: (1) hydrogen desorbed from the body-centered cubic iron lattice[163, 164] and hydrogen release

from surface iron hydroxides; (2) high-angle grain boundaries and dislocations (constituting the low-angle grain boundaries)[165, 166]; (3) nano-pore and iron oxide (Fe_3O_4)[158, 167]; and (4) remaining gangue inclusions (*e.g.* SiO_2, Al_2O_3, *etc.*)[158], respectively (see Appendix **Table A** 1). **Fig. 31**f shows the amount of hydrogen at these individual trapping sites. The results confirm that the complex defect substructures of the sponge iron offer multiple types of hydrogen trapping sites, capable of storing high amounts of hydrogen in the as-reduced HyDR solid-state material, namely, about 40 wppm.

When additionally melting the as-reduced HyDR product, its high hydrogen content drastically dropped to 1.46±0.50 wppm (**Fig. 31**b), 96% below its value after the preceding solid-state reduction process. This additional melting step of the iron sponge is meant to mimic the subsequent steelmaking process where the sponge is transformed into a liquid, in an electric arc furnace or in a basic oxygen converter. Such a strong hydrogen removal effect can be attributed to: (1) outgassing of hydrogen from the liquid iron to the argon-filled furnace chamber, where the driving force comes from the difference in hydrogen concentration between liquid iron and the gas phase[168]; (2) removal of the relevant trapping sites of hydrogen during the melting process, such as pores (via liquefaction) and gangue oxides (via slag formation). The same principles also apply to the liquid-state HPSR process, explaining its very low hydrogen content of 0.98±0.50 wppm.

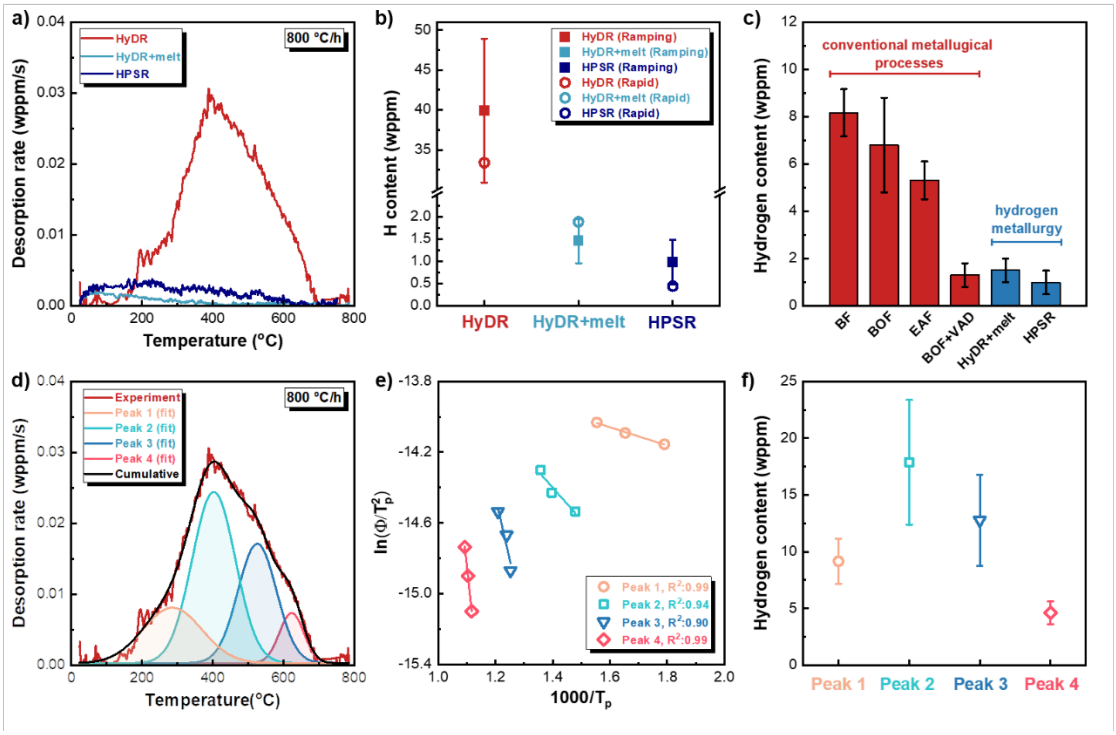

Fig. 31. a) Hydrogen desorption spectra of the HyDR, HyDR+melt, and HPSR samples measured by hot extraction tests with a constant ramping rate of 1000 °C/h. **b)** Average hydrogen content (solid square) from measurements obtained for three constant ramping rates of 800, 1000, and 1200 °C/h. These values are denoted as 'Ramping'. The corresponding error bars represent the standard deviation from the three measurements. The figure shows for reference also the hydrogen content measured by rapid heating to 800 °C at a heating rate of ~800 °C/min (open circle), followed by isothermal holding for 15 mins. This value is denoted as 'Rapid'. **c)** Comparison of the hydrogen contents along the conventional metallurgical (BF stands for blast furnace, BOF for basic oxygen furnace, EAF for electric arc furnace, VAD for vacuum arc degassing) and hydrogen-based metallurgical processes. **d**) Deconvolution of hydrogen desorption spectrum of the HyDR product. **e)** Kissinger plots for the four deconvoluted peaks at ramping rates of 800, 1000, and 1200 °C/h, where T_p stands for the peak temperature of the deconvoluted peaks and Φ for the ramping rate. Details for the Kissinger method are in the Appendix 8.2.1. **f)** Hydrogen contents corresponding to the four deconvoluted peaks.

5.4. Discussion

During conventional metallurgical processes, hydrogen uptake from slag formers, air humidity, steel scrap, *etc*. can occur[168, 169]. Its average content in hot metal ranges from 5-8 wppm processed through the blast furnace (BF), basic oxygen furnace (BOF), and electric arc furnace routes[170, 171], which are the standard processes today. When deploying a subsequent vacuum degassing step, the hydrogen content can be reduced even further to 1-2 wppm[168]. As demonstrated in this study, green steel produced via hydrogen-based metallurgical reduction processes contains only 1-2 wppm hydrogen in its final liquid form, prior to its delivery to customers. This is a similar (low) level as steels processed via the currently most advanced (and expensive) vacuum degassing technology. Thus, the results suggest that using hydrogen in green

steel production is not creating any threat of hydrogen embrittlement. However, hydrogen uptake in green steel can also occur in certain downstream processing and/or in application environments, much like for any steel produced via the conventional BF-BOF route. This can happen for instance during pickling and galvanizing[172], storage and transport, when steel products are exposed to hydrogen-rich corrosive environments[172-175]. Yet, such downstream hydrogen uptake, which may in certain cases lead to hydrogen embrittlement in high-strength steels, is independent of the origin of the production of the raw material (conventional fossil fuel or green hydrogen as reductants). In either case, protective coatings and adequate microstructure design can be effective measures to improve the steels' resistance to hydrogen embrittlement [142, 176].

In summary, we applied thermal desorption spectroscopy to evaluate the hydrogen content in virgin iron produced via two hydrogen-based ironmaking processes, namely, HyDR (solid-state reduction) and HPSR (liquid-state reduction). The complex defect structures in the HyDR sponge iron product trapped high amounts of hydrogen (~40 wppm). This high hydrogen content was drastically reduced by subsequent melting in an arc furnace, mainly through a degassing mechanism, to a level of 1-2 wppm. The HPSR product contained a very low hydrogen content of 0.98±0.50 wppm immediately after the plasma smelting reduction. Compared with the steel produced via conventional processes followed by vacuum treatment (with a hydrogen content of 1-2 wppm), green steel produced via hydrogen-based ironmaking processes can reach a similar level of hydrogen. Thus, using hydrogen as a reductant for future sustainable steel production is not expected to be a cause of hydrogen embrittlement.

6. CONCLUSION

This dissertation highlights the critical role of H_2 gas pressure on the reduction kinetics and microstructural evolution of porous polycrystalline hematite during hydrogen-based direct reduction of hematite. In addition, we analyzed the retained hydrogen content in virgin iron produced through two distinct H_2-based ironmaking methods: Hydrogen-based direct reduction (HyDR) and hydrogen-based plasma smelting reduction (HyPSR), as well as the possible hydrogen trapping sites in direct reduced iron. The main conclusions are summarized as follows:

Influence of H_2 gas pressure on reduction kinetics of hematite pellet under static and dynamic conditions:

- The hematite pellets exhibited increasing reduction kinetics with an increase in H_2 pressure under both static gas exposure conditions (1, 10, and 100 bar) and dynamic gas exposure conditions (1.3 and 50 bar). The enhanced reaction rate with higher H_2 gas pressure is attributed to the increase of H_2 partial pressure in the reducing gas (mixture of H_2 and H_2O). Higher H_2 partial pressure increases the thermodynamic driving force and accelerates the rate of oxygen removal, resulting in enhanced reaction rates on the reaction.

Influence of H_2 gas pressure on microstructural evolution of hematite pellet under static and dynamic conditions:

- Under static conditions, hematite pellets reduced (industrial hematite pellets with 10-13 mm in diameter) at 1 bar and 10 bar exhibited dense iron formation on the wüstite surface as a consequence of sluggish reaction kinetics at low partial pressure of H_2. The faster diffusion rate of iron than the rate of oxygen removal results in the formation of dense iron morphology on the wüstite surface.
- In contrast, elevated H_2 pressure resulted in faster oxygen removal (than at 1 bar and 10 bar) compared to the unchanged iron diffusion (at 700 °C) from the reaction interface towards the iron nuclei favors the formation of porous iron structures.
- Under both dynamic and static conditions, the pore morphology changed from long-elongated pores at ambient H_2 gas pressures to fine-random-shaped pores at elevated H_2 gas pressures. The formation of elongated pore structure is attributed to the presence of instabilities (*i.e.,* distortions on the wüstite surface at the atomic/molecular level) and its

growth during reduction. At elevated hydrogen pressures, a high density of iron nucleation sites leads to the creation of numerous pores with smaller radii.

Green ironmaking under high H2 pressure: Resolving individual reaction steps via in-situ synchrotron high-energy X-ray diffraction:

- Elevated H_2 pressure lowered the onset temperatures of all reduction steps, indicating that higher pressures provide more favorable thermodynamic conditions for the reactions to initiate at lower temperature.
- At 1, 10, and 50 bar H_2 gas pressures, the reactions proceeded in a sequential manner (*i.e.,* hematite was first fully reduced to magnetite, then magnetite to wüstite transformation started, and α-Fe appeared when all almost magnetite was consumed), while at 100 bar, heterogeneous behavior was observed. This is attributed to the highly reactive environment at 100 bar, whereas the elevated chemical potential of H_2 creates a strong thermodynamic driving force for α-Fe formation.
- Overall reduction kinetics improved markedly with increasing H_2 pressure. The reaction rates of all individual steps (*i.e.,* hematite to magnetite, magnetite to wüstite, and wüstite to α-iron) were accelerated. For instance, the rate of α-iron formation at 100 bar was approximately 6.5 times faster than at 1 bar. This step is the most sluggish step under ambient pressure conditions, but, exhibited much faster kinetics at elevated H_2 gas pressures. The pressure effect became particularly pronounced at 50 and 100 bar, where reaction rate enhancement was substantial.
- The wüstite to α-iron reduction was identified as the rate-limiting step under all studied H_2 pressures. Kinetic analyses and microstructural observations confirmed that this step follows a phase-boundary-controlled (PB) mechanism at 1, 10, and 50 bar H_2. Increasing the H_2 pressure significantly enhanced both the thermodynamic driving force and the kinetics of this transformation by accelerating the advancement rate of the wüstite–iron interface.

Influence of H_2 gas pressure on microstructural evolution of cuboidal hematite samples under static conditions, HEXRD study:

- Similar to the microstructural changes observed in hematite pellets with increasing H_2 pressure, the pore morphology transitioned from elongated structures at ambient pressure to fine, random structures at elevated pressures. This transition is attributed to a shift in the balance between vacancy diffusion and interface mobility. At low H_2 pressure, faster vacancy diffusion toward the advancing interface led to the formation of elongated pores, whereas at high pressure, the accelerated interface advancement outpaced vacancy mobility, resulting in equiaxed pores.

Analysis of hydrogen content in green steel:

- As measured by TDS, the iron reduced via HyDR at 900 °C contained 39.90±9.00 wppm hydrogen, and it was significantly removed by the subsequent melting in the arc furnace to 1.46±0.50 wppm, *i.e.*, ~95% hydrogen removal. The iron produced via HyPSR possessed a low hydrogen content of 0.98±0.50 wppm. The HET results concurred well with the TDS measurements.
- The possible hydrogen trapping sites in the iron produced via HyDR were determined based on the associated activation energy of hydrogen desorption, including iron lattice (E_a: 4.32±0.31 kJ/mol), grain boundary and dislocations (E_a: 15.15±4.10 kJ/mol), nanopore and Fe_3O_4 (E_a: 59.14±20.13 kJ/mol) and gangue inclusions (E_a: 126.07±7.04 kJ/mol). Among these trapping sites, grain boundary and dislocations trapped the highest amount of hydrogen of 14.78 wppm, followed by nanopore and Fe_3O_4 (11.33 wppm), lattice (9.17 wppm), and gangue inclusions (4.60 wppm).
- Compared with the hydrogen content in iron and steel produced via conventional processes and followed by vacuum arc degassing (1-2 wppm), the amount of hydrogen in the iron produced via the hydrogen-based ironmaking process is at a similar level. Thus, using hydrogen as a reductant in green steel production is not expected to be a key cause of hydrogen embrittlement.

7. OUTLOOK AND FUTURE WORK

The findings of this dissertation provide valuable insights into the role of H_2 gas pressure on the reduction behavior and microstructural evolution of commercial hematite pellets and final product quality in terms of the risk of hydrogen embrittlement. However, the research scope is primarily confined to a specific set of reduction parameters, leaving several broader questions open for exploration. Some examples are given below.

7.1. Preliminary insights into the effects of impurities on iron oxide reduction

The increasing demand for iron in the steel industry, combined with the decrease in the availability of high-grade iron ores, has made it essential to develop alternative methods for extracting iron from low-grade ores. Low-grade iron ores typically contain high concentrations of alumina and silica as gangue oxides. Commercial hematite pellets contain gangue elements and oxides, including SiO_2 (1.0 to 6.2 wt.%), CaO(0.1 to 2.4 wt.%), MgO (0.2 to 2.6 wt.%), Al_2O_3 (0.2 to 2.7 wt.%), etc. The role of impurities in the iron oxide feedstock is a critical area for further investigation, particularly in the context of HyDR, a solid-state reduction process. The reaction kinetics in HyDR are significantly influenced by the impurities present in commercial hematite pellets, such as MgO and Al_2O_3. These impurities can impact the solid-state reduction process in several ways:

- Dissolution in Iron Oxide Phases: Impurities can dissolve into individual iron oxide phases, including hematite, magnetite, and wüstite, altering their chemical and physical properties, *i.e.,* decreasing cation ion vacancy in oxide [177], and subsequently slowing down the reaction rate [78].
- Segregation at Phase Boundaries: Due to varying solubility levels, impurities can segregate at the boundaries between different iron oxide phases, affecting the structural integrity and reaction pathways [33].
- Formation of Iron-Containing Phases: Impurities may combine with iron to form secondary phases, which can reduce the degree of metallization and hinder the efficiency of the reduction process [178].

Understanding these effects is crucial for optimizing the feedstock composition and enhancing the efficiency of HyDR.

The presence of impurities influences the kinetics of solid-gas reactions and the microstructural evolution of the iron ore [33, 179]. Among these, Al_2O_3 has a particularly strong impact on the reduction behavior and microstructural changes in hematite pellets. Fig. 32. reveals the preliminary results of the influence of Al_2O_3 on the reduction kinetics of magnetite. Preliminary findings indicate that the addition of 1–3 wt.% Al_2O_3 in magnetite decreases the incubation time required to initiate reduction of magnetite, Fig. 32b, likely due to its catalytic effect on H_2 dissociation and its facilitation of exchange of Al^{3+} cation with Fe^{3+} cation within the magnetite matrix. This exchange promotes the counter-diffusion of Fe^{3+} cations from magnetite to wüstite, stabilizing the wüstite phase due to the negligible solubility of Al_2O_3 in wüstite compared to approximately 18 wt.% in magnetite at 700 °C [33]. However, higher concentrations of Al_2O_3 (*e.g.,* 6 wt.%) adversely affect the reduction process. For instance, the degree of reduction is 6 wt.% Al_2O_3 containing sample reached only 0.33 reduction degree after 1 hour of reduction. Literature suggests this sluggish reaction rate is due to the formation of hercynite reaching Fe_3O_4-$FeAl_2O_4$ solid solution, which reduces the thermodynamic driving force for the magnetite-to-wüstite reduction [180].

Further research into gangue elements and their combined effects on reduction behavior is crucial for developing more robust and efficient reduction strategies. Specifically, understanding the role of Al_2O_3 in reduction kinetics and the microstructural evolution of iron ore is vital for optimizing ore preparation (separation of gangue phases with beneficiation approaches, *e.g.,* classification, gravity concentration, magnetic separation, and flotation). Future studies will focus on the catalytic effects of Al_2O_3, its impact on the microstructural evolution of magnetite, and atomic-scale investigations into the partitioning of aluminum within the iron oxide matrix.

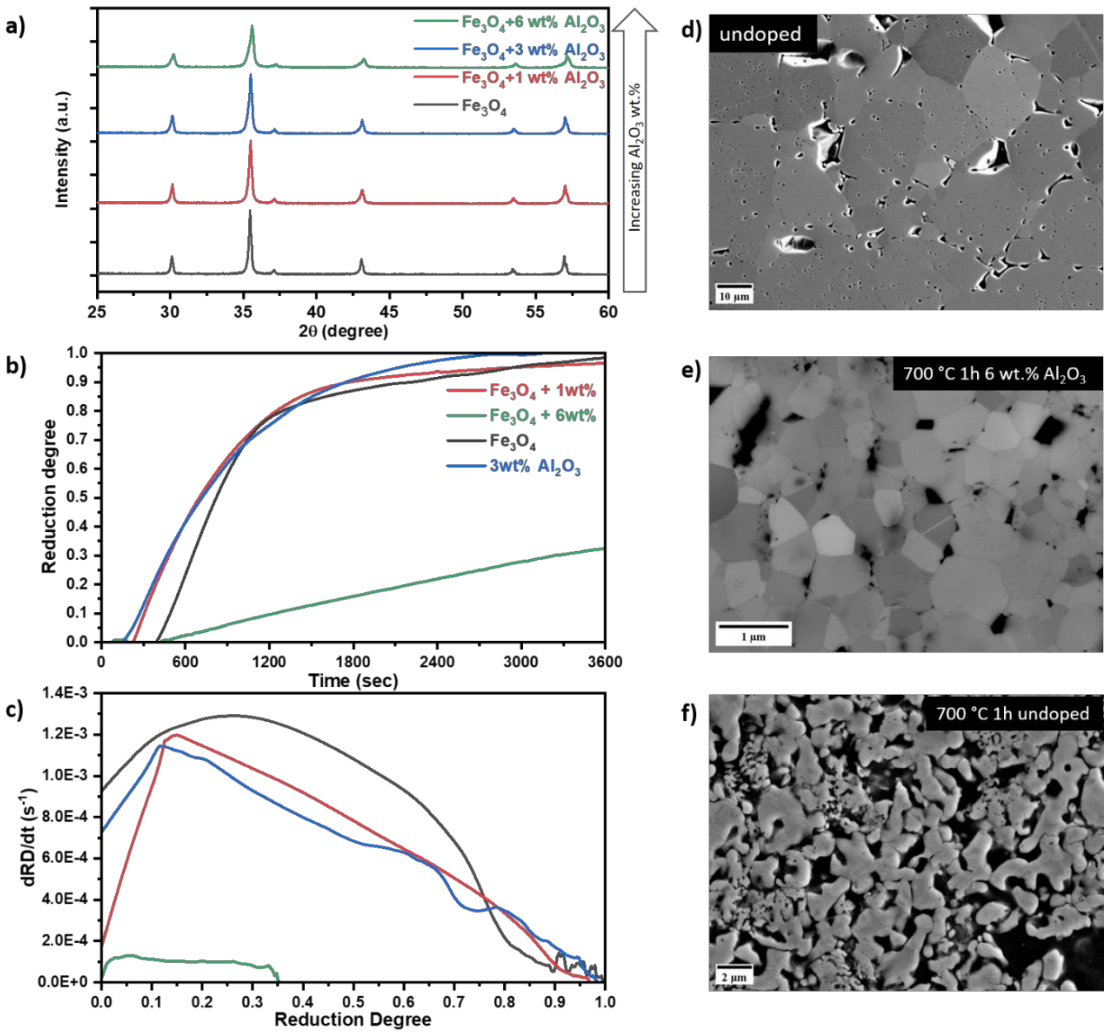

Fig. 32. Preliminary results of the influence of alumina on the reaction kinetics of magnetite with H_2. (a) XRD of magnetite and, 1, 3, and 3 wt% alumina doped samples after spark plasma sintering. (b) The reduction degree versus time curves of samples reduced at 700 C for 1h under 10 L_s/min H_2 gas flow. (c) the reduction rate versus reduction degree curve of samples (d) The microstructure of undoped magnetite after spark plasma sintering. (e) The microstructure of 6wt% AL2O3 added magnetite after 1 h reduction. (f) microstructure of reduced undoped magnetite after reduction.

7.2. Understanding the reduction of wüstite into iron

Wüstite, often represented by its stoichiometric composition as FeO, exhibits an iron-deficient structure under pressures below 10 GPa. It is more accurately described as $Fe_{1-x}O$, where $0.8 \leq 1-x \leq 0.95$. This iron deficiency is accompanied by cation vacancies that balance the stoichiometry. Under reductive atmospheres, the stoichiometry of wüstite is influenced by the partial pressures of H_2 and H_2O. Higher partial pressures of H_2 increase the stoichiometry, moving wüstite closer to its ideal FeO composition.

During the reduction of wüstite to α-Fe, it naturally transitions toward a more stoichiometric structure. This shift is driven by the diffusion of iron cations within the bulk wüstite, which occurs due to a concentration gradient formed between the wüstite surface and its bulk as oxygen is removed. This gradient acts as a driving force, redistributing iron cations throughout the material. The diffusion process not only promotes a more uniform and stoichiometric wüstite structure but also facilitates the subsequent transformation into α-Fe under reducing conditions. The reduction of wüstite to α-Fe is the most sluggish step of the HyDR of iron ore. While existing literature indicates that the reduction behavior of wüstite is influenced by its stoichiometry [62], the specific effects remain poorly understood. Key questions that require further investigation include:

- How does wüstite stoichiometry impact reduction kinetics?
- Can wüstite stoichiometry be optimized through gas composition adjustments to enhance reaction kinetics?
- What role does wüstite stoichiometry play in the evolution of pores during reduction?

8. Appendix

8.1. Green Ironmaking Under High H_2 Pressure Resolving Individual Reaction Steps via In-Situ Synchrotron High-Energy Diffraction

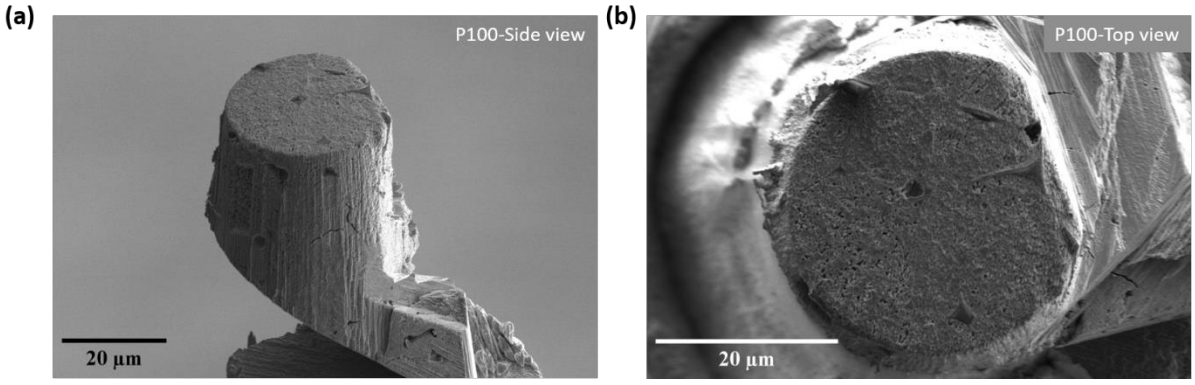

Fig.A 1.SE image of P100 sample prepared using focused ion beam in an FEI Helios dual-beam system with a Xe plasma source. a) Side view b) Top view.

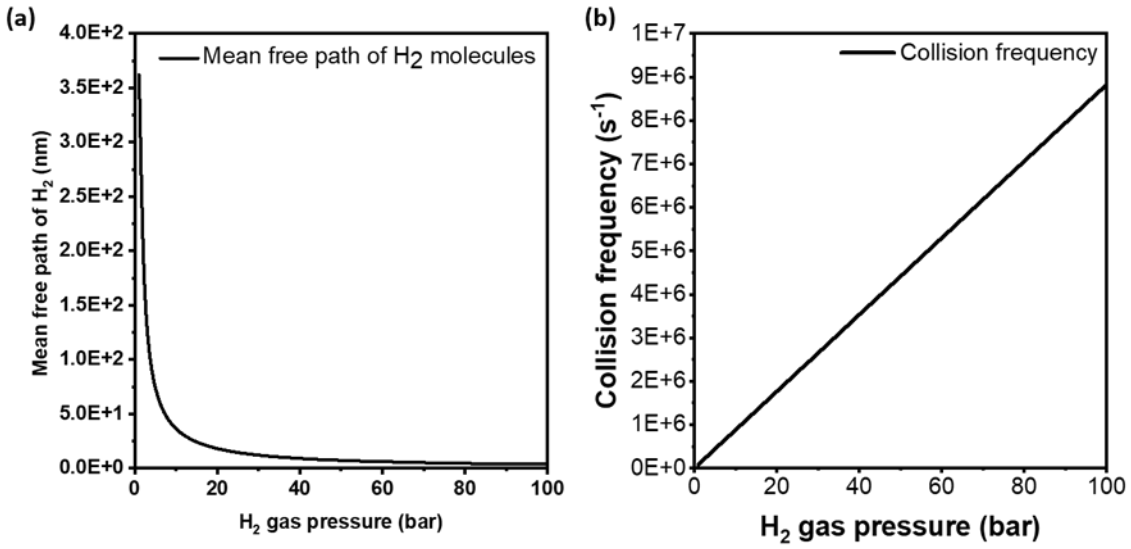

Fig.A 2. The change of gas molecules (a) mean free path and (b) collision frequency as a function of H_2 gas pressure

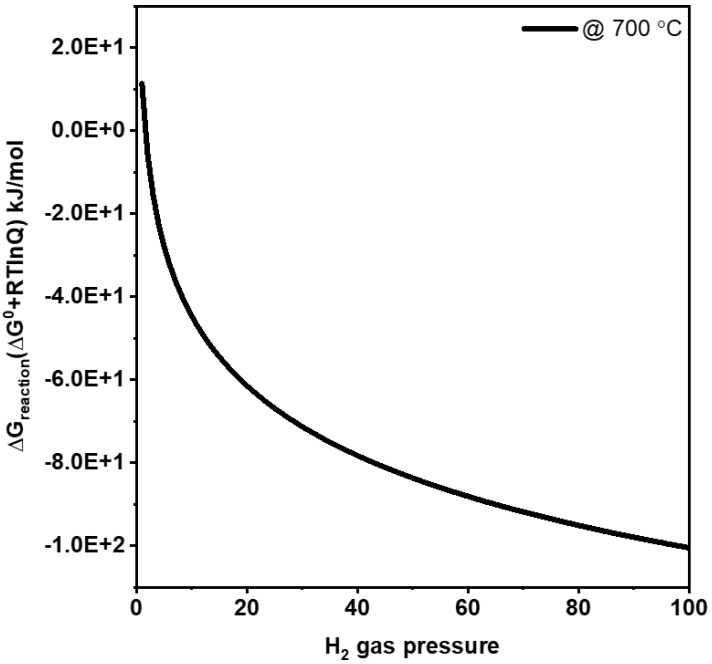

Fig.A 3 Gibbs free energy change (ΔG) for the reduction of 1 g hematite by H_2 at 700 °C, calculated for a 30 L reaction volume under varying H_2 gas pressures. Calculation of Gibbs free energy is done using Eq. (S11). ΔG values are computed using Eq. (S11).

8.1.1. Reduction degree calculations

The overall reduction degree of each sample was calculated based on the conservation of iron moles during reduction, as no iron is lost from the system. Initially, the total number of moles of iron was determined from the sample mass and the stoichiometry of hematite (Eq. 1). At a given reduction stage, the sample consisted of a mixture of hematite, magnetite, wüstite, and α-iron, with their weight fractions obtained from in situ HEXRD measurements. These weight fractions were converted to moles of each phase, and the corresponding moles of iron were calculated based on the stoichiometric Fe content in each phase's chemical formula (Eq. 2). By maintaining the conservation of total iron moles before and after reduction, the mass of the reduced sample was determined from the phase composition. The reduction degree was then computed as the ratio of the actual oxygen-related mass loss to the theoretical maximum mass loss if complete reduction to metallic iron were achieved, as explained below.

Fe(wt%) in Fe, FeO, Fe_3O_4, Fe_2O_3 phases: known from *in-situ* HEXRD experiments

Molecular masses of phases:

- Fe = 55.85 g/mol
- FeO = 71.84 g/mol
- Fe_3O_4 = 231.53 g/mol
- Fe_2O_3 = 159.69 g/mol

The Fe content in remaining oxides must match the theoretical Fe from the initial hematite.

At initial time ($t=t_0$):

Assume the material is all hematite with initial mass of $M^H = a$ g, then the mol of Fe in hematite is given by Eq. (A1);

$$n_{Fe}^{H}(\text{Fe mol in hematite}) = 2 \times \frac{a}{160}\ \text{mol} \qquad \text{(A1)}$$

At time $t=t_1$ (instant state):

Mass of reduced sample at $t=t_1$ is b g, given by;

$$\mathrm{b} = n_{Fe}^{t_0} \times (\sum \frac{w_i}{M_i} \times z_{Fe,i})^{-1} \quad \text{(A2)}$$

where; a, $n_{Fe}^{t_0}$, w_i, M_i and $z_{Fe,i}$ are initial sample mass (hematite), total number of moles of iron (constant from hematite), weight fraction of phase i (hematite, magnetite, wüstite and α-iron), and number of iron atoms per formula unit of phase i (*e.g.,* 2 for hematite).

The reduction degree of hematite was subsequently calculated using Eq. (A3);

$$\mathrm{RD\%} = \frac{a - b}{0.3 \times a} \times 100 \quad \text{(A3)}$$

Where a, b, and $0.3a$, are initial mass, mass at time t, and theoretical oxygen content in hematite, respectively.

8.1.2. Thiele modulus calculations [95]

The Thiele modulus, a dimensionless number, is calculated to characterize the relationship between the redox reaction of H_2 with hematite and the diffusion rate of H_2 gas molecules within the porous hematite sample using Eq. (S4).

$$\Phi^2 = \frac{k_3 r_p}{D_{eff}} \quad \text{(A4)}$$

k_3: The rate constant for the reduction from wüstite to α-iron

r_p : The half-length of the specimen

D_{eff} : Effective diffusivity of H_2

The following Eq.s (A5) to (A9) are used to calculate D_{eff}.

$$D_{eff,\,H_2} = \varepsilon^2 D_{H_2}\ (\mathrm{m^2/s}) \quad \text{(A5)}$$

$$D_{H_2} = \frac{1}{\frac{1}{D_{H_2}^m}} + \frac{1}{\frac{1}{D_{H_2}^k}}\ (\mathrm{m^2/s}) \quad \text{(A6)}$$

$$D_{H_2}^m = (1 - y_{H_2})(\Sigma_{H_2 \neq H_2O} \frac{y_{H_2O}}{D_{H_2,H_2O}})^{-1} (\mathrm{m^2/s}) \quad \text{(A7)}$$

$$D_{H_2}^k = \frac{4K_0}{3} \sqrt{\frac{8RT}{\pi M_{H_2}}}\ (\mathrm{m^2/s}) \quad \text{(A8)}$$

$$D_{H_2,H_2O} = \frac{10^{-7} T^{1,75} (\frac{1}{M_{H_2}} + \frac{1}{M_{H_2O}})^{1/2}}{P[(\Sigma_{H_2} \sigma_{H_2})^{\frac{1}{3}} + (\Sigma_{H_2O} \sigma_{H_2O})^{\frac{1}{3}}]}\ (\mathrm{m^2/s}) \quad \text{(A9)}$$

$D_{eff,\,H_2}$: Effective diffusivity of H_2 in porous medium ($\mathrm{m^2/s}$)

ε: Sample porosity, dimensionless (obtained from nanoCT experiments)

D_{H_2}: Effective intraparticle diffusivity of H_2 (m^2/s)

$D_{H_2}^m$: Molecular diffusivity of H_2 (m^2/s)

$D_{H_2}^k$: Knudsen diffusivity of H_2 (m^2/s)

M_{H_2,H_2O}: Molecular mass of H_2 and H_2O (g/mol)

σ_{H_2}: Diffusion volume of H_2, 7.07 cm^3/mol

σ_{H_2O}: Diffusion volume of H_2O, 12.7 cm^3/mol

D_{H_2,H_2O}: Mass diffusivity of H_2 through H_2O (cm^2/s) [181]

y_{H_2}: Mole fraction of H_2

y_{H_2O}: Mole fraction of H_2O

8.1.3. Wüstite-Iron interface velocity calculations

α-iron growth across the wüstite surface occurs at a velocity, V_m, and the Gibbs free energy change for the reaction $FeO+H_2 \rightarrow Fe+H_2O$, $\Delta G_{reaction}$, are described by Eq (A10) and (A11) , respectively [28, 125] ;

$$V_m = R_m\left(\frac{b_m}{\rho_m h_m}\right) = \left(\frac{b_m}{\rho_m h_m}\right)\phi_m^1 P_{H_2} \times \left[1 - \exp\left(\frac{\Delta G_{reaction}}{RT}\right)\right] (ms^{-1}) \qquad \text{(A10)}$$

$$\Delta G_{reaction} = \Delta G^0 + RT \ln \frac{(P_{H_2O})^3}{(P_{H_2})^3} \qquad \text{(A11)}$$

The definitions of each symbol are provided in the main text. Here, b_m and h_m are assumed to be 1 μm. The forward reaction rate constant, ϕ_m^1, and standard Gibbs free energy of the reaction, ΔG^0, determined using the FactSage 8.3, reaction module and SGPS(2023) database [182, 183].

8.2. How much hydrogen is in green steel?

This chapter provides supplementary information to Chapter 5. It presents the microstructural features of HyDR and HPRS samples, the deconvolution analysis of TDS plots of HyDR samples, and the methods used to analyze the trapping energy of hydrogen and their possible trapping sites. Furthermore, the hydrogen content measured in the conventional steel production route is presented.

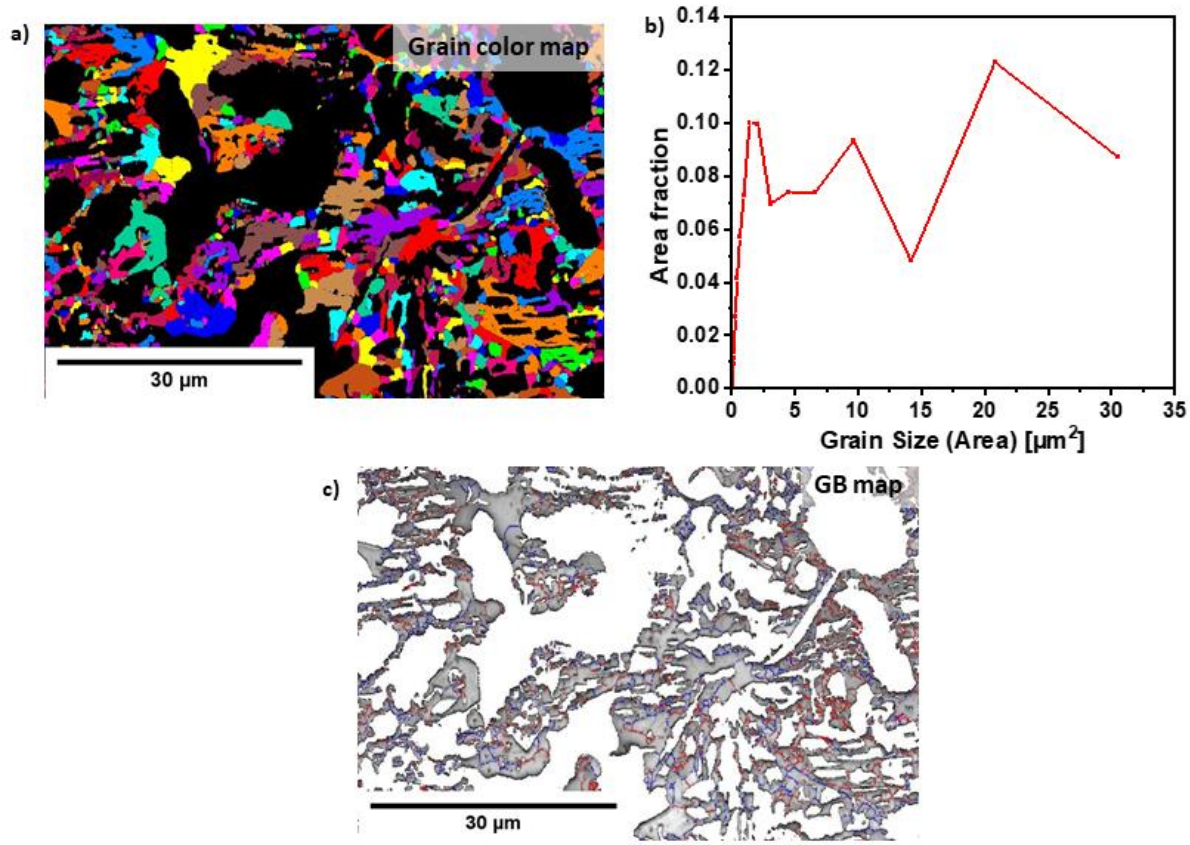

Fig.A 4. Grain color map of the HDR sample probed by electron backscatter diffraction, the black regions represent pores and gangue inclusions; **b,** the size distribution of the iron grains; **c,** and distribution of low-angle and high-angle grain boundaries of iron in HyDR sample, blue lines representing high-angle grain boundaries (>15º) and red lines for low-angle grain boundaries (<15º)

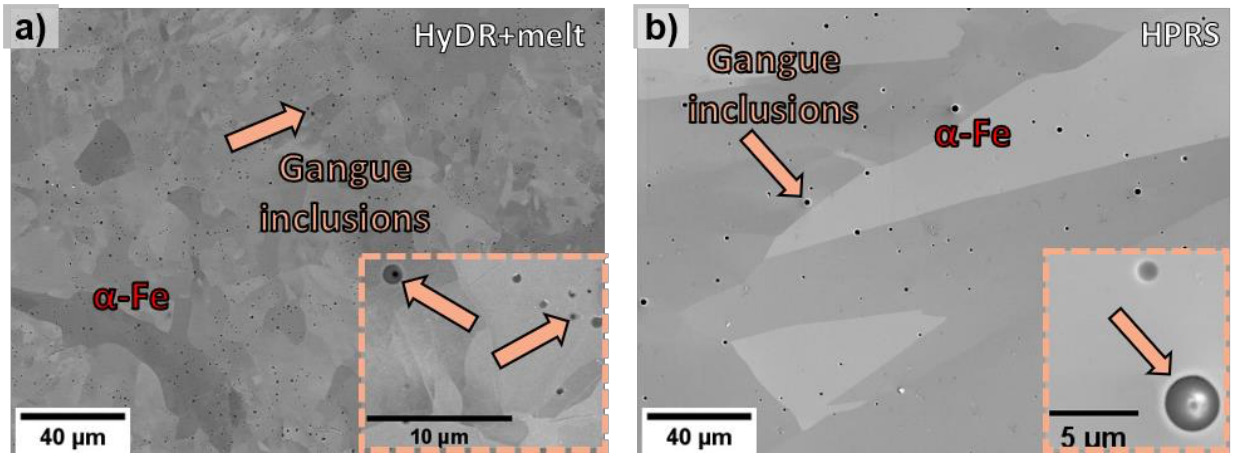

Fig.A 5. a) SE image of HyDR+melt sample; **b)** SE image of HPSR sample.

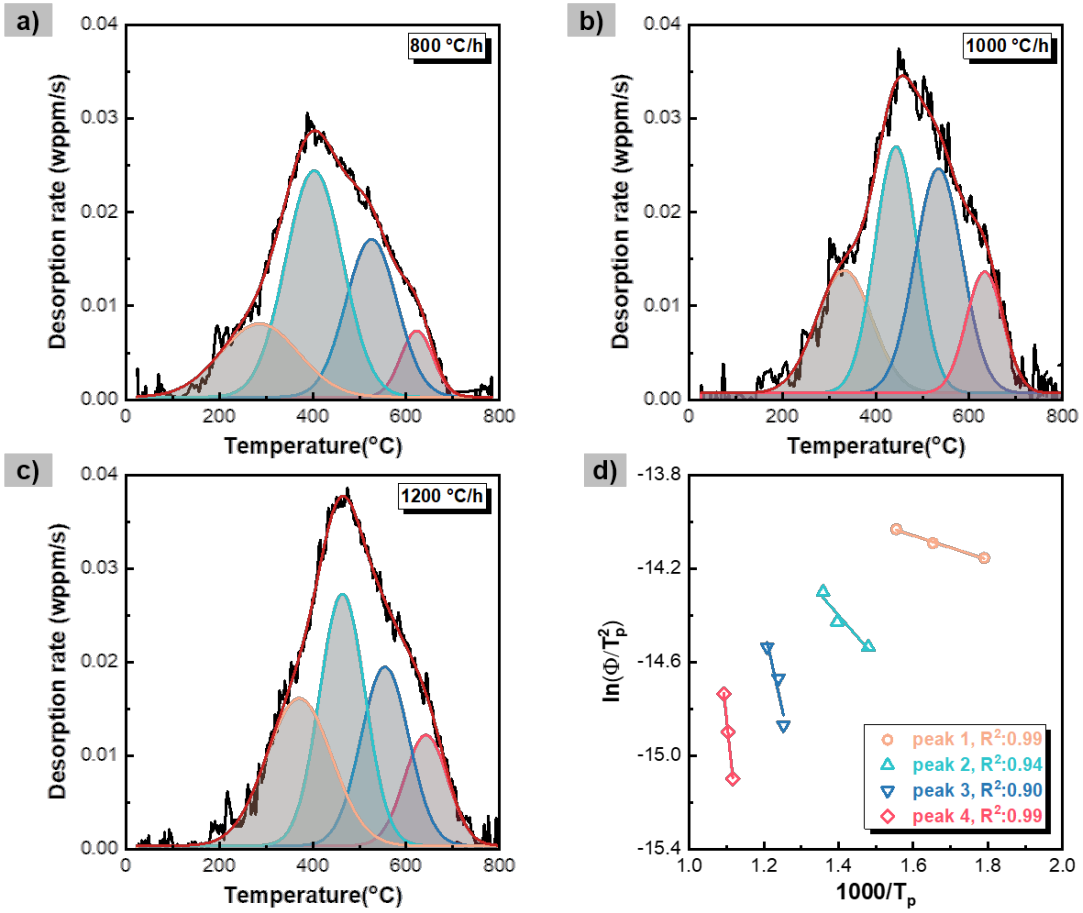

Fig.A 6. Deconvolution of the TDS spectra of HDR sample at different heating rates: **a)**800 ºC/h, **b)** 1000 ºC/h, **c)**1200 ºC/h; **d)** the correlation between $ln\left(\phi/T_p^2\right)$ and 1000/T_p for the calculation of activation energies of hydrogen trapping sites

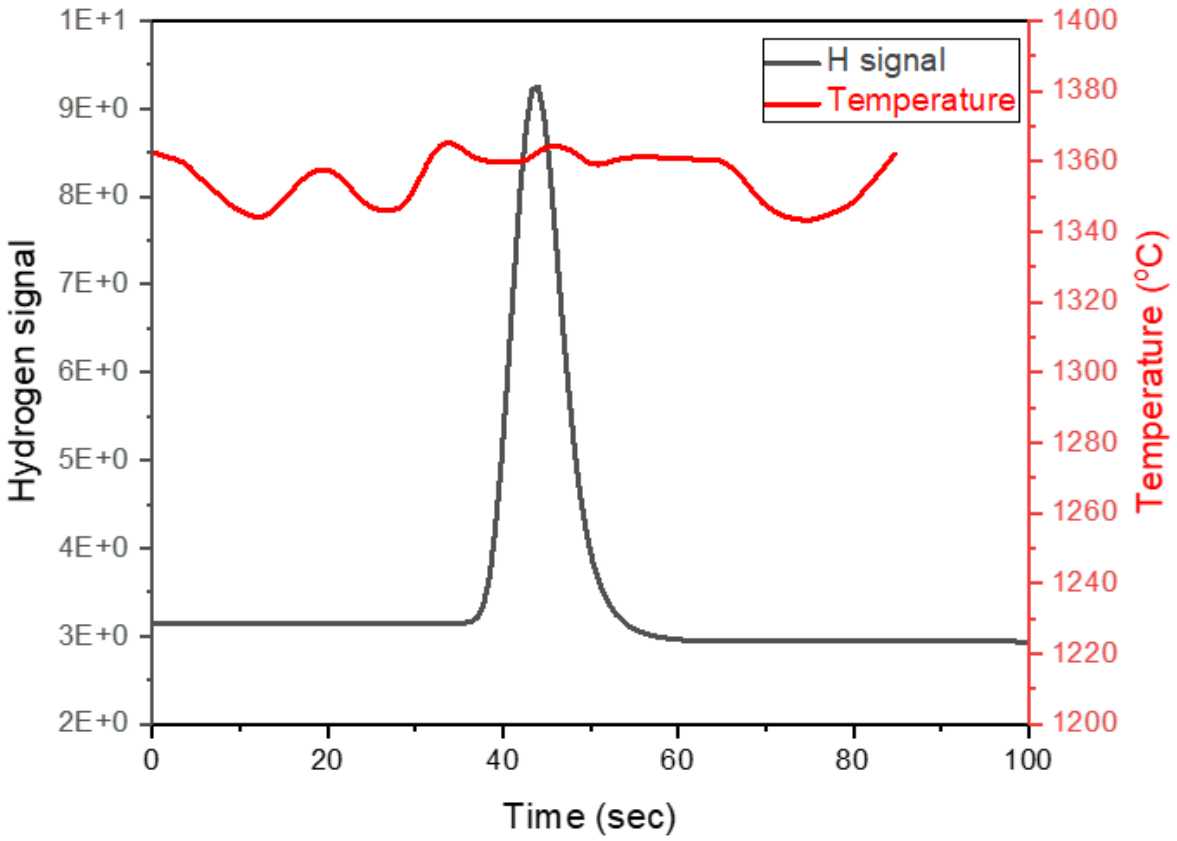

Fig.A 7. The hydrogen signal of the HyDR sample after TDS experiments (after two weeks) obtained from MS detector for rapid heating from room temperature to 1400 ºC (MS stands for mass spectrometer). The integration of the area below the signal curve corresponds to 9.47 wppm of hydrogen.

8.2.1. Method

The trapping energies pertaining to specific trapping sites were further determined using the TDS data. Desorption of hydrogen from its trapping sites is a thermally activated process and the rate of its desorption is formulated by Kissinger´s reaction kinetics in Eq. (A12) [184]:

$$\frac{dx}{dt} = A(1-x)\exp\left\{\frac{-E_a}{RT}\right\} \qquad \text{(A12)}$$

where $x=(N_0-N)/N_0$, x is the hydrogen concentration desorbed from trapping sites, N_o is the hydrogen concentration at t=0, N is the hydrogen concentration at $t\neq0$, A is the reaction constant, E_a is the activation energy for hydrogen desorption, R is the gas constant, and T is the absolute temperature in Kelvin.

A mathematical method proposed by J.Y. Lee and S.M. Lee was used to calculate activation energy for hydrogen desorption from multiple traps based on Kissinger´s reaction kinetics equation [185]. For a constant heating rate, Φ, the first derivative of Eq. A12 is set to zero at the temperature $T_{p,}$ where the hydrogen desorption rate is maximum. The equation is then derived as:

$$\frac{\phi E_a}{RT_p^2} = A \exp\left(\frac{-E_a}{RT_p}\right) \quad \text{(A13)}$$

When the logarithms of both sides of Eq A13 are taken, then differentiated with respect to $1/T_p$, the equation is derived as:

$$\frac{\partial \ln\{\phi/T_p^2\}}{\partial\{1/T_p\}} = \frac{-E_a}{R} \quad \text{(A14)}$$

Here, E_a is deduced from the slope of $ln(\Phi/T_p^2)$ versus $(1/T_p)$ (Figure **3** d) by measuring the T_p of the desorption peak at various heating rates, *i.e.*, 800 (**Fig.A 6**a), 1000 (**Fig.A 6**b) and 1200 ºC (**Fig.A 6**c) [155]. Based on the effect of the heating rate on the peak temperature in TDS measurements, the $ln(\phi/T_p^2)$ against $1000/T_p$ was plotted and activation energies of each peak were calculated by employing Eq. A14.

8.2.2. Discussion

8.2.2.1. Analysis of trapping energies

Hydrogen-based direct reduction HyDR is a complex multistep solid-gas reaction and includes chemical, physical, and mechanical interactions [30, 59]. As a consequence of these complex interactions, direct reduced iron acquires multiple defects such as vacancy, dislocation, grain boundary, porosity, and inclusions [186], which are potential hydrogen trapping sites in the HDR sample [187, 188]. The typical activation energies of hydrogen desorption from these microstructural features in the literature are summarized in **Table A** 1.

Table A 1Summary of the trapping sites of hydrogen in body-centered cubic iron (TDS stands for thermal desorption spectroscopy, EAM for embedded atom model, DFT for density functional theory, IF for internal friction technique)

Trapping sites	The activation energy (kJ/mol)	Method
Lattice diffusion	6.90-7.60 [155, 157, 189]	TDS
	3.85-4.72 [163]	EAM
	4.05 [164]	DFT
Grain boundary	17.20-19.68 [155, 157, 189]	TDS
Dislocation	24.12 [165], 26.80 [155]	TDS
	36.66-46.32 [165]	IF
Nanopore	35.20 [155], 48.30 [167]	TDS
Iron oxide (Fe_2O_3, Fe_3O_4)	50.60-69.50 [158]	TDS
	47.20 [156]	TDS
Gangue inclusion (SiO_2)	112.10 [158]	TDS

The activation energy calculated for the first peak (4.32±0.31 kJ/mol) is close to the reported activation energy of hydrogen desorption from the bcc-iron lattice. However, the period between the sample preparation and the measurement of hydrogen content was two to four weeks, so that, most of the diffusible hydrogen was supposed to diffuse out because of the extremely low solubility of hydrogen in the lattice (~0.002 wppm at room temperature [190]) and high mobility of hydrogen in the bcc-iron (1.0×10^{-4} cm^2/s at room temperature [164]). The hydrogen might be released from the surface iron hydroxides which can be formed during sample preparation (using water during cutting and grinding) and or its storage during shipment (humidity). To verify this statement, the hydrogen content of the HyDR sample after TDS measurement was measured (no trapped hydrogen in the sample) by melting the sample with rapid heating from room temperature to 1400 ºC., and 9.47 wppm of hydrogen was detected. **Fig.A** *7* shows the hydrogen signal curve detected by quadrupole mass spectrometer and internal temperature as a function of time. The integration of the area below hydrogen signal curve represents hydrogen content in the sample, measured as 9.47 wppm.

The second peak associated with the activation energy of 15.15±4.10 kJ/mol designates multiple trapping sites, such as grain boundaries (17.20-19.68 kJ/mol) and dislocations (24.12-26.8 kJ/mol). This fact implies the stored dislocations in the microstructure could trap hydrogen in the HDR sample. As the hematite pellets were exposed to HyDR at 900 ºC, dislocations generated during reduction due to lattice mismatch and local delamination could re-arrange into a special dislocation pattern, *i.e.*, the low-angle grain boundaries, as observed in **Fig.A** *4*c. This type of

boundary is comprised of a periodic dislocation arrangement. The distortion at the cores of these dislocations could be the potential trapping sites for hydrogen.

The calculated activation energy of 59.14±20.13 kJ/mol for the third desorption peak indicates several possible trapping sites as well, such as nanopore and iron oxide (Fe_3O_4). During HyDR, the removal of oxygen atoms from the iron ore lattices results in vacancy formation, which coalesces to form pores [76]. Such pores can act as hydrogen-trapping sites. Moreover, the direct reduced iron is susceptible to surface oxidation due to its large surface area to volume ratio, which can also trap hydrogen when it diffuses through the lattices.

The remaining gangue inclusions (*e.g.* SiO_2, Al_2O_3, *etc.*) serve as deep trapping sites for hydrogen, which revealed the highest activation energy of 126.07±7.04 kJ/mol during the TDS measurements. This value agrees well with the desorption of hydrogen from SiO_2 (*i.e.*, 112.10 kJ/mol).

8.2.2.2. Hydrogen content in steel produced by conventional processes

The hydrogen content of pig iron trapped in a blast furnace is measured as 8±1 wppm via the vacuum heating method [170]. The hydrogen content of the steel produced in the basic oxygen furnace is measured to be ~9 wppm using the HYDRIS method, which can be reduced to 6.8±2.2 wppm by decreasing the basicity of the slag, using low hydrogen petcoke (<1000 wppm), and avoiding the use of aluminum as deoxidizer [191]. The hydrogen content can be further reduced to 1-2 wppm using a vacuum arc degassing treatment, which is a mature technology in the steel industry to remove excess hydrogen from the liquid steel. For the secondary synthesis route through an electric arc furnace, including continuous casting, the hydrogen content is measured to be approximately 5.3±0.8 wppm using the HYDRIS method [171].

List of Figures

List of Tables

References

1. Raabe, D., *The Materials Science behind Sustainable Metals and Alloys.* Chem Rev, 2023. **123**(5): p. 2436-2608.
2. Basson, E., *2023 World Steel in Figures*, W.s. association, Editor. 2023. p. 1-30.
3. Raabe, D., C.C. Tasan, and E.A. Olivetti, *Strategies for improving the sustainability of structural metals.* Nature, 2019. **575**(7781): p. 64-74.
4. Sun, Y., et al., *Decarbonising the iron and steel sector for a 2 C target using inherent waste streams.* Nature communications, 2022. **13**(1): p. 297.
5. Jiang, B., et al., *Carbon carrier modeled for CO2 emission assessment in steel industry.* Sustainable Energy Technologies and Assessments, 2024. **72**: p. 104068.
6. Kim, S.-H., et al., *Influence of microstructure and atomic-scale chemistry on the direct reduction of iron ore with hydrogen at 700°C.* Acta Materialia, 2021. **212**.
7. Hermwille, L., et al., *A climate club to decarbonize the global steel industry.* Nature Climate Change, 2022. **12**(6): p. 494-496.
8. Agreement, P., *UNFCCC, Adoption of the Paris agreement. COP.* 25th session Paris, 2015. **30**: p. 1-25.
9. Wiencke, J., et al., *Electrolysis of iron in a molten oxide electrolyte.* Journal of Applied Electrochemistry, 2018. **48**(1): p. 115-126.
10. Tian, S., et al., *Inherent potential of steelmaking to contribute to decarbonisation targets via industrial carbon capture and storage.* Nat Commun, 2018. **9**(1): p. 4422.
11. Allanore, A., *Features and Challenges of Molten Oxide Electrolytes for Metal Extraction.* Journal of The Electrochemical Society, 2014. **162**(1): p. E13-E22.
12. Cooper, D.R., et al., *Component level strategies for exploiting the lifespan of steel in products.* Resources, Conservation and Recycling, 2014. **84**: p. 24-34.
13. Ohno, H., et al., *Toward the efficient recycling of alloying elements from end of life vehicle steel scrap.* Resources, Conservation and Recycling, 2015. **100**: p. 11-20.
14. Patisson, F., O. Mirgaux, and J.-P. Birat, *Hydrogen steelmaking. Part 1: Physical chemistry and process metallurgy.* Matériaux & Techniques, 2021. **109**(3-4): p. 303.
15. Souza Filho, I.R., et al., *Sustainable steel through hydrogen plasma reduction of iron ore: Process, kinetics, microstructure, chemistry.* Acta Materialia, 2021. **213**.
16. Patisson, F. and O. Mirgaux, *Hydrogen Ironmaking: How It Works.* Metals, 2020. **10**(7).
17. Dutta, S.K. and Y.B. Chokshi, *Basic concepts of Iron and steel making*. 2020: Springer Nature.
18. Mitra, S., et al., *Understanding cohesive zone behaviour of blast furnace based on computed tomography flow modelling in a fused bed of ferrous and coke particles.* Powder Technology, 2024. **439**: p. 119686.
19. Basson, E., *2022 World steel in figures* 2023, World steel association.
20. Midrex Technologies, I., *2023 World Direct Reduction Statics* 2024.
21. Ripke, J. and J. Kopfle, *MIDREX H2: ultimate low CO2 ironmaking and its place in the new hydrogen economy.* Direct from MIDREX, 3rd quarter, 2017: p. 7-12.
22. Moziraji, M.R., et al., *Natural gas as a relatively clean substitute for coal in the MIDREX process for producing direct reduced iron.* Energy for Sustainable Development, 2024. **78**: p. 101356.
23. Ibrahim, A.A., et al., *Methane decomposition over iron catalyst for hydrogen production.* International Journal of Hydrogen Energy, 2015. **40**(24): p. 7593-7600.
24. Souza Filho, I.R., et al., *Fundamentals of Green Steel Production: On the Role of Gas Pressure During Hydrogen Reduction of Iron Ores.* JOM (1989), 2023. **75**(7): p. 2274-2286.

25. Shams, A. and F. Moazeni, *Modeling and Simulation of the MIDREX Shaft Furnace: Reduction, Transition and Cooling Zones.* Jom, 2015. **67**(11): p. 2681-2689.
26. Jiang, X., L. Wang, and F.M. Shen, *Shaft Furnace Direct Reduction Technology - Midrex and Energiron.* Advanced Materials Research, 2013. **805-806**: p. 654-659.
27. Duarte, P. and D. Pauluzzi, *Premium quality DRI products from ENERGIRON.* Techn rep. Energiron, 2019.
28. Hayes, P.C., *Stability criteria for product microstructures formed on gaseous reduction of solid metal oxides.* Metallurgical and Materials Transactions B, 2010. **41**: p. 19-34.
29. Andersson, J.-O., et al., *Thermo-Calc & DICTRA, computational tools for materials science.* Calphad, 2002. **26**(2): p. 273-312.
30. Ma, Y., et al., *Hierarchical nature of hydrogen-based direct reduction of iron oxides.* Scripta Materialia, 2022. **213**.
31. Kitchener, J., et al., *The solubility of oxygen in gamma iron.* Acta Metallurgica, 1953. **1**(1): p. 93-101.
32. Cornell, R.M. and U. Schwertmann, *The iron oxides: structure, properties, reactions, occurrences, and uses*. Vol. 664. 2003: Wiley-vch Weinheim.
33. Kapelyushin, Y., et al., *Formation of a Network Structure in the Gaseous Reduction of Magnetite Doped with Alumina.* Metallurgical and Materials Transactions B, 2017. **48**(2): p. 889-899.
34. Hazen, R.M. and R. Jeanloz, *Wüstite (Fe1-x O): A review of its defect structure and physical properties.* Reviews of Geophysics, 1984. **22**(1): p. 37-46.
35. Spreitzer, D. and J. Schenk, *Reduction of Iron Oxides with Hydrogen—A Review.* steel research international, 2019. **90**(10).
36. van der Eijk, C., H. Dalaker, and J. Safarian, *Possibilities and Limitations of the Use of Hydrogen in Different Metallurgical Sectors.* Materials Proceedings, 2023. **15**(1): p. 63.
37. Liu, F., et al., *Theoretical study of reduction mechanism of Fe2O3 by H2 during chemical looping combustion.* Chinese Journal of Chemical Engineering, 2021. **37**: p. 175-183.
38. Yu, X., X. Zhang, and S. Wang, *High coverage hydrogen adsorption on the Fe3O4(110) surface.* Applied Surface Science, 2015. **353**: p. 973-978.
39. Teplov, O., *Kinetics of the low-temperature hydrogen reduction of magnetite concentrates.* Russian Metallurgy (Metally), 2012. **2012**(1): p. 8-21.
40. El-Geassy, A. and M. Nasr, *Influence of the original structure on the kinetics of hydrogen reduction of hematite compacts.* Transactions of the Iron and Steel Institute of Japan, 1988. **28**(8): p. 650-658.
41. Bahgat, M. and M. Khedr, *Reduction kinetics, magnetic behavior and morphological changes during reduction of magnetite single crystal.* Materials Science and Engineering: B, 2007. **138**(3): p. 251-258.
42. El-Rahaiby, S. and Y. Rao, *The kinetics of reduction of iron oxides at moderate temperatures.* Metallurgical Transactions B, 1979. **10**: p. 257-269.
43. Zuo, H.-b., et al., *Reduction kinetics of iron oxide pellets with H 2 and CO mixtures.* International Journal of Minerals, Metallurgy, and Materials, 2015. **22**: p. 688-696.
44. Kovtun, O., et al., *Results of Hydrogen Reduction of Iron Ore Pellets at Different Temperatures.* steel research international, 2024: p. 2300707.
45. Edstrom, J. and G. Bitsianes, *Solid state diffusion in the reduction of magnetite.* Jom, 1955. **7**: p. 760-765.
46. Heidari, A., et al., *A review on the kinetics of iron ore reduction by hydrogen.* Materials, 2021. **14**(24): p. 7540.

47. Bonalde, A., A. Henriquez, and M. Manrique, *Kinetic analysis of the iron oxide reduction using hydrogen-carbon monoxide mixtures as reducing agent.* ISIJ international, 2005. **45**(9): p. 1255-1260.
48. AA, E. and V. Rajakumar, *Gaseous reduction of wustite with H2, CO and H2-CO mixtures.* Transactions of the Iron and Steel Institute of Japan, 1985. **25**(6): p. 449-458.
49. Ali, M.L., Q. Fradet, and U. Riedel, *Kinetic mechanism development for the direct reduction of single hematite pellets in H2/CO atmospheres.* steel research international, 2022. **93**(12): p. 2200043.
50. Lu, F., et al., *Carbon formation on the surface during the reduction of iron oxide particles by CO and CO/H2 mixtures.* Chemical Engineering Science, 2019. **205**: p. 238-247.
51. SATO, K., Y. NISHIKAWA, and T. GOTO, *Non-isothermal and Non-isobaric Phenomena during the Reduction of a Hematite Sphere with Hydrogen.* Transactions of the Iron and Steel Institute of Japan, 1985. **25**(12): p. 1194-1201.
52. Kawasaki, E., J. Sanscrainte, and T.J. Walsh, *Kinetics of reduction of iron oxide with carbon monoxide and hydrogen.* AIChE Journal, 1962. **8**(1): p. 48-52.
53. Özgün, Ö., et al., *Green Ironmaking at Higher H(2) Pressure: Reduction Kinetics and Microstructure Formation During Hydrogen-Based Direct Reduction of Hematite Pellets.* J Sustain Metall, 2024. **10**(3): p. 1127-1140.
54. TAKAHASHI, R., et al., *Operation and simulation of pressurized shaft furnace for direct reduction.* Transactions of the Iron and Steel Institute of Japan, 1986. **26**(9): p. 765-774.
55. Arno HABERMANN, F.W., Hermann HOFBAUER, Johann ZIRNGAST and Johannes Leopold SCHENK, *An Experimental Study on the Kinetics of Fluidized Bed Iron Ore Reduction.* ISIJ International, 2000. **40**(10): p. 935-942.
56. Cavaliere, P., A. Perrone, and D. Marsano, *Effect of reducing atmosphere on the direct reduction of iron oxides pellets.* Powder Technology, 2023. **426**.
57. SATO, K., et al., *Effect of Pressure on Reduction Rate of Iron Ore with High Pressure Fluidized Bed.* Transactions of the Iron and Steel Institute of Japan, 1986. **26**(8): p. 697-703.
58. Zakeri, A., K.S. Coley, and L. Tafaghodi, *Hydrogen-based direct reduction of iron oxides: a review on the influence of impurities.* Sustainability, 2023. **15**(17): p. 13047.
59. Bai, Y., et al., *Chemo-mechanical phase-field modeling of iron oxide reduction with hydrogen.* Acta Materialia, 2022. **231**.
60. Ünal, A. and A. Bradshaw, *Rate processes and structural changes in gaseous reduction of hematite particles to magnetite.* Metallurgical Transactions B, 1983. **14**: p. 743-752.
61. Zhou, X., et al., *Effect of Pore Formation on Redox-Driven Phase Transformation.* arXiv preprint arXiv:2209.09069, 2022.
62. Matthew, S., T. Cho, and P. Hayes, *Mechanisms of porous iron growth on wustite and magnetite during gaseous reduction.* Metallurgical transactions B, 1990. **21**: p. 733-741.
63. Cabot, A., et al., *Vacancy coalescence during oxidation of iron nanoparticles.* Journal of the American Chemical Society, 2007. **129**(34): p. 10358-10360.
64. Hidayat, T., et al., *On the relationships between the kinetics and mechanisms of gaseous hydrogen reduction of solid nickel oxide.* Metallurgical and Materials Transactions B, 2009. **40**: p. 474-489.
65. Kolluri, K. and M.J. Demkowicz, *Formation, migration, and clustering of delocalized vacancies and interstitials at a solid-state semicoherent interface.* Physical Review B—Condensed Matter and Materials Physics, 2012. **85**(20): p. 205416.
66. Kang, S.-J.L., *Sintering: densification, grain growth and microstructure*. 2004: Elsevier.
67. Chen, J., et al., *Microstructural Changes and Kinetics of Reduction of Hematite to Magnetite in CO/CO 2 Gas Atmospheres.* Metallurgical and Materials Transactions B, 2019. **50**: p. 2612-2622.

68. John, D.S., S. Matthew, and P. Hayes, *Establishment of product morphology during the initial stages of wustite reduction.* Metallurgical Transactions B, 1984. **15**: p. 709-717.
69. John, D.S., S. Matthew, and P. Hayes, *The breakdown of dense iron layers on wustite in CO/CO 2 and H 2/H 2 O systems.* Metallurgical Transactions B, 1984. **15**: p. 701-708.
70. Xie, D.-G., et al., *In situ study of the initiation of hydrogen bubbles at the aluminium metal/oxide interface.* Nature materials, 2015. **14**(9): p. 899-903.
71. El-Zoka, A.A., et al., *The Fate of Water in Hydrogen-Based Iron Oxide Reduction.* Advanced Science, 2023. **10**(24): p. 2300626.
72. Hayes, P.C. and P. Grieveson, *Microstructural changes on the reduction of hematite to maanetite.* Metallurgical transactions B, 1981. **12**: p. 579-587.
73. Turkdogan, E.T., Olsson, R. G., & Vinters, J. V., *Turkdogan, E. T., Olsson, R. G., & Vinters, J. V. (1971). Gaseous reduction of iron oxides: Part II. Pore characteristics of iron reduced from hematite in hydrogen.* Metallurgical and Materials Transactions B, 1971. **2**: p. 3189-3196.
74. Cavaliere, P., et al., *Three-dimensional characterization of porosity in iron ore pellets: A comprehensive study.* Minerals Engineering, 2024. **213**: p. 108746.
75. Khani, M., H.A. Ebrahim, and S. Habibzadeh, *A comprehensive random pore model kinetic study of hematite to iron reduction by hydrogen.* Chemical Engineering Science, 2023. **281**: p. 119116.
76. Turkdogan, E., R. Olsson, and J. Vinters, *Gaseous reduction of iron oxides: Part II. Pore characteristics of iron reduced from hematite in hydrogen.* Metallurgical and Materials Transactions B, 1971. **2**: p. 3189-3196.
77. Paul, S., et al., *A Percolating Path to Green Iron.* 2024.
78. John, D.S. and P. Hayes, *Microstructural features produced by the reduction of wustite in H 2/H 2 O gas mixtures.* Metallurgical Transactions B, 1982. **13**: p. 117-124.
79. Moujahid, S.E. and A. Rist, *The nucleation of iron on dense wustite: a morphological study.* Metallurgical Transactions B, 1988. **19**: p. 787-802.
80. Turkdogan, E. and J. Vinters, *Gaseous reduction of iron oxides: Part III. Reduction-oxidation of porous and dense iron oxides and iron.* Metallurgical Transactions, 1972. **3**: p. 1561-1574.
81. Hayes, P., *Analysis of product morphologies and reaction mechanisms on gaseous reduction of iron oxides.* steel research international, 2011. **82**(5): p. 480-493.
82. Özgün, Ö., et al., *How much hydrogen is in green steel?* npj Materials Degradation, 2023. **7**(1).
83. Sebastian Lang, T.H., and Max Köpf, *Circored Fine Ore Direct Reduction Plus DRI Smelting: Proven Technologies for the Transition Towards Green Steel.* REWAS 2022: Energy Technologies and CO2 Management (Volume II), Springer International Publishing, Cham, 2022: p. 61-71.
84. Guo, L., et al., *A review on prevention of sticking during fluidized bed reduction of fine iron ore.* ISIJ International, 2020. **60**(1): p. 1-17.
85. Wolfinger, T., D. Spreitzer, and J. Schenk, *Analysis of the usability of iron ore ultra-fines for hydrogen-based fluidized bed direct reduction—a review.* Materials, 2022. **15**(7): p. 2687.
86. Spreitzer, D. and J. Schenk, *Fluidization behavior and reducibility of iron ore fines during hydrogen-induced fluidized bed reduction.* Particuology, 2020. **52**: p. 36-46.
87. Zhu, Q., R. Wu, and H. Li, *Direct reduction of hematite powders in a fluidized bed reactor.* Particuology, 2013. **11**(3): p. 294-300.
88. He, K., et al., *Kinetics of hydrogen reduction of Brazilian hematite in a micro-fluidized bed.* International Journal of Hydrogen Energy, 2021. **46**(5): p. 4592-4605.
89. Moukassi, M., et al., *A study of the mechanism of reduction with hydrogen of pure wustite single crystals.* Metallurgical Transactions B, 1983. **14**: p. 125-132.
90. Mao, W. and W.G. Sloof, *Reduction kinetics of wüstite scale on pure iron and steel sheets in Ar and H 2 gas mixture.* Metallurgical and Materials Transactions B, 2017. **48**: p. 2707-2716.

91. Ma, Y., et al., *Hydrogen-based direct reduction of iron oxide at 700°C: Heterogeneity at pellet and microstructure scales.* International Journal of Minerals, Metallurgy and Materials, 2022. **29**(10): p. 1901-1907.
92. Zheng, X., et al., *Correlating Chemical Reaction and Mass Transport in Hydrogen-based Direct Reduction of Iron Oxide.* arXiv preprint arXiv:2302.14215, 2023.
93. Zhao, Z., et al., *Direct reduction swelling behavior of pellets in hydrogen-based shaft furnaces under typical atmospheres.* International Journal of Minerals, Metallurgy and Materials, 2022. **29**(10): p. 1891-1900.
94. Pineau, A., N. Kanari, and I. Gaballah, *Kinetics of reduction of iron oxides by H2: Part II. Low temperature reduction of magnetite.* Thermochimica Acta, 2007. **456**(2): p. 75-88.
95. Metolina, P., T.R. Ribeiro, and R. Guardani, *Hydrogen-based direct reduction of industrial iron ore pellets: Statistically designed experiments and computational simulation.* International Journal of Minerals, Metallurgy and Materials, 2022. **29**(10): p. 1908-1921.
96. Dirba, I., et al., *Production of Fe nanoparticles from γ-Fe 2 O 3 by high-pressure hydrogen reduction.* Nanoscale Advances, 2020. **2**(10): p. 4777-4784.
97. Kazemi, M., M.S. Pour, and D. Sichen, *Experimental and modeling study on reduction of hematite pellets by hydrogen gas.* Metallurgical and Materials Transactions B, 2017. **48**: p. 1114-1122.
98. Lutterotti, L., *Total pattern fitting for the combined size–strain–stress–texture determination in thin film diffraction.* Nuclear Instruments and Methods in Physics Research Section B: Beam Interactions with Materials and Atoms, 2010. **268**(3-4): p. 334-340.
99. F. Adam, B.D., C. Gleitzer, *Cracking of hematite crystals during their low-temperature reduction into magnetite.* Solid State Ionic, 1989. **32**(33): p. 330-333.
100. Hofmann, A., *Physical chemistry essentials*. 2018: Springer. 147-152.
101. Li, M., et al., *Adsorption and dissociation of high-pressure hydrogen on Fe (100) and Fe2O3 (001) surfaces: Combining DFT calculation and statistical thermodynamics.* Acta Materialia, 2022. **239**.
102. Cheng, Q., et al., *Adsorption properties of hydrogen with iron oxides (FeO, Fe2O3): A ReaxFF molecular dynamics study.* Computational Materials Science, 2023. **218**.
103. Solaz-Portolés, J.J. and J. Quílez-Pardo, *Thermodynamics and the Le Chatelier's principle.* Revista Mexicana de Física, 1994. **41**(1): p. 128-138.
104. Kang, H., et al., *Influence of hydrogen flow rate on multistep kinetics of hematite reduction.* International Journal of Hydrogen Energy, 2024. **49**: p. 1255-1268.
105. Guo, L., et al., *Nucleation and growth of iron whiskers during gaseous reduction of hematite iron ore fines.* Metals, 2019. **9**(7): p. 750.
106. Basson, E., *World Steel in Figure 2024*, W.s. association, Editor. 2024: Brussel.
107. Zheng, X., et al., *Correlating chemistry and mass transport in sustainable iron production.* Proc Natl Acad Sci U S A, 2023. **120**(43): p. e2305097120.
108. Shimokawabe, M., R. Furuichi, and T. Ishii, *Influence of the preparation history of α-Fe2O3 on its reactivity for hydrogen reduction.* Thermochimica Acta, 1979. **28**(2): p. 287-305.
109. Piotrowski, K., et al., *Topochemical approach of kinetics of the reduction of hematite to wüstite.* Chemical Engineering Journal, 2007. **131**(1-3): p. 73-82.
110. Pena, J., et al., *Kinetic study of the redox process for storing hydrogen: reduction stage.* Catalysis today, 2006. **116**(3): p. 439-444.
111. Hessels, C., et al., *Reduction kinetics of combusted iron powder using hydrogen.* Powder Technology, 2022. **407**: p. 117540.
112. Thüns, N., et al., *The effect of H2 pressure on the reduction kinetics of hematite at low temperatures.* International Journal of Hydrogen Energy, 2019. **44**(50): p. 27615-27625.
113. Wang, H., et al., *A computational study of adsorption and activation of CO 2 and H 2 over Fe(1 0 0) surface.* Journal of CO2 Utilization, 2016. **15**: p. 107-114.

114. Dippel, A.-C., et al., *Beamline P02. 1 at PETRA III for high-resolution and high-energy powder diffraction.* Journal of synchrotron radiation, 2015. **22**(3): p. 675-687.
115. Pistidda, C., et al., *First Direct Study of the Ammonolysis Reaction in the Most Common Alkaline and Alkaline Earth Metal Hydrides by in Situ SR-PXD.* The Journal of Physical Chemistry C, 2015. **119**(2): p. 934-943.
116. Ginell, K.M., et al., *Materials for learning use of GSAS-II.* Powder Diffraction, 2019. **34**(2): p. 184-188.
117. Lenthe, W., et al., *Spherical indexing of overlap EBSD patterns for orientation-related phases–Application to titanium.* Acta Materialia, 2020. **188**: p. 579-590.
118. Martínez-Criado, G., et al., *ID16B: a hard X-ray nanoprobe beamline at the ESRF for nano-analysis.* Journal of synchrotron radiation, 2016. **23**(1): p. 344-352.
119. Paganin, D., et al., *Simultaneous phase and amplitude extraction from a single defocused image of a homogeneous object.* Journal of microscopy, 2002. **206**(1): p. 33-40.
120. Mirone, A., et al., *The PyHST2 hybrid distributed code for high speed tomographic reconstruction with iterative reconstruction and a priori knowledge capabilities.* Nuclear Instruments and Methods in Physics Research Section B: Beam Interactions with Materials and Atoms, 2014. **324**: p. 41-48.
121. Strohmann, T., et al., *Semantic segmentation of synchrotron tomography of multiphase Al-Si alloys using a convolutional neural network with a pixel-wise weighted loss function.* Scientific reports, 2019. **9**(1): p. 19611.
122. Ronneberger, O., P. Fischer, and T. Brox. *U-net: Convolutional networks for biomedical image segmentation*. in *Medical image computing and computer-assisted intervention–MICCAI 2015: 18th international conference, Munich, Germany, October 5-9, 2015, proceedings, part III 18*. 2015. Springer.
123. Boulos, V., et al. *Investigating performance variations of an optimized GPU-ported granulometry algorithm*. in *Proceedings of the 2012 Conference on Design and Architectures for Signal and Image Processing*. 2012. IEEE.
124. Von Bogdandy, L. and H.-J. Engell, *The reduction of iron ores: scientific basis and technology*. 2013: Springer Science & Business Media.
125. Atkins, P.W., J. De Paula, and J. Keeler, *Atkins' physical chemistry*. 2023: Oxford university press.
126. Levenspiel, O., *Chemical reaction engineering*. 1998: John wiley & sons.
127. Khawam, A. and D.R. Flanagan, *Solid-state kinetic models: basics and mathematical fundamentals.* The journal of physical chemistry B, 2006. **110**(35): p. 17315-17328.
128. Vyazovkin, S., et al., *ICTAC Kinetics Committee recommendations for performing kinetic computations on thermal analysis data.* Thermochimica acta, 2011. **520**(1-2): p. 1-19.
129. Melchiori, T. and P. Canu, *Improving the quantitative description of reacting porous solids: critical analysis of the shrinking core model by comparison to the generalized grain model.* Industrial & Engineering Chemistry Research, 2014. **53**(22): p. 8980-8995.
130. Ruiz Puigdollers, A., et al., *Increasing oxide reducibility: the role of metal/oxide interfaces in the formation of oxygen vacancies.* Acs Catalysis, 2017. **7**(10): p. 6493-6513.
131. Kang, S.-J.L., *Sintering: densification, grain growth and microstructure*. 2005: Elsevier.
132. Basson, E., *2022 World Steel Fig.* 2022. p. 1-30.
133. Ma, Y., et al., *Reducing Iron Oxide with Ammonia: A Sustainable Path to Green Steel.* Advanced Science, 2023. **10**(16): p. 2300111.
134. Flores-Granobles, M. and M. Saeys, *Minimizing CO2 emissions with renewable energy: a comparative study of emerging technologies in the steel industry.* Energy & Environmental Science, 2020. **13**(7): p. 1923-1932.

135. Raabe, D., *The Materials Science behind Sustainable Metals and Alloys.* Chemical Reviews, 2023. **123**(5): p. 2436-2608.
136. Wang, R.R., et al., *Hydrogen direct reduction (H-DR) in steel industry—An overview of challenges and opportunities.* Journal of Cleaner Production, 2021. **329**: p. 129797.
137. Tang, J., et al., *Development and progress on hydrogen metallurgy.* International Journal of Minerals, Metallurgy and Materials, 2020. **27**(6): p. 713-723.
138. Cavaliere, P., et al., *Hydrogen-Based Direct Reduction of Iron Oxides Pellets Modeling.* steel research international, 2023. **94**(6): p. 2200791.
139. Ma, Y., et al., *Hierarchical nature of hydrogen-based direct reduction of iron oxides.* Scripta Materialia, 2022. **213**: p. 114571.
140. Naseri Seftejani, M., J. Schenk, and M.A. Zarl, *Reduction of Haematite Using Hydrogen Thermal Plasma.* Materials (Basel), 2019. **12**(10).
141. Bhadeshia, H.K.D.H., *Prevention of hydrogen embrittlement in steels.* ISIJ International, 2016. **56**(1): p. 24-36.
142. Sun, B., et al., *Current Challenges and Opportunities Toward Understanding Hydrogen Embrittlement Mechanisms in Advanced High-Strength Steels: A Review.* Acta Metallurgica Sinica (English Letters), 2021. **34**(6): p. 741-754.
143. Johnson, W.H., *On some remarkable changes produced in iron and steel by the action of hydrogen and acids.* Proc. Royal Society of London, 1874. **23**: p. 168-180.
144. Robertson, I.M., et al., *Hydrogen Embrittlement Understood.* Metallurgical and Materials Transactions B, 2015. **46**(3): p. 1085-1103.
145. Beachem, C.D., *A new model for hydrogen-assisted cracking (hydrogen "embrittlement").* Metallurgical Transactions, 1972. **3**(2): p. 441-455.
146. Huang, L., et al., *Quantitative tests revealing hydrogen-enhanced dislocation motion in α-iron.* Nature Materials, 2023. **22**(6): p. 710-716.
147. Oriani, R.A., *A mechanistic theory of hydrogen embrittlement of steels.* Berichte der Bunsengesellschaft für physikalische Chemie, 1972. **76**(8): p. 848-857.
148. Lynch, S., *Hydrogen embrittlement phenomena and mechanisms.* Corrosion Reviews, 2012. **30**(3-4): p. 105-123.
149. Nagumo, M., K. Ohta, and H. Saitoh, *Deformation induced defects in iron revealed by thermal desorption spectroscopy of tritium.* Scripta Materialia, 1999. **40**(3): p. 313-319.
150. Ma, M.-T., et al., *Hydrogen Embrittlement of Advanced High-Strength Steel for Automobile Application: A Review.* Acta Metallurgica Sinica (English Letters), 2023. **36**(7): p. 1144-1158.
151. Koyama, M., et al., *Recent progress in microstructural hydrogen mapping in steels: quantification, kinetic analysis, and multi-scale characterisation.* Materials Science and Technology, 2017. **33**(13): p. 1481-1496.
152. Auinger, M., et al., *A novel laboratory set-up for investigating surface and interface reactions during short term annealing cycles at high temperatures.* Review of Scientific Instruments, 2013. **84**(8): p. 085108.
153. Ellingham, H.J.T., *Reducibility of oxides and sulphides in metallurgical processes.* Journal of the Society of Chemical Industry, 1944. **63**(5): p. 125-160.
154. Spreitzer, D. and J. Schenk, *Reduction of Iron Oxides with Hydrogen—A Review.* Steel Research International, 2019. **90**(10): p. 1900108.
155. Choo, W.Y., and Jai Young Lee, *Thermal Analysis of Trapped Hydrogen in Pure Iron.* Metallurgical Transactions A, 1982. **13A**: p. 135-140.
156. Hong, G.-w. and J.-y. Lee, *The interaction of hydrogen with iron oxide inclusions in iron.* Materials Science and Engineering, 1983. **61**(3): p. 219-225.

157. Lee, J.L., & Lee, J. Y. , *The interaction of Hydrogen with the Interface of Al2O3 Particles in Iron.* METALLURGICAL TRANSACTIONS A 1986. **17A**: p. 2183-2186.
158. Lee, K.Y., Lee, J. Y., & Kim, D. R. , *A Study of Hydrogen-trapping Phenomena in AISI 5160 Spring Steel* Materials Science and Engineering: A, 1984. **67**(2): p. 213-220.
159. Oudriss, A., et al., *Grain size and grain-boundary effects on diffusion and trapping of hydrogen in pure nickel.* Acta Materialia, 2012. **60**(19): p. 6814-6828.
160. Sato, R. and K. Takai, *Quantitative hydrogen trap states on high-angle grain boundaries and at dislocations in iron.* Scripta Materialia, 2023. **228**: p. 115339.
161. Chen, Y.-S., et al., *Observation of hydrogen trapping at dislocations, grain boundaries, and precipitates.* Science, 2020. **367**(6474): p. 171-175.
162. Kissinger, H.E., *Reaction Kinetics in Differential Thermal Analysis.* Analytical Chemistry, 1957. **29**(11): p. 1702-1706.
163. Hayward, E. and C.-C. Fu, *Interplay between hydrogen and vacancies inα-Fe.* Physical Review B, 2013. **87**(17): p. 174103.
164. Jiang, D.E. and E.A. Carter, *Diffusion of interstitial hydrogen into and through bcc Fe from first principles.* Physical Review B, 2004. **70**(6): p. 064102.
165. Vandewalle, L., et al., *A combined thermal desorption spectroscopy and internal friction study on the interaction of hydrogen with microstructural defects and the influence of carbon distribution.* Acta Materialia, 2022. **241**.
166. Lee, J.-Y. and J.-L. Lee, *A trapping theory of hydrogen in pure iron.* Philosophical Magazine A, 1987. **56**(3): p. 293-309.
167. Lee, J. and J.Y. Lee, *Hydrogen trapping in AISI 4340 steel.* Metal Science, 1983. **17**(9): p. 426-432.
168. Holappa, L., *Chapter 1.6 - Secondary Steelmaking*, in *Treatise on Process Metallurgy*, S. Seetharaman, Editor. 2014, Elsevier: Boston. p. 324-330.
169. Turkdogan, E.T., *Fundamentals of Steelmaking*. 1996, London: Institute of Materials.
170. Starshinov, B.N., N. A. Voronova, T. Pliskanovskii, O. A. Mogilevtsev, G. N. Shtein, E. N. Vishnyakova, N. P. Popova, and Yu N. Vyazovskii., *Improving the properties of foundry-grade pig iron.* Metallurgist, 1972. **16**(2): p. 96-99.
171. Vrbek, K., et al., *Changes in Hydrogen Content During Steelmaking.* Archives of Metallurgy and Materials, 2015. **60**(1): p. 295-299.
172. Shirband, Z., M.R. Shishesaz, and A. Ashrafi, *Hydrogen degradation of steels and its related parameters, a review.* Phase Transitions, 2011. **84**(11-12): p. 924-943.
173. Yan, Y., et al., *Hydrogen-induced cracking and service safety evaluation for precipitation strengthened austenitic stainless steel as hydrogen storage tank.* International Journal of Hydrogen Energy, 2014. **39**(31): p. 17921-17928.
174. Wan, D., et al., *Evaluation of hydrogen effect on the fatigue crack growth behavior of medium-Mn steels via in-situ hydrogen plasma charging in an environmental scanning electron microscope.* Journal of Materials Science & Technology, 2021. **85**: p. 30-43.
175. Lu, X., et al., *Insight into hydrogen effect on a duplex medium-Mn steel revealed by in-situ nanoindentation test.* International Journal of Hydrogen Energy, 2019. **44**(36): p. 20545-20551.
176. Sun, B., et al., *Chemical heterogeneity enhances hydrogen resistance in high-strength steels.* Nature Materials, 2021. **20**(12): p. 1629-1634.
177. Nakiboglu, F., D.S. John, and P. Hayes, *The gaseous reduction of solid calciowustites in Co/Co 2 and H 2/H 2 O gas mixtures.* Metallurgical Transactions B, 1986. **17**: p. 375-381.
178. Kim, W.-H., et al., *Influence of CaO and SiO2 on the reducibility of wüstite using H2 and CO gas.* ISIJ international, 2012. **52**(8): p. 1463-1471.

179. Zeng, R., N. Wang, and W. Li, *Influence of SiO2 on the gas-based direct reduction behavior of Hongge vanadium titanomagnetite pellet by hydrogen-rich gases.* Powder Technology, 2021. **386**: p. 90-97.
180. Kapelyushin, Y., et al., *Effect of alumina on the gaseous reduction of magnetite in CO/CO 2 gas mixtures.* Metallurgical and Materials Transactions B, 2015. **46**: p. 1175-1185.
181. Welty, J., G.L. Rorrer, and D.G. Foster, *Fundamentals of momentum, heat, and mass transfer*. 2014: John Wiley & Sons.
182. Bale, C.W., et al., *FactSage thermochemical software and databases.* Calphad, 2002. **26**(2): p. 189-228.
183. Bale, C.W., et al., *Reprint of: FactSage thermochemical software and databases, 2010–2016.* Calphad, 2016. **55**: p. 1-19.
184. Kissinger, H.E., *Reaction Kinetics in Differential Thermal Analysis* Analytical Chemistry, 1957. **29(11)**: p. 1702-1706.
185. LEE, J.Y., LEE, S.M., *Hydrogen Trapping Phenomena in Metals with b.c.c. and f.c.c. Crystal Structures by the Desorption Thermal Analysis Technique.* Surface and coating technology, 1986. **28**: p. 301-314.
186. Rau, M.F., Rieck, D., & Evans, J. W., *Investigation of iron oxide reduction by TEM.* Metallurgical and Materials Transactions B, 1987. **18**(1): p. 257-278.
187. Chen, Y.-S., et al., *Observation of hydrogen trapping at dislocations, grain boundaries, and precipitates.* Science, 2020. **367**(6474): p. 171-175.
188. Pressouyre, G.M., *A Classification of Hydrogen Traps in steel.* Metallurgical Transactions A 1979. **10**: p. 1571-1573.
189. Ryu, J.H., et al., *Effect of deformation on hydrogen trapping and effusion in TRIP-assisted steel.* Acta Materialia, 2012. **60**(10): p. 4085-4092.
190. Choo, W., et al., *Hydrogen solubility in pure iron and effects of alloying elements on the solubility in the temperature range 20 to 500 C.* Journal of Materials Science, 1981. **16**: p. 1285-1292.
191. Jha, K.N., et al., *Hydrogen control during steel making for medium carbon wheels.* Scandinavian Journal of Metallurgy, 2003. **32**(6): p. 296-300.